SPECIAL REPORT 90-14

Ice Forces on Flat, Vertical Indentors Pushed Through Floating Ice Sheets

Naoki Nakazawa and Devinder S. Sodhi

May 1990

For conversion of SI metric units to U.S./British customary units of measurement consult ASTM Standard E380, Metric Practice Guide, *published by the American Society for Testing and Materials, 1916 Race St., Philadelphia, Pa. 19103.*

Special Report 90-14

U.S. Army Corps of Engineers
Cold Regions Research & Engineering Laboratory

Ice Forces on Flat, Vertical Indentors Pushed Through Floating Ice Sheets

Naoki Nakazawa and Devinder S. Sodhi

May 1990

Prepared for
OFFICE OF THE CHIEF OF ENGINEERS

PREFACE

This report was prepared by Naoki Nakazawa, graduate student, Arctic Engineering Program, University of Alaska, Fairbanks, and Dr. Devinder S. Sodhi, Research Hydraulic Engineer, Ice Engineering Research Branch, Experimental Engineering Division, U.S. Army Cold Regions Research and Engineering Laboratory. Funding for this project was provided by the Directorate of Civil Works, Civil Works Program, *Ice Engineering*, CWIS 31723, *Model Studies and Ice Effects on Structures*.

The authors express their gratitude to Guenther E. Frankenstein, Chief of the Ice Engineering Research Branch, for his encouragement of this research. They also thank Dr. John P. Zarling, Dr. Wilford F. Weeks and Dr. J. Leroy Hulsey of University of Alaska, Fairbanks, for their arrangements and encouragement of this study at CRREL, Carl R. Martinson for assistance in conducting the tests, Stephen L. DenHartog for the video recording, Edward P. Foltyn for the help in computer programming and John J. Gagnon for the help in data storage. The first author is grateful to Kieko Nakazawa, his wife, for typing the first draft of this report and her encouragement during this study.

CONTENTS

ILLUSTRATIONS

Figure

TABLES

Table

Ice Forces on Flat, Vertical Indentors Pushed Through Floating Ice Sheets

NAOKI NAKAZAWA AND DEVINDER S. SODHI

INTRODUCTION

About half the Earth's surface is subject to snow, ice and seasonally frozen ground. Extensive permafrost and ice sheets exist in the polar regions, and the oceans are covered by seasonal and multiyear sea ice. With the growth of human activities in cold regions, the impact of snow, ice and frozen ground on human affairs and commercial development has grown in recent decades, thus establishing the need for scientific research. In low temperatures, the properties of most materials change, and many machines either do not work as designed or fail. Design criteria and construction techniques for structures for cold regions are different from those in warm regions.

Purpose for this study

A rational basis is needed for the design and construction of structures in coastal and offshore regions where the presence of floating ice presents a hazard. Among the ice forces imposed on structures that interact with ice, the impact of an ice floe produces some of the greatest loads that the structure has to be designed to withstand. This impact can be approximated by an indentation.

In this study, indentation tests were conducted to allow us to observe ice failure and to determine the distribution of ice pressures and the total ice force. The geometry of an indentation in an actual environment is shown in Figure 1. An ice sheet of thickness h moves at a velocity v past an indentor of width d. Because of the limits imposed by model testing in the laboratory, indentors with a velocity v were *pushed* through an ice sheet in this study.

Previous indentation studies were conducted using finite-sized ice sheets that were confined in a frame. Because of the limitations of hydraulic equipment or facilities, many of these tests used a short indentation distance. However, limited studies by Kato and Sodhi (1984), Sodhi and Morris (1984) and Timco (1987) have been conducted on large, floating ice sheets with long indentation distances, simulating the indentation of a vertical structure into an infinite, first-year, floating ice sheet.

The previous studies did not completely illuminate the ice failure mechanism. It is, therefore, the objective of this study to attempt to understand the ice failure process during ice crushing against an indentor. To accomplish this, instrumented indentors were pushed against the edge of floating ice sheets at different velocities. The instrumentation of the indentors allowed us to measure both the total ice force and the local ice pressure or the position of the resultant ice force within the contact area. Furthermore, transducers were placed to monitor the Acoustic Emission (AE) activity in the ice and to measure displacements of the carriage and the indentor, which enabled us to analyze the energies stored in the structure and dissipated in the ice.

Plots of force versus time and force versus displacement allowed us to draw conclusions concerning the

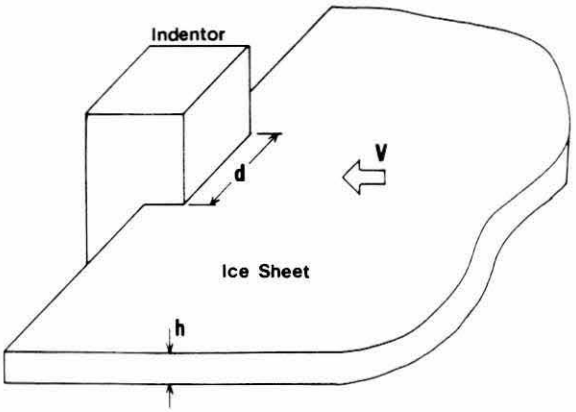

Figure 1. Schematic of indentation geometry.

magnitude of the force or energy required to make an ice sheet fail, as well as allowing us to observe the size of the damage zone in the ice sheet during each loading event. Moreover, AE signals, believed to be caused by the formation of microcracks, were correlated with the damage caused by the interaction and with the resulting ice forces. To summarize the objectives of this study, we hoped to do the following:

1. Observe the nature of the ice failure mode during the indentation.
2. Estimate the energy required to cause an ice sheet to fail.
3. Observe the indentor response at the point of the ice failure.
4. Determine whether there is any non-simultaneous crushing failure by measuring the distribution of ice pressure at the ice/structure interface.
5. Determine the frequency of ice crushing failure.

The instrumentation used in this study had some desirable features. First of all, the experiments were conducted on large, floating ice sheets, simulating an infinite ice sheet; second, the indentor support was quite stiff; third, a screw-driven carriage capable of moving up to 2 m was used; fourth, direct ice force measurements were made by mounting the indentor on the load cells at the ice/structure interface; and fifth, separate measurements were made of carriage and indentor displacement relative to an ice sheet.

We carried out 92 indentation tests with rigid, vertical, flat indentors of various widths at different indentation velocities on different thicknesses of freshwater ice. We varied several parameters during this study—indentor widths of 50, 60, 100 and 150 mm were used, ice thickness ranged from 20 to 60 mm, and indentor velocity varied between 1 and 9 mm/s.

During each test, we measured the force generated during ice–indentor interaction, ice pressure at the ice/indentor interface, indentor displacement relative to the ice sheet, displacement of the carriage relative to a fixed datum, and AE activity in the ice. In addition, we noted nucleation of the first radial crack using an event marker, and used photography and video to record the experiments.

Background

The crystallographic structure and properties of both freshwater and sea ice have been intensively studied (e.g., Weeks and Ackley 1982, Weeks and Cox 1984). Through studies by many investigators, the dependence of ice strength (i.e., compressive, tensile and bending strength) on temperature, strain rate, grain size, porosity, salinity, etc., is now well understood. Frictional resistance and adfreeze bond strength between ice and different materials (e.g., concrete, steel and wood) have been investigated by Tusima and Tabata (1979), Oksanen (1980), Forland and Tatinclaux (1984) and Saeki et al. (1986, 1988). Ice forces on bridge piers in rivers have been studied for a long time, but the interaction between ice and structures in offshore regions is a relatively new field of study.

For the estimation of design loads, ice forces are broadly divided into two categories (Neill 1976, Sanderson 1988): static and dynamic.

Static loading

The loading state is defined as static if ice exists in stationary contact with a structure, and then the structure experiences an increasing load applied to it by natural driving forces, such as wind and water stresses, and thermal expansion of ice sheets because of warming.

Dynamic loading

The loading state is defined as dynamic if an ice feature is not initially in contact with a structure, but arrives and strikes it with an appreciable velocity. This loading state differs significantly from static loading in two respects: firstly, the initial contact conditions are invariably irregular and nonuniform, and secondly, the duration of the impact is generally determined by the kinetic energy of the impacting ice feature, which may come to rest during the process. Examples of dynamic ice forces are impacts by multiyear floes and by icebergs or ice islands.

In addition to the above two broad categories of loading, it is also necessary to understand the magnitude of the forces and the contact area over which these forces act. For example, total force on the whole structure and local pressures over a limited area are extremely important.

Total load

The total load sustained by a structure is important for considerations of foundation sliding resistance, foundation bearing capacity and overturning moment.

Local loads or pressure

The magnitude and distribution of local pressure is essential information for determination of the design and spacing of internal structural members and the dimensions of internal cell units. Loads over smaller areas are also important for the design of the external skin of a structure.

Structures placed in an ice environment should be able to withstand not only the total ice load but also the local pressure. A good understanding of these loads will lead to an economical design for structures.

Experimental and theoretical studies on ice pressure distribution at the ice/structure interface were conducted by Schwarz (1970), Kry (1978, 1979), Tanaka et al. (1987), Tunik (1987) and Blanchet (1987).

Korzhavin's formula, which empirically relates ice crushing force with contact area and compressive strength of ice, has been discussed by many researchers. Experimental and theoretical studies to determine ice forces on structures were conducted by many researchers: laboratory tests were done by Hirayama et al. (1974), Michel and Toussaint (1977), Saeki et al. (1977), Kry (1980b), Michel and Blanchet (1983), Kato and Sodhi (1984), Sodhi and Morris (1984) and Timco (1987); field tests have been done by Zabilansky et al. (1975) and Croasdale et al. (1977).

EXPERIMENTAL SETUP AND PROCEDURES

Facilities

The experiments were conducted in the test basin of CRREL's Ice Engineering Facility. The test basin is 34.4 m (113 ft) long, 9 m (30 ft) wide and 2.4 m (8 ft) deep. A photograph of the test basin is shown in Figure 2. The test basin is insulated, and its refrigeration is provided by seven forced-air heat exchangers suspended from the ceiling. The total refrigeration capacity is 80 kW, and the minimum air temperature that can be achieved is approximately –23°C. The refrigeration fluid is ammonia.

Ice sheets

Ice growth

The freshwater ice sheets were grown in the test basin. To freeze an ice sheet, a mixture of water and air was sprayed into the cold air over the water surface. The resulting seed crystals falling from the air onto the water surface started the ice growth and ensured uniform, small size grains (approximately 1 to 2 mm) throughout the sheet. The top layer of the ice sheet is generally thin

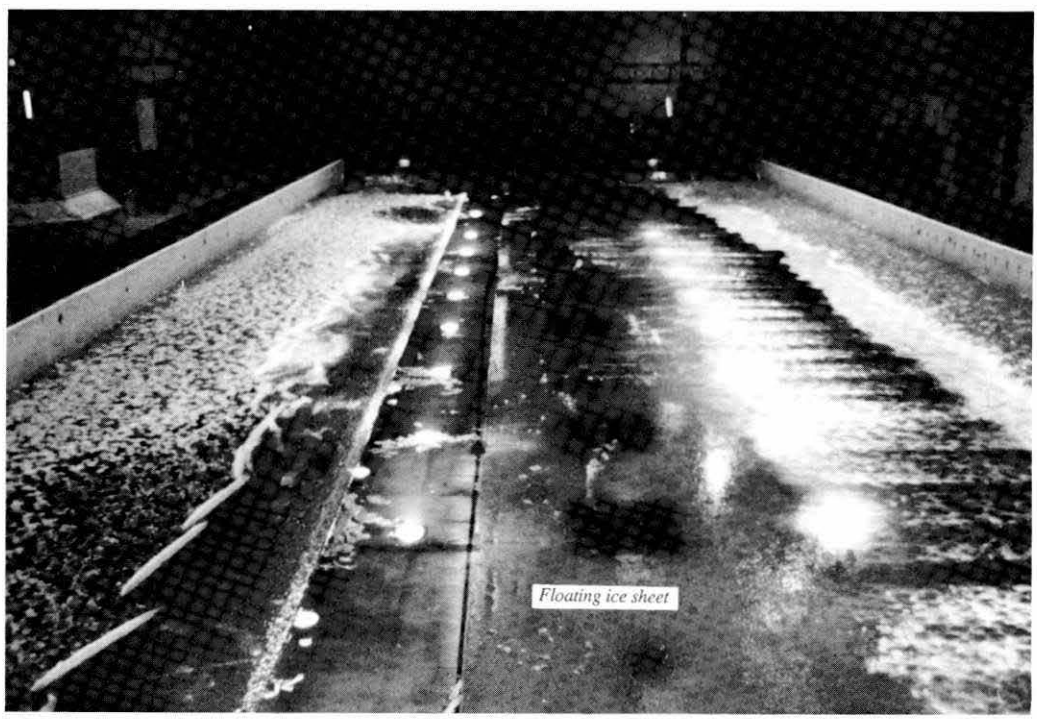

Figure 2. Test basin.

(1 mm) and is composed of columnar ice with a mixed vertical and horizontal c-axis orientation. The rest of the ice sheet has a random c-axis orientation in the horizontal plane and has a columnar structure characteristic of dendritic type growth.

The ice sheets were grown at several temperatures, depending on the time available for freezing and the cooling capacity available from the refrigeration plant. Most sheets were grown at a temperature between –15 and –20°C. It took approximately 36 hours to grow a 50-mm-thick ice sheet. On a typical day of testing, the room was allowed to warm to approximately –3°C, after which the ice was allowed to temper and to attain a uniform temperature.

Temperature

The temperature of the ice sheets was measured a few times during the program and was found to be between –1 and 0°C.

Ice thickness

The ice thickness was measured after each test at the test track using vernier calipers with a resolution of 0.05 mm.

Characteristic length

The characteristic length of each floating ice sheet was measured shortly before the tests for that day. A deadweight (10 lb [5 kg]) was placed over a circular plate near the center of an ice sheet. The resulting deflection of the sheet was measured using a displacement transducer at the point of loading. The characteristic length of the floating ice sheet was calculated according to the theory of an infinite plate on an elastic foundation (Wyman 1950, Sodhi et al. 1982).

The setup for load application and deformation measurements is shown schematically in Figure 3. The characteristic length was calculated using eq 1.

$$l = \left\{ \frac{\Delta P}{8K\,\Delta w} \left[1 + \frac{\alpha^2}{2\pi} \left(\ln \frac{\gamma\alpha}{2} - \frac{5}{4} \right) \right] \right\}^{1/2} \qquad (1)$$

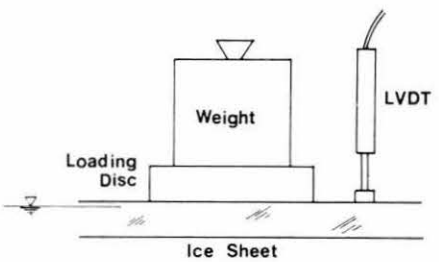

Figure 3. Experimental setup for measuring the characteristic length of a floating ice sheet.

where l = characteristic length of ice sheet
ΔP = incremental load placed on the ice sheet
K = specific weight of water
Δw = resulting deflection increment of the ice sheet at the center of the load zone
$\ln\gamma$ = 0.55772157 (Euler constant)
r = radius of the applied load
α = r/l.

Elastic modulus

The elastic modulus can then be calculated by eq 2 using the characteristic length and ice thickness

$$E = \frac{12(1-\nu^2)K\,l^4}{h^3} \qquad (2)$$

where E = effective elastic modulus
ν = Poisson's ratio for ice
K = specific weight of water
l = characteristic length of the ice
h = ice thickness.

Experimental apparatus

A schematic drawing of the test structure setup is shown in Figure 4. A carriage that travels parallel to the length of the basin was used to carry the test apparatus. The high-force module, which includes a screw-driven carriage for the indentation tests, was mounted under the carriage. The test structure, structural support and indentor were attached to the screw-driven carriage. The test structure traveled perpendicular to the longitudinal direction of the basin, and was powered by a motor located at one end of the high-force module. The range of velocity for the carriage in the high-force module was from 1 to 9 mm/s. A photograph of the high-force module is shown in Figure 5.

A schematic diagram of the experimental setup is

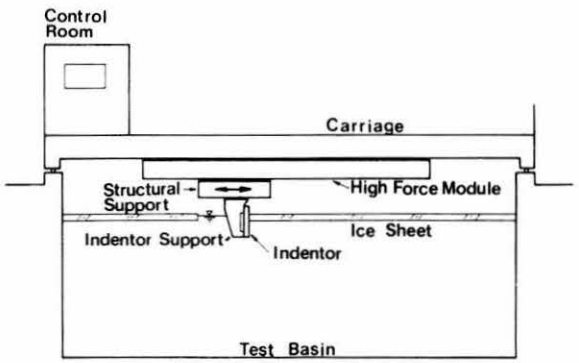

Figure 4. Schematic of the test structure setup.

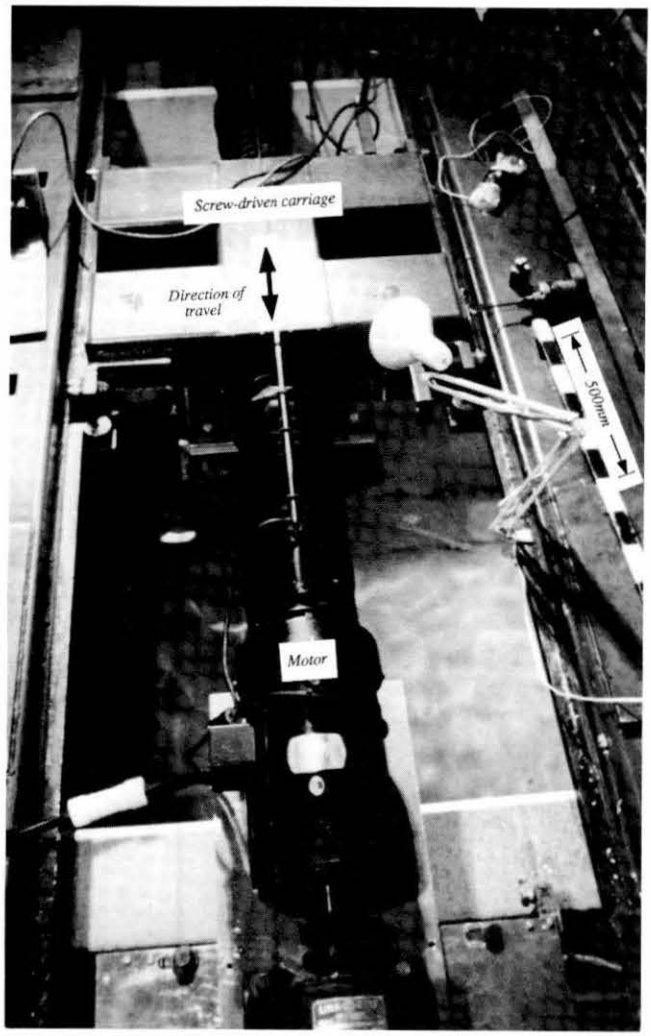

Figure 5. High-force module, looking from above.

shown in Figure 6. The structural support mounted on the carriage of the high-force module is 1.2 m long, 0.6 m wide and 0.3 m high. The indentor support was mounted under the structural support, and indentor plates were attached to the indentor support. Both the indentor and structural support moved together. The load cell installed in the structural support was calibrated to measure the horizontal ice force on the indentor.

The following two methods were used to determine the pressure distribution on the indentor (Fig. 7).

Installation of pressure transducers on the indentor plate

The pressure transducers were installed to measure the local ice pressure at the ice–indentor interface. The widths of the indentor used with this method were 60 and 100 mm. Two pressure transducers were installed on the 60-mm-width indentor and four pressure transducers on the 100-mm-width indentor.

Support of indentor on three load cells

The indentor plate was mounted on three load cells that were installed on the supporting structure behind the indentor. The total interaction force at the interface was obtained by summing the forces measured by each load cell. The indentor widths used with this setup were 50, 100 and 150 mm.

Mounting the indentor plate on three load cells produced a stiff load-measuring system that gauged the interaction forces without the influence of the structural response. This methodology (Fig. 7b) to measure interaction forces enabled us to determine not only the magnitude of the total forces but also the position of the

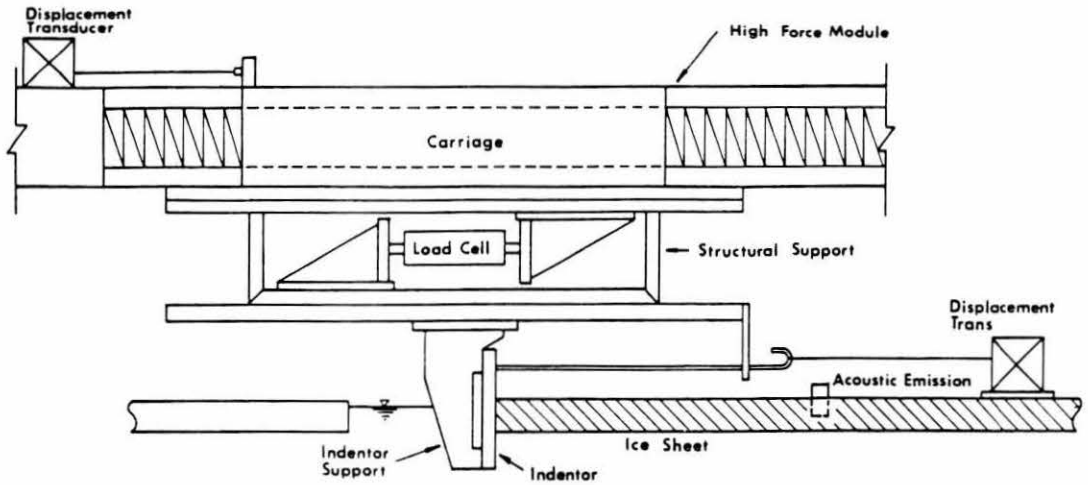

Figure 6. Schematic of the experimental setup.

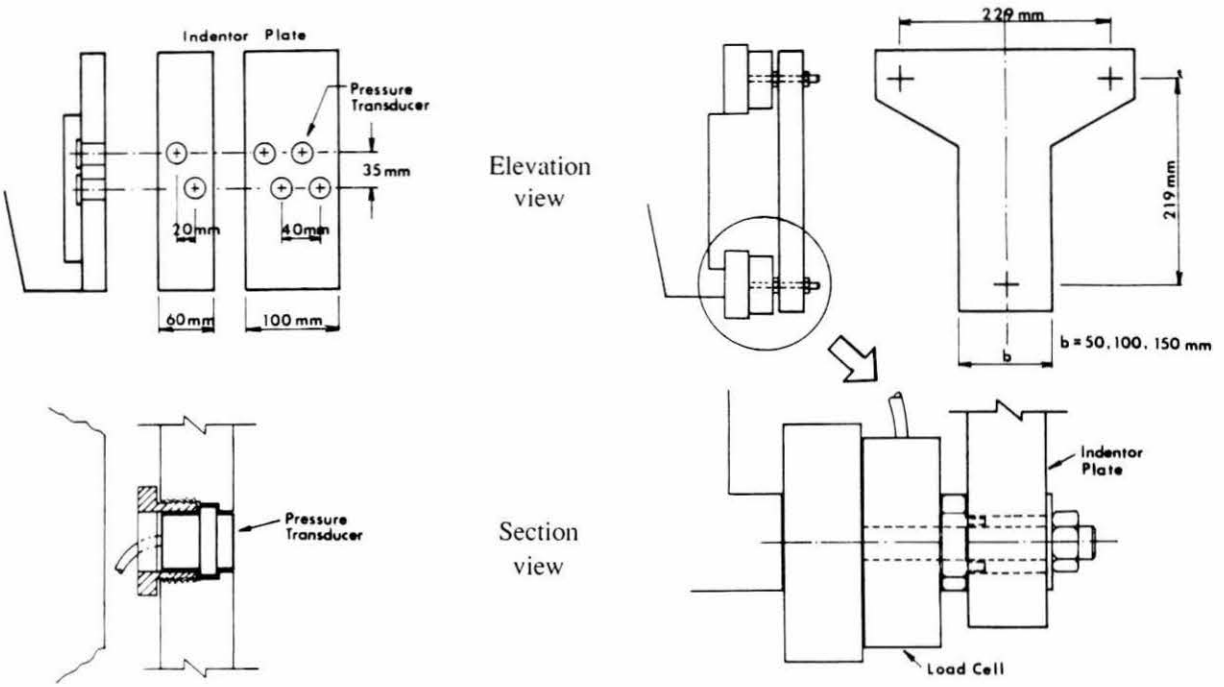

a. Installation of pressure transducers on the indentor plate.

b. Support of indentor on three load cells.

Figure 7. Schematic of indentor plate.

resultant forces. When the resultant force is found to be in the center of the contact area, it is an indication of a symmetrical distribution of ice pressure at the interface. Examples of simple symmetrical distributions of ice pressure would be a uniform or a parabolic distribution or a combination of these two. However, if the position of the resultant force is not at the center of the contact area, we know that the distribution of ice pressure is asymmetrical.

Instrumentation

A 44-kN-capacity (10,000-lb) load cell shown in Figure 6 was installed on the structural support to measure the total ice force. However, only part of the total interaction force at the interface was measured by this load cell (which was calibrated prior to the testing program). The capacity of each load cell supporting the indentor plate was 22 kN (5000 lb). The capacity of each of the 13 pressure transducers installed on the indentor plate was 7 MPa (rated) and 14 MPa (maximum). Because the capacity of these transducers was not high enough, they failed, one after the other, during the tests because of overloading.

The velocity of the structural support was measured using a position–velocity transducer mounted on the frame of the high-force module and attached to the screw-driven carriage. Displacement of the indentor relative to the ice sheet was measured using another position–velocity transducer that was placed on the ice sheet and connected to the indentor surface.

An Acoustic Emission (AE) sensor was placed in the ice sheet to monitor the acoustic activity from microcracking during deformation of the ice. The AE transducer was connected to a signal conditioner whose output in volts was proportional to the cumulative AEs (or counts) received by the sensor. It would automatically reset to zero whenever it reached a maximum limit.

An event marker was used to record the initial contact between the indentor and the ice and the nucleation of the first radial macrocrack in the ice sheet during tests. The event marker was connected to the signal conditioner, and the researcher observing the tests cued the signal conditioner by touching the event marker.

Data acquisition system

A flow chart of the data acquisition system used to monitor our tests is shown in Figure 8. The data acquisition system was controlled by a desk-top computer that also provided input–output handling for data storage. All transducers were connected to a signal conditioner that also provided the excitation voltage to each transducer. The data were stored in digital form on floppy disks.

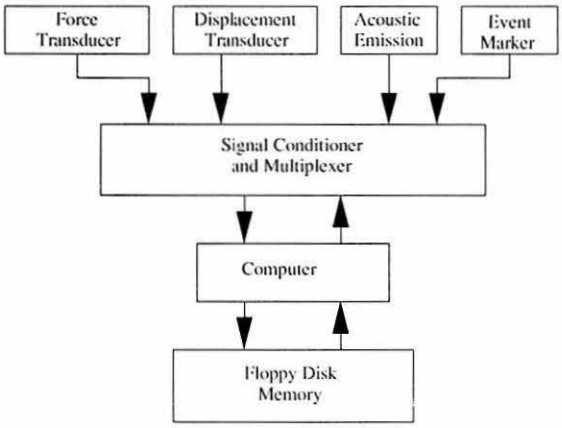

Figure 8. Flow chart of the data acquisition system.

Testing procedures

When the ice sheet thickness reached that required for the planned test, the characteristic length of the ice sheet was measured by placing a deadweight on the center of the ice sheet and monitoring its vertical displacement with respect to a fixed datum. A slot was cut in the ice sheet with a chain saw to allow the indentor, which protruded below the water surface, to travel from one test location to another. The ice was carefully cut to avoid cracking and to make the ice edge perpendicular to the indentor surface. Indentation tests were performed on ice that was visually free of macrocracks.

The AE sensor was placed in the ice sheet by drilling a 1-cm-deep hole at a location approximately 70 cm in front of the indentor. A weight was placed on it to keep it in firm contact with the ice sheet. A displacement transducer was also placed on the ice sheet approximately 1.5 m in front of the indentor and its string was connected to the indentor plate. Indentation tests were conducted after these preparations.

Tests were conducted along several tracks in the ice sheet as shown schematically in Figure 9. First, a test was conducted on an undamaged (with no microcracks) ice sheet for several seconds and then stopped (first run). During these tests, extensive microcracks were produced in front of the indentor. Then, another test was carried out on this damaged ice in the track created by the first run at the same velocity (second run). The time interval between these two tests (or runs) was usually 2 to 3 minutes. During the first run, the initial contact of the indentor with the ice and the nucleation of the first radial macrocrack were recorded manually with the help of the event marker.

After conducting two tests in one track, we moved the carriage to another location, doing two more tests at a different velocity, creating another test track (see Fig. 9). Up to five test locations were carefully chosen to avoid existing cracks in the ice sheet, the distance between different test tracks being at least 3 m. In one day, 9 to 11 tests were usually conducted on one ice sheet. Second runs for tests at very low velocities (1 mm/s) were not conducted. Still photographs and video recording of the tests were taken. After the tests, crushed ice specimens were cut out to observe and to photograph the ice damaged by microcracking.

Summary of test series

The test period was from 19 February through 18 April 1988. Altogether, 92 tests were conducted in an 8-week period.

Tests were divided into two test series. First, tests were conducted in which the pressure transducers were installed on the indentor (Fig. 7a). When some of the pressure transducers failed because of overloading during the tests, the experimental setup was changed to supporting the indentor plate on three load cells (Fig. 7b), thus enabling the measurement of total force and determining the position of the resultant force. They are labeled NSC test and N N test, respectively. The test conditions are listed in Table 1 for NSC tests and in Table 2 for N N tests.

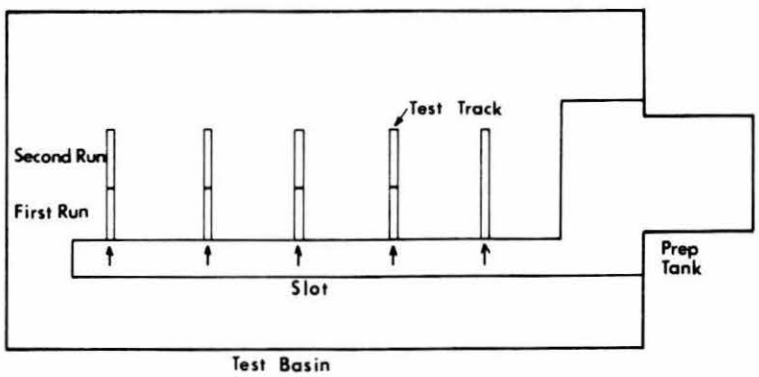

Figure 9. Test track location in the basin.

Table 1. Parameters and ice properties for the NSC series of tests.

Date (1988)	Test number	Indentor width (mm)	Ice thickness (mm)	Indentor velocity (mm/s)	Lc (cm)* E (Gpa)
19 Feb	89/88	60	50	7.7	not measured
	87/86	60	42	6.6	
	85/84	60	45	5.4	
	83/82	60	48	3.3	
25 Feb	79	100	26	7.8	not measured
	78	100	25	6.6	
	77	100	25	4.4	
	76	100	24	2.6	
29 Feb	69/68/67	100	57	7.9	not measured
	66	100	56	7.5	
	65	100	56	5.5	
	64/63/62/61	100	56	5.8	
	60	100	62	6.1	
	59	100	57	1.8	
7 Mar	49/48/47	100	52	7.9	not measured
	46	100	54	—	
	45	100	55	—	
	44	100	55	—	
10 Mar	39/38	100	45	8.0	not measured
	37	100	43	8.1	
	36	100	49	1.0	
16 Mar	29	100	47	8.3	$Lc = 116.7$
	28	100	58	0.9	$E = 1.19$
	27	100	56	1.5	
	26	100	56	1.3	
	25	100	56	1.0	
	24	100	55	3.1	
	23	100	53	4.6	
	22	100	57	6.2	
	21	100	51	7.9	
18 Mar	19	100	25	8.0	$Lc = 65.3$
	18	100	25	5.8	$E = 1.25$
	17	100	25	3.8	
	16	100	25	2.0	

*Lc = characteristic length; E = elastic modulus.

Table 2. Parameters and ice properties for the N N series of tests.

Date (1988)	Test number	Indentor width (mm)	Ice thickness (mm)	Indentor velocity (mm/s)	Lc (cm)* E (GPa)
1 Apr	31/32	50	26	9.3	$Lc = 65.3$
	33/34	50	26	7.0	$E = 1.11$
	5/36	50	27	4.6	
	37/38	50	27	2.2	
	39	50	27	1.2	
4 Apr	41/42	50	60	9.2	$Lc = 146.3$
	43/44	50	60	6.8	$E = 2.27$
	45/46	50	56	4.4	
	47/48	50	57	2.2	
	49	50	60	1.3	
7 Apr	51	100	34	9.1	$Lc = 77.3$
	52/53	100	34	6.9	$E = 1.07$
	54	100	33	9.4	
	55/56	100	33	4.5	
	57/58	100	32	2.3	
	59/60	100	33	2.0	
11 Apr	61/62	100	53	9.2	$Lc = 129.0$
	63/64	100	56	6.6	$E = 1.69$
	65/66	100	56	4.6/3.4	
	67/68	100	54	2.2	
	69/70	100	55	1.1	
	701	100	57	9.4	
14 Apr	71	150	30	4.9	$Lc = 71.8$
	72	150	31	2.9	$E = 1.05$
	73	150	30	0.3	
	74	150	29	1.5	
	75	150	31	1.1	
	76	150	33	1.2	
18 Apr	81	150	54	3.5	$Lc = 129.0$
					$E = 1.88$

*Lc = characteristic length; E = elastic modulus.

TEST RESULTS AND OBSERVATIONS

In this study, we observed microcracking near the indentor as well as a variety of failure modes during the indentation tests: radial cracking, circumferential cracking, cleavage cracking, spalling and crushing, and buckling. The time when the radial cracks occurred during a test depended on the test conditions, i.e., ice thickness, indentor width and indentor velocity.

Microcracking

Observations

Microcracking was observed visually and recorded by still photography and video. Sketches of microcracks and some larger cracks, based on visual observations, are shown in Figure 10. Photographs of a test, which were continuously taken from the initial contact through the ice failure, are shown in Figure 11.

At the onset of loading, microcracks formed in the immediate vicinity of the indentor (Fig. 10a). As the indentor deformed the ice, more microcracks appeared in an expanding zone. The crack density also appeared to increase with the passage of time after the initial contact between the indentor and the ice. As the ice force increased during microcracking and deformation of the ice, one (and sometimes two) big radial cracks propagated into the ice sheet ahead of the indentor. A photograph of the microcracks and a radial crack is shown in Figure 12. With the help of an event marker, it was possible to establish that this radial crack formed when the ice force reached a magnitude of about 70% of the maximum force; there is no indication in the record of any decrease in ice force at the time this crack nucleated and propagated. The length of these radial cracks was usually about 3 m and they formed almost perpendicular to the indentor face (Fig. 10b).

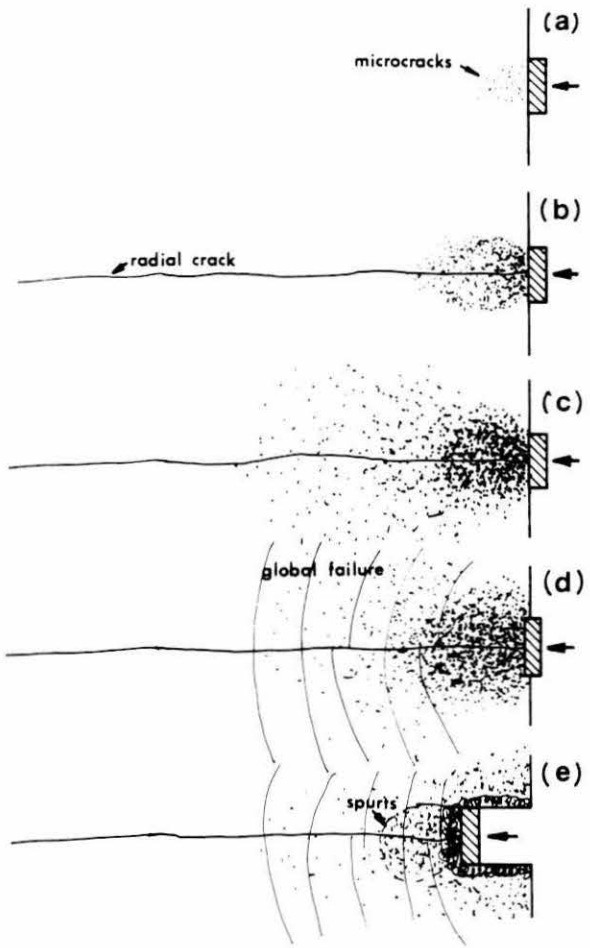

Figure 10. Microcracking and radial macrocracking behavior.

Even after the formation of the radial crack, microcracks would keep developing, not only in front of the indentor, but also on both sides. The ice in front of the indentor would turn milky with the accumulation of microcracks. We found by observing the tests that the highest density of microcracks was near the indentor, decreasing with increasing distance from it (Fig. 10c).

When the test velocity was high ($v > 4$ mm/s), the ice sheet failed brittlely, followed by sudden forward movements of the indentor into the ice sheet and into the zone of extensive cracks (Fig. 10d). When the indentor velocity was low ($v < 3$ mm/s), the ice failed ductilely, as indicated by the absence of sudden forward indentor motion and the rounded peaks in the ice force record.

During tests at high velocity ($v > 4$ mm/s), we observed spurts of microcracking prior to each subsequent failure. Microcracks developed ahead of the indentor, and then the indentor moved forward very quickly, accompanied by crushing or spalling of the damaged (microcracked) ice (Fig. 10e).

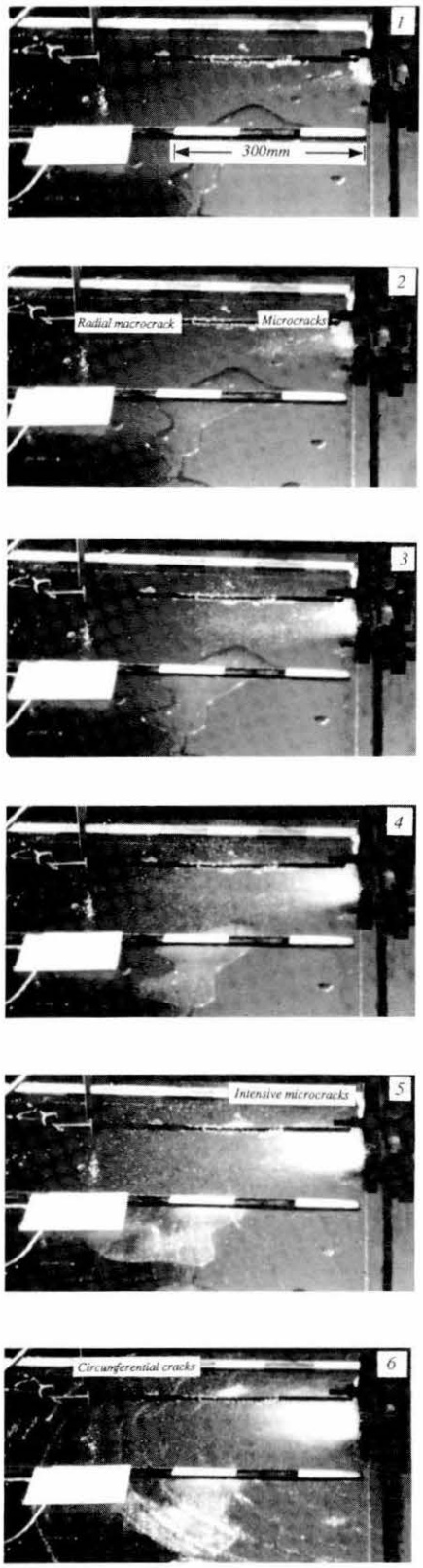

Figure 11. Progress of an indentation test from the initial contact through the first failure.

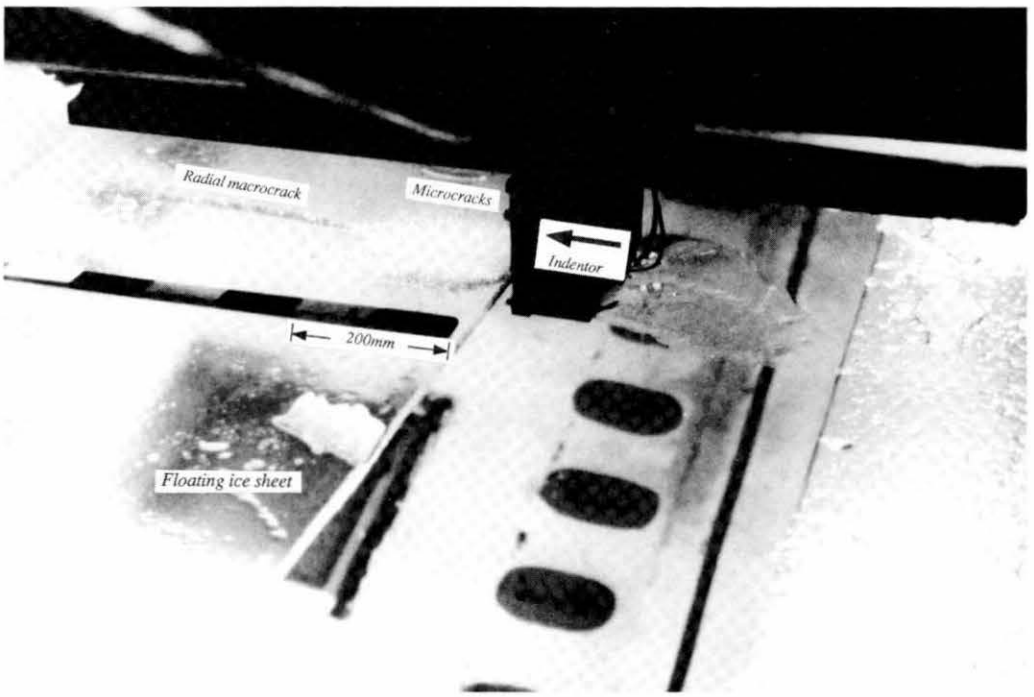

Figure 12. Microcracks and one radial macrocrack during a test.

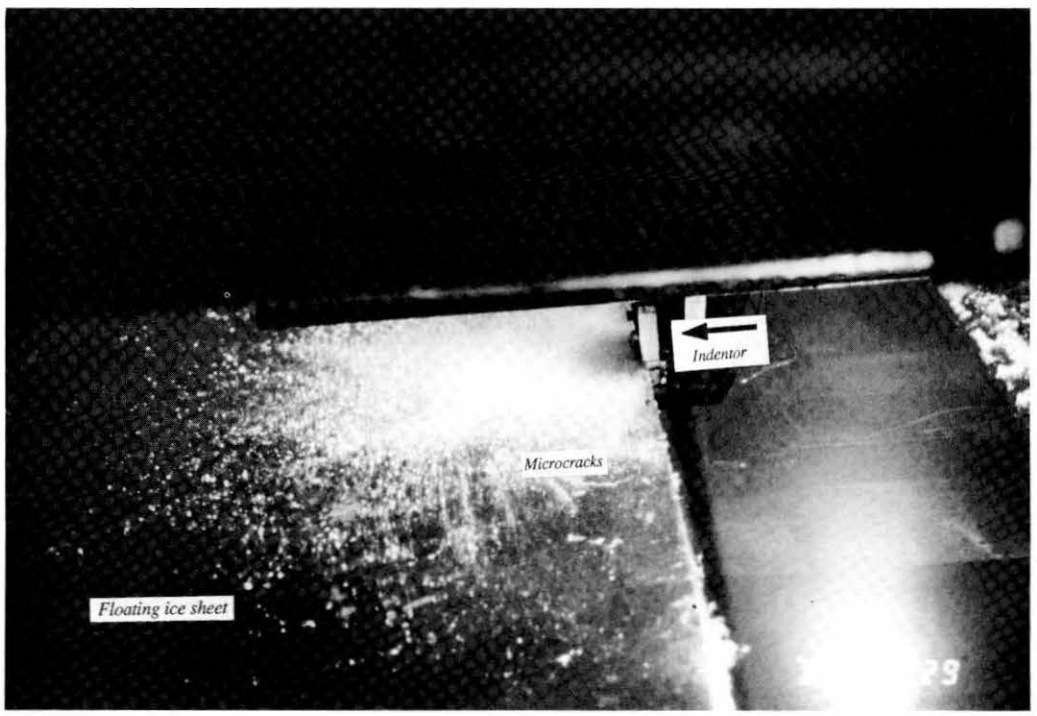

Figure 13. Microcracks during a test.

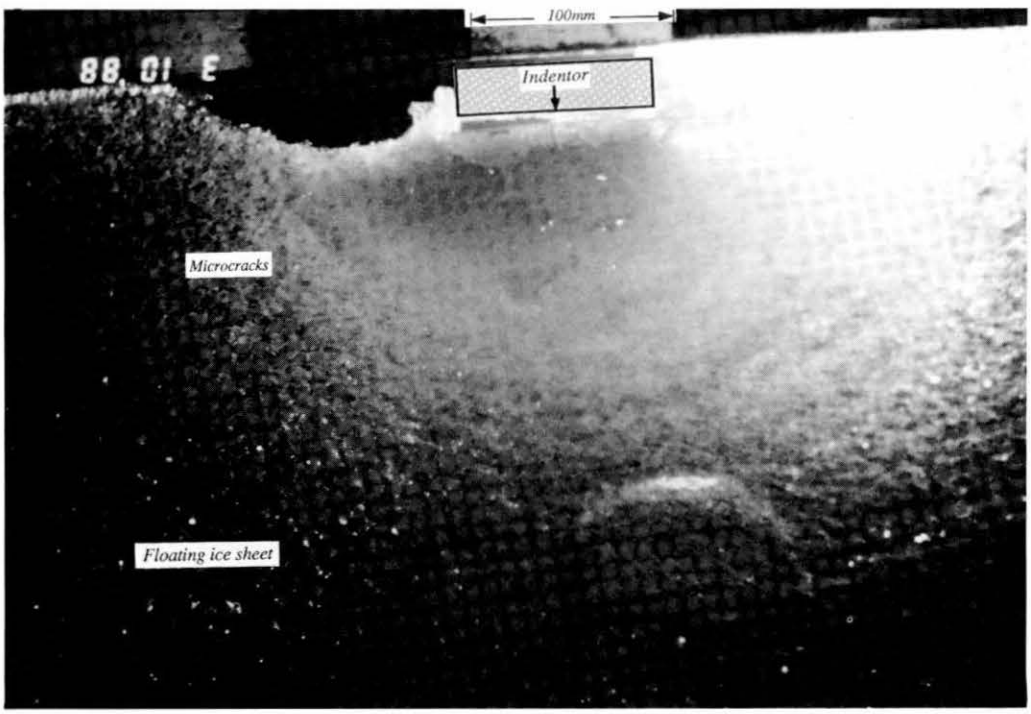

Figure 14. Microcracks in the ice after a test.

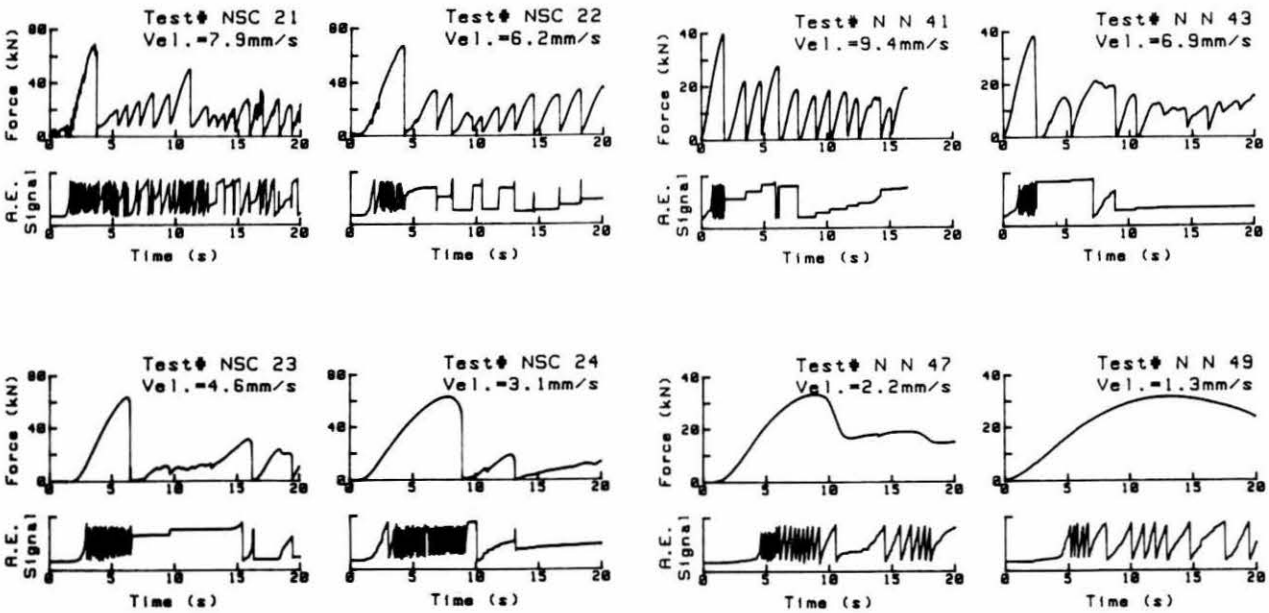

a. d = *100 mm and* h = *54 mm.* *b.* d = *50 mm and* h = *60 mm.*

Figure 15. Acoustic emission signals and ice force records.

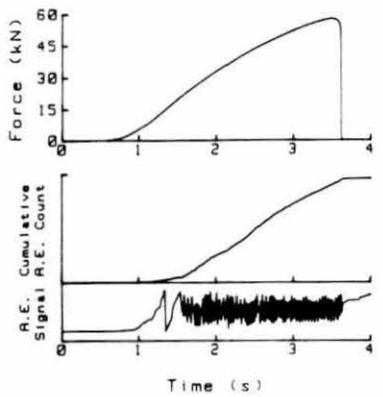

a. Test N N 61—d = *100 mm*, h = *53 mm*, v = *9.2 mm/s* .

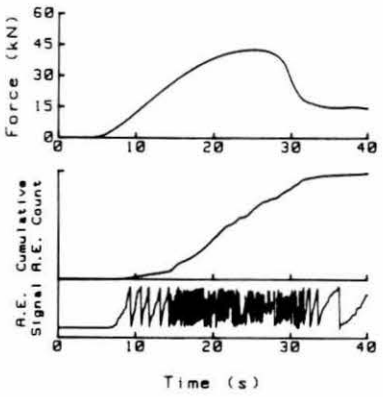

b. Test N N 69—d = *100 mm*, h = *55 mm*, v = *1.1 mm/s*.

Figure 16. Cumulative AE count and ice force.

Microcracks spread slower during tests with a low indentor velocity than they did during tests at higher velocities. Figure 13 shows a photograph of microcracks formed during a test, whereas Figure 14 shows a photograph of microcracks after a test. A preliminary examination of thin sections from a freshly deformed ice sample indicated that the microcracks were located at the grain boundaries. This agrees with the observations of Sinha (1984), who proposed a model for the initiation of intergranular cracks and their subsequent accumulation.

Microcracking and AE signals

Figure 15 shows records of the AE signals and the ice force versus time. As we stated previously in the section describing instrumentation, the AE apparatus would reset the cumulative count (or the signal) automatically to zero when the count reached the saturation level of the apparatus. The intense AE activity is reflected in the records by the high frequency of resetting. The increase in ice force correlates very well with the high AE count, which can be directly attributed to microcracking as observed visually. For the ductile failure at low velocity ($v < 3$ mm/s), an AE signal was recorded after the time when the maximum ice force occurred.

Figure 16 shows the cumulative AE count and the ice force with respect to the time for the indentor velocities of 9.2 and 1.1 mm/s. The upper curves in the AE figures are the cumulative count, which has been nondimensionalized with respect to its maximum value. After the buildup in the ice force, the cumulative AE count started to increase, and the ice force and the cumulative AE count increased together. These findings show that the microcracks are generated and accumulated in the ice by the indentor loading. In the test having high indentor velocity (9.2 mm/s), the cumulative AE count increased until brittle failure. At the low indentor velocity (1.1 mm/s), however, the cumulative AE count increased with increasing ice force. Even after the time when the peak force was recorded, this count continued to increase because of the ductile behavior of the ice.

Failure modes

The failure modes observed in the test series are illustrated schematically in Figure 17.

Radial crack

As mentioned in the previous section, one (or sometimes two) radial cracks were generated after a certain time (between 1 and 5 seconds, which depended on indentor velocity) following the initial contact between the indentor and the ice. The length of these radial cracks was usually about 3 m and they formed almost perpendicular to the indentor face (Fig. 17a).

Circumferential crack

Many circumferential cracks were generated in front of the indentor by the first brittle failure (Fig. 17b). Usually, five to ten circumferential cracks developed in front of the indentor. No circumferential cracks were generated when the ice failed ductilely.

Cleavage crack

Cleavage cracks (in-plane horizontal cracks) were sometimes observed in front of the indentor. These cracks appeared after the microcracks formed and grew gradually in size as the indentor loading increased (Fig. 17c). In Figure 18, the dense, milky semicircular shape in front of the indentor is a cleavage crack. Figure 19 shows a photograph of both a plan view and a cross

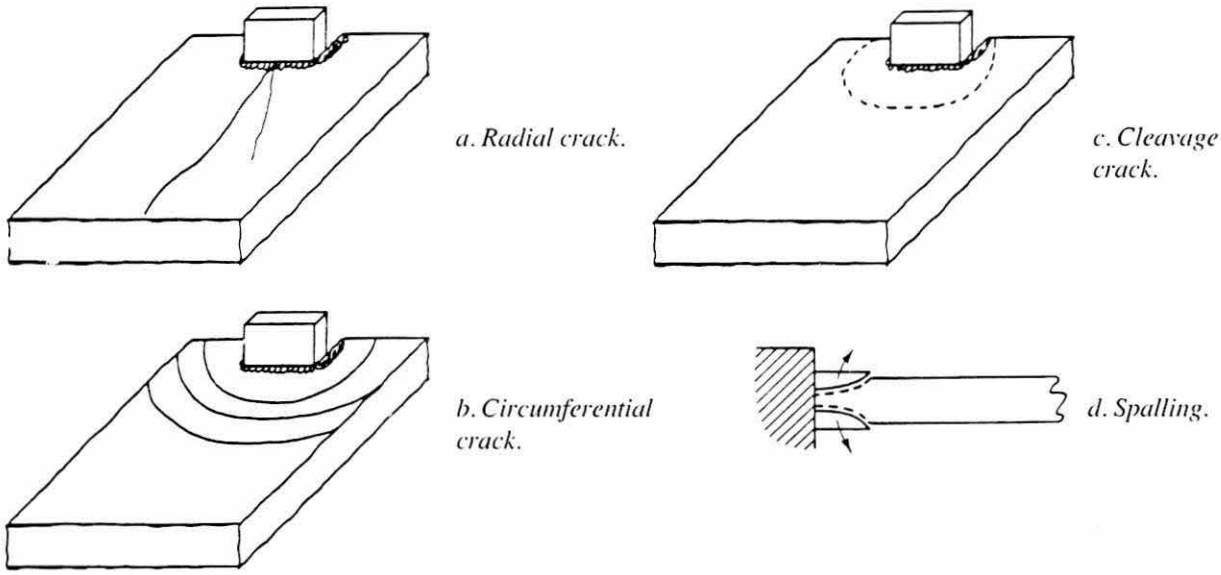

Figure 17. Global failure modes (after Sanderson 1988).

section of the ice cut after the test shown in Figure 18.

A theoretical model for the propagation of cleavage cracks was presented by Kendall (1978). A geometry useful in the analysis of cleavage propagation is shown in Figure 20. The compressive force P is conceptually divided into two forces $P/2$ acting at points a distance $h/2$ from the top and bottom surfaces. These two forces lead to tensile forces at the crack tip. More research is needed to understand cleavage crack propagation.

Spalling

During tests at intermediate to high indentation velocities ($v > 6$ mm/s), we observed local spalling failure during ice crushing. The sudden forward motion of the

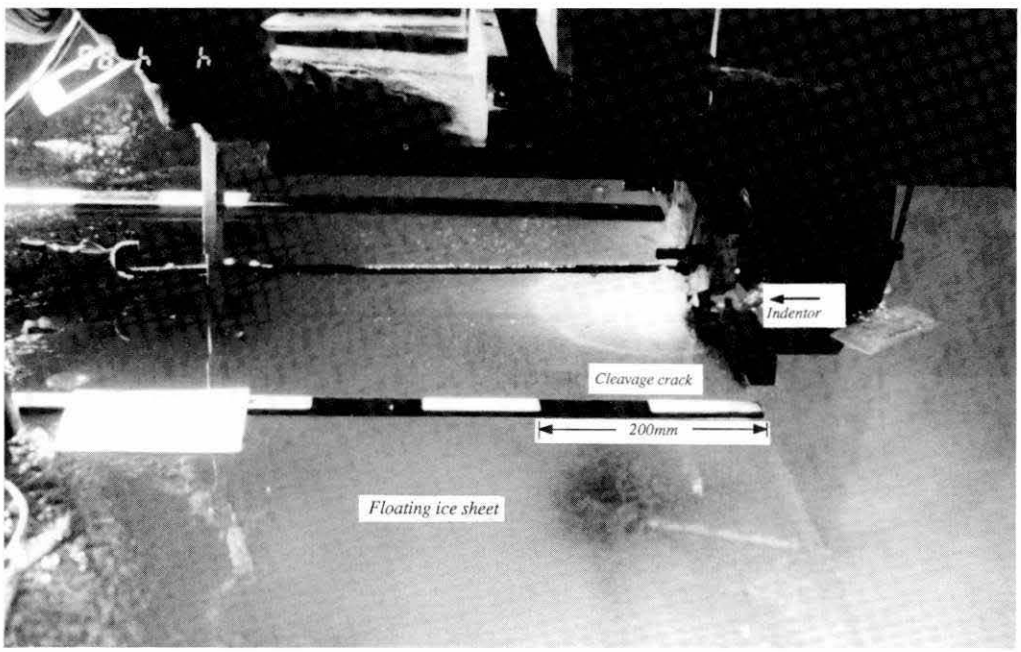

Figure 18. Cleavage crack during a test—semicircular shape in front of the indentor is a cleavage crack.

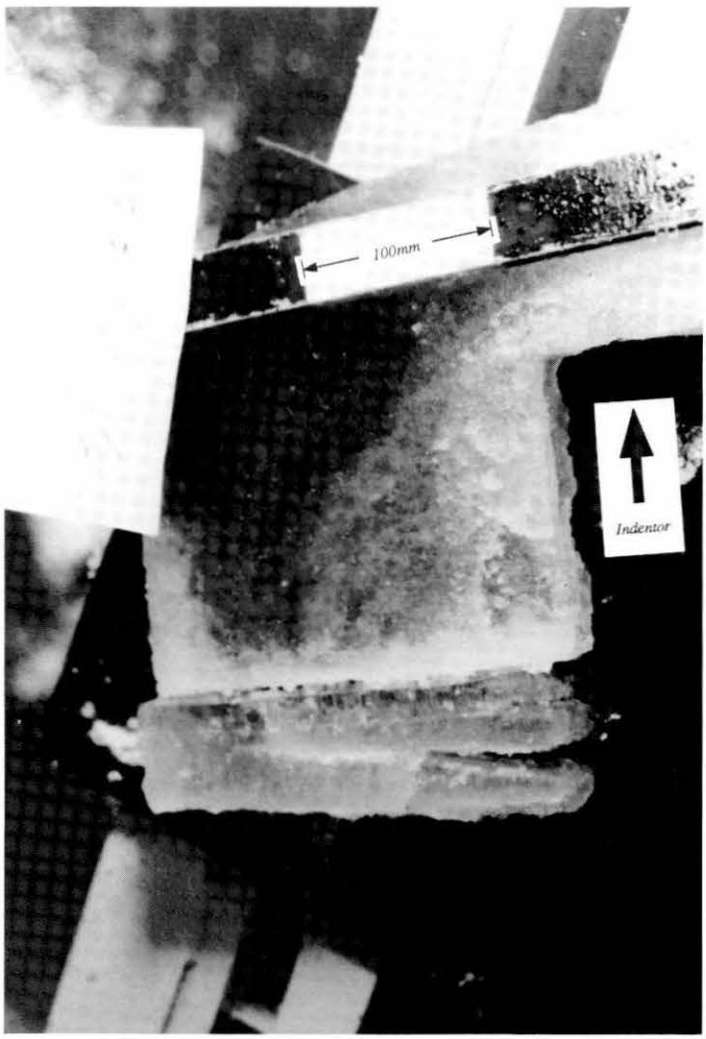

Figure 19. Ice horizontally separated by the in-plane cleavage crack: the plan view and the cross section of the ice (arrow indicates indentor path).

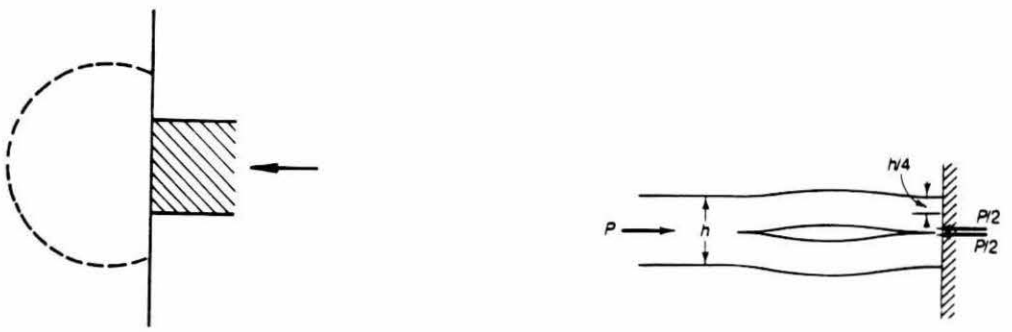

a. Plan view.

b. Cross-sectional view for the analysis of propagation of the cleavage crack.

Figure 20. Geometry of an in-plane cleavage crack (after Wierzbicki 1985).

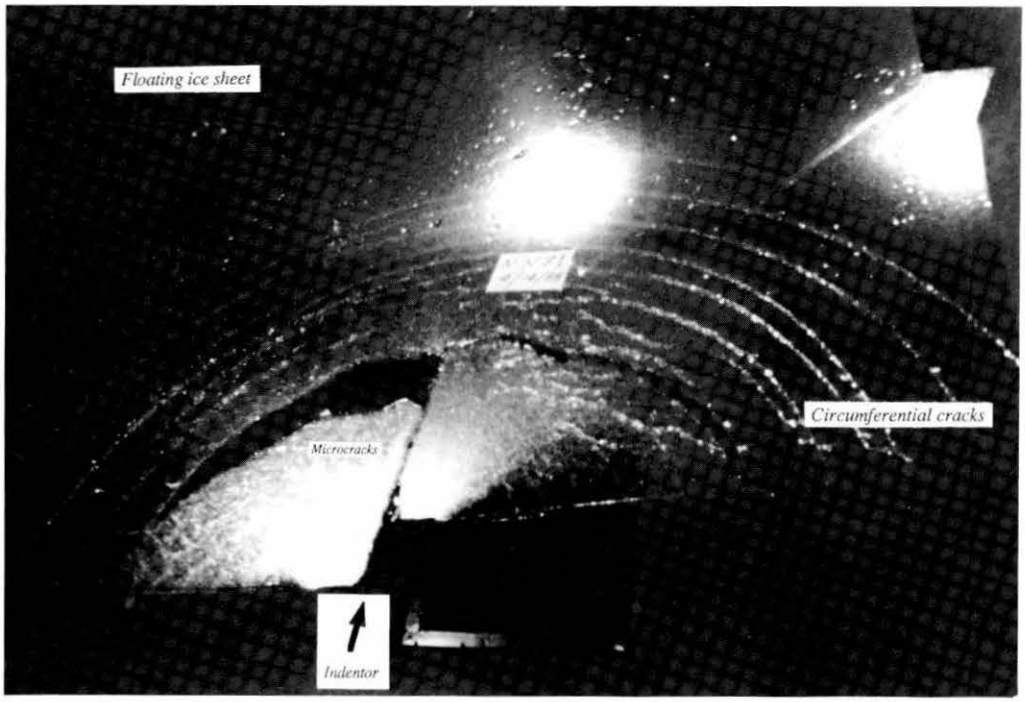

Figure 21. Buckled ice sheet with a number of circumferential cracks.

indentor caused fragments of ice to break away ahead of it. Ice, damaged by microcracks, expanded near the indentor. As the ice moved in the vertical direction, the indentor moved forward suddenly, with the ice fragments spalling up and down (Fig. 17d).

Buckling

In some tests, ice buckled, especially when indentors were pushed against thin ice at low velocities ($v < 3$ mm/s). Tests N N 71 to N N 76 ($d = 150$ mm) all resulted in buckling failure. At the onset of the loading, microcracks were generated in the same manner as stated earlier. But soon after the nucleation of the microcracks, the ice sheet started to bend downward and eventually buckled forming several circumferential cracks (Fig. 21).

DISCUSSION

To examine the factors influencing the ice forces on flat, vertical indentors, we looked at the following topics: velocity effects, energy analysis, ice pressure and contact area, position of resultant force, first peak force versus subsequent peak force, frequency of ice force failure, and buckling failure.

The velocities indicated in figures and tables are those of the average rate of indentor displacement relative to the ice sheet. Test results and analyses are summarized in Table 3.

Velocity effects

Because ice is a viscoelastic material, its properties depend on the magnitude of the stress it is under and the rate of stress application. The ice may fail by brittle fracture or by ductile creep, depending on the applied stress rate. The range of relative velocity in the present test series was between 1 and 9 mm/s.

At the instant of ice failure, especially during tests at intermediate to high indentor velocity ($v > 4$ mm/s), a sudden unloading occurred with a loud noise because the indentor would spring back to its original position. This can be seen in the displacement records of the carriage and the indentor in Figure 22, where force and displacement records are shown for tests at velocities ranging from 3.1 to 7.9 mm/s. Figure 23 defines the deformation of the structure: the difference between the displacement of the carriage and that of the indentor. We observed, from Figure 22, that the indentor displacement record was not always linear with time. The nonlinear displacement record of the indentor at a velocity of 3.1 mm/s in Figure 22 shows that the indentor catches up with the carriage faster as the ice resistance decreases as a result of creep failure.

The effects of velocity on the nature of failure can be seen in the records of ice force versus time and in the

records of ice force versus indentor displacement shown in Figures 24 and 25 respectively. The sudden unloading of the force on the indentor is an indication of brittle failure, whereas the ductile failure results in gradually decreasing force, but not all the way to zero. Typical force versus time plots for the brittle and the ductile failures of ice are shown in Figure 26.

At high velocities ($v > 4$ mm/s), after the initial contact of the indentor with the ice, the ice force increases monotonically to a maximum value, as shown in Figures 24 and 25. Microcracks nucleate and accumulate in the ice sheet during this period. Brittle ice behavior results in sudden unloading of the indentor at the instant of the ice failure and forward indentor movement, with crushing or spalling of the microcracked ice in front of the indentor. Because of brittle failure, a sawtooth type of force–time plot is recorded for high velocity tests.

At low velocities ($v < 3$ mm/s), the data in Figures 24 and 25 show that the ice forces gradually increase to a

Table 3. Summary of test parameters and results.

Test no.	Ice thickness, h (mm)	Elastic modulus, E (GPa)	Indentor Width, d (mm)	Indentor Velocity, v (mm/s)	F_{max}* (kN)	P_{max}** (MPa)	F_{sub}† (kN)	R = $\frac{F_{sub}}{F_{max}}$	f(Hz)††	fh/v
					NSC					
21	51	1.19	100	7.9	70.0	13.7	31.8	0.45		
22	57	1.19	100	6.2	67.1	11.8	29.3	0.44	0.54	4.96
23	53	1.19	100	4.6	63.0	11.9				
24	55	1.19	100	3.1	63.0	11.5				
25	56	1.19	100	1.0	56.0	10.0				
					NN					
31/32	26	1.11	50	9.3	17.0	13.1	6.4	0.38		
33/34	26	1.11	50	7.0	15.6	12.0	5.8	0.37		
35/36	27	1.11	50	4.6	15.3	11.3				
37/38	27	1.11	50	2.2	13.7	10.1				
39	27	1.11	50	1.2	12.7	9.4				
41/42	60	2.27	50	9.2	39.7	13.2	20.9	0.53	0.75	4.89
43/44	60	2.27	50	6.8	38.4	12.8	20.5	0.53	0.59	5.21
45/46	56	2.27	50	4.4	35.7	12.8				
47/48	57	2.27	50	2.2	33.0	11.6				
49	60	2.27	50	1.3	31.5	10.5				
51	34	1.07	100	9.1	31.9	9.4	13.0	0.41	1.52	5.68
52/53	34	1.07	100	6.9	28.4	8.4	11.0	0.39	0.86	4.24
54	33	1.07	100	9.4	28.7	8.7	13.0	0.45	1.38	4.84
55/56	33	1.07	100	4.5	28.7	8.7				
57/58	32	1.07	100	2.3	22.0	6.9				
59/60	33	1.07	100	2.0	24.2	7.3				
61/62	53	1.69	100	9.2	57.2	10.8	18.0	0.31	0.94	5.42
63/64	56	1.69	100	6.6	54.6	10.3	23.8	0.44	0.57	4.84
65/66	56	1.69	100	4.0	52.6	9.4	23.3	0.44	0.38	5.32
67/68	54	1.69	100	2.2	46.9	8.7				
69/70	55	1.69	100	1.1	42.5	7.7				
701	57	1.69	100	9.4	52.1	9.1	28.7	0.55	0.72	4.37
71	30	1.05	150	4.9	39.3	8.7				
72	31	1.05	150	2.9	31.0	6.7				
73	30	1.05	150	0.3	25.0	5.6				
74	29	1.05	150	1.5	33.2	7.6				
75	31	1.05	150	1.1	28.3	6.1				
76	33	1.05	150	1.2	30.5	6.2				

* Maximum force.
** Effective pressure.
† Maximum force of the first peak.
†† Frequency of ice failure.

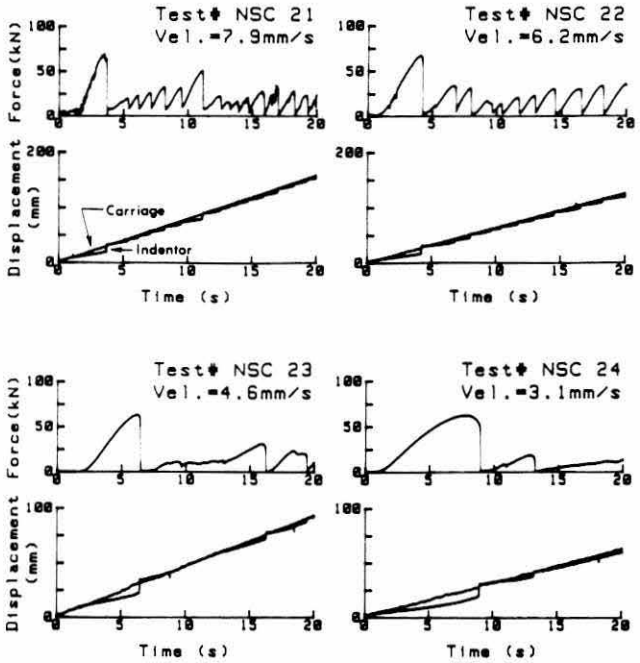

Figure 22. Plots of ice force and displacement of the carriage and the indentor with respect to time for the tests with d = *100 mm and* h = *54 mm at different velocities.*

maximum value after the initial contact and that the ductile deformation of ice results in gradual unloading of the indentor and smooth variations in the ice force records. Ductile failure can be recognized by rounded peaks attributable to softening of the material at high stress levels.

Sharp peaks in force versus time plots become rounded with decreasing velocity. It should, however, be noted that even at high velocity ($v > 4$ mm/s), the monotonic increase in the ice force becomes slightly rounded before the ice failure takes place.

Further, the plots of ice force versus the indentor displacement at different indentor velocities (Fig. 27) present ice force records up to the first few peaks to show the effect of velocity.

From these records, it appears that the indentor displacements corresponding to the peak ice force are almost the same even though the indentor velocities are different (the peaks in the records for ductile failure are a little bit to the right of those for brittle failure). Also, even after the ice failed brittlely (i.e., tests N N 35, 43, 45, 52 and 61), the indentors are still loaded for a certain distance after the peak force is recorded.

After the sudden unloading of the indentor, it moves forward until it again contacts the ice. Figure 27 shows that the second loadings start almost at the same position in the ice sheet for different indentor velocities. The size of the damage zone caused by the first peak loading is about the same even when the indentor velocities are different.

The maximum effective pressure, defined as the maximum ice force divided by the contact area, is plotted with respect to the indentation rate v/d (v = indentor velocity, d = indentor width) in Figure 28. We can see a trend of the maximum effective pressure slightly increasing with the increase in indentation rate v/d, which is in the range of 0.01 and 0.18 1/s.

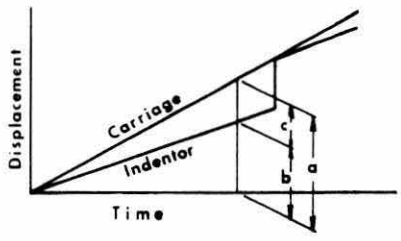

Figure 23. Sketch explaining the displacement records shown in Figure 22: a—*displacement of the carriage;* b—*displacement of the indentor with respect to the ice sheet;* c—*deformation of the structure.*

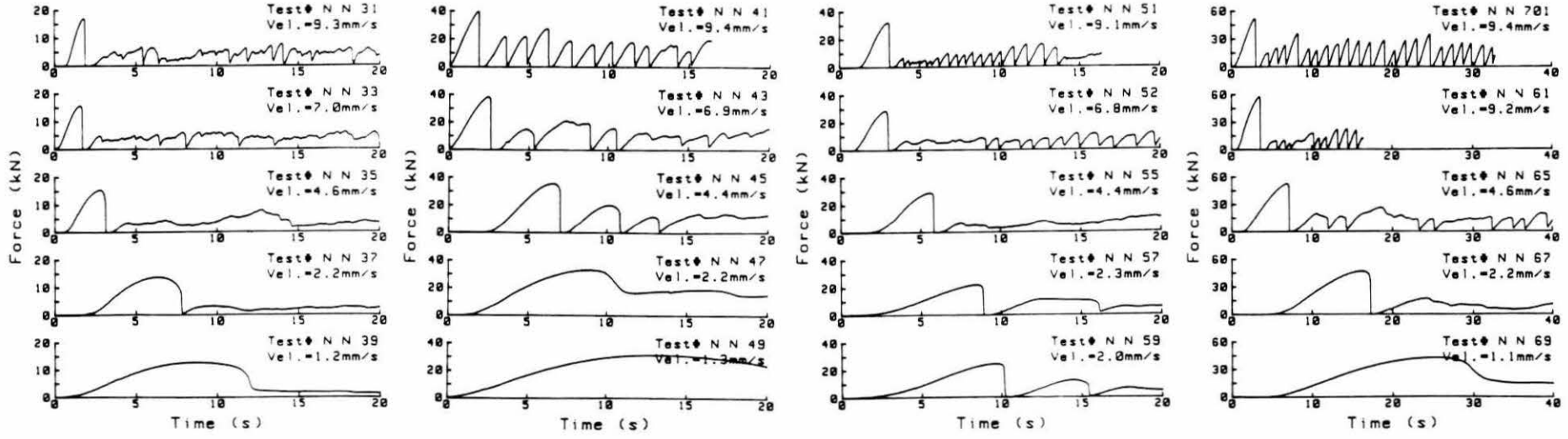

a. d = *50 mm and* h = *27 mm.* *b.* d = *50 mm and* h = *60 mm.* *c.* d = *100 mm and* h = *33 mm.* *d.* d = *100 mm and* h = *55 mm.*

Figure 24. Ice force versus time records at different velocities.

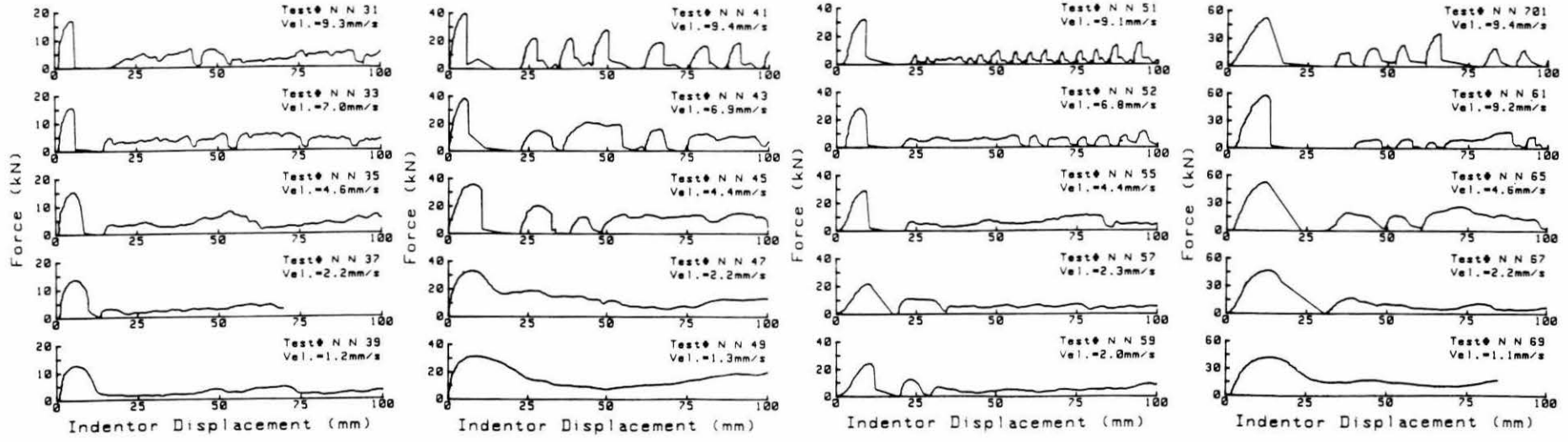

a. d = *50 mm and* h = *27 mm.* *b.* d = *50 mm and* h = *60 mm.* *c.* d = *100 mm and* h = *33 mm.* *d.* d = *100 mm and* h = *55 mm.*

Figure 25. Ice force versus indentor displacement records at different velocities.

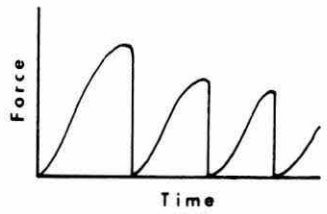

a. Brittle failure; saw tooth type records with force going to zero after each failure.

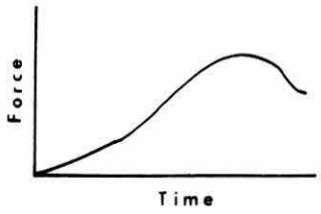

b. Ductile failure; rounded ice force curve with force not going to zero.

Figure 26. Typical ice force records.

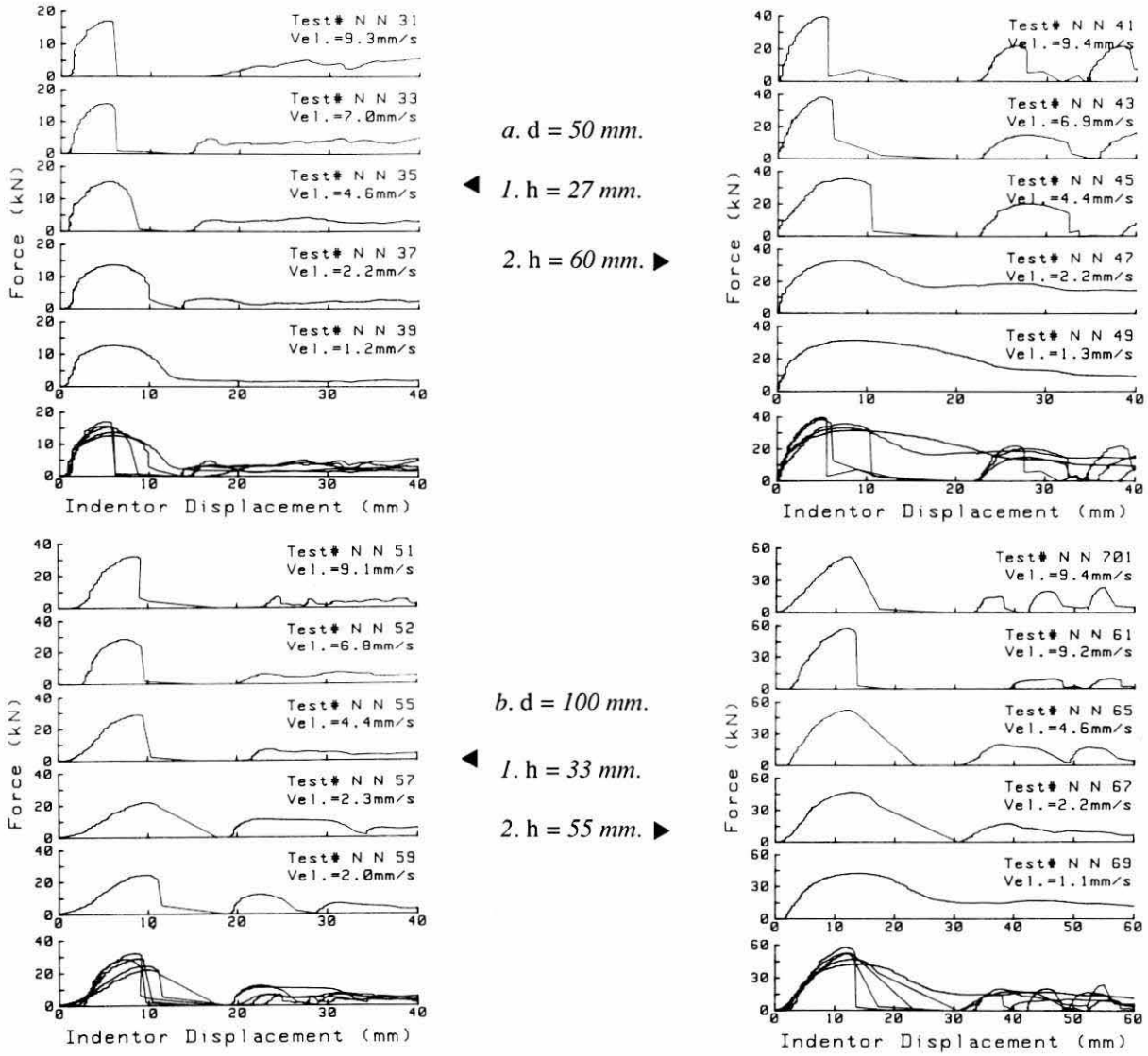

Figure 27. Comparison of ice force versus indentor displacement records up to the first few peaks at different velocities. The upper five plots show separately the records for different velocities; the bottom plot shows the records together.

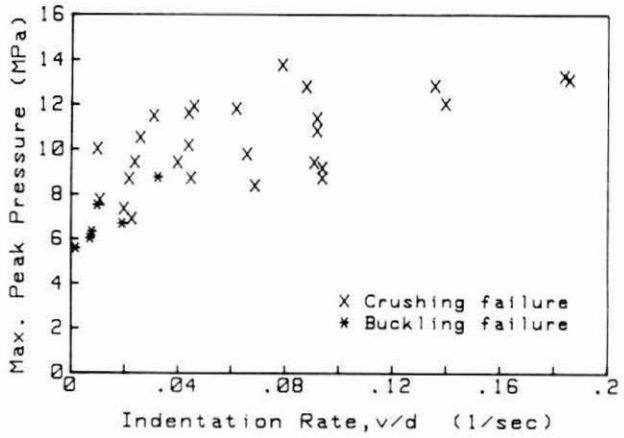

◀ *Figure 28. Maximum peak pressure* F/dh *versus indentation rate* v/d.

Figure 29. Comparison of indentation pressure versus indentation rate v/d *with those from other small-scale data measured in the laboratory (from Sanderson 1988).*

▼

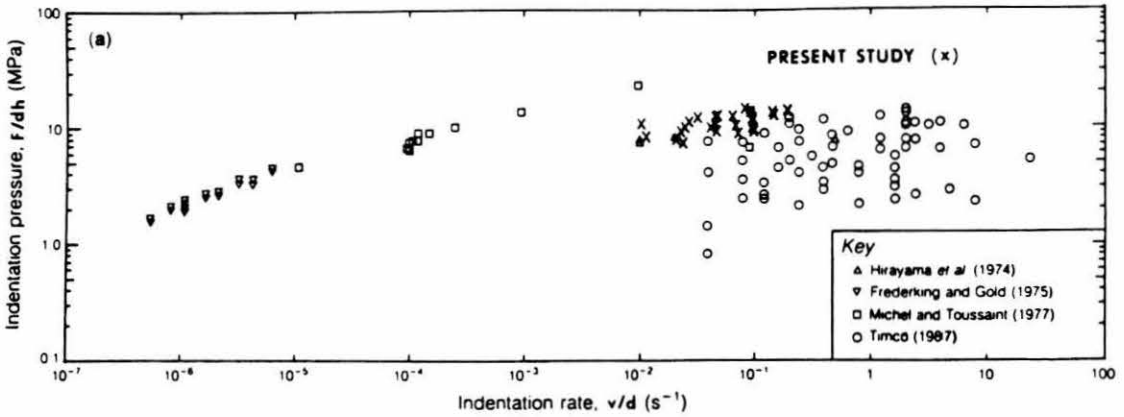

In Figure 29, plots of maximum effective pressure versus indentation rate obtained from the present study are compared with those from other studies on laboratory ice (Hirayama et al. 1974, Frederking and Gold 1975, Michel and Toussaint 1977, Timco 1987). We obtained an average value for maximum effective pressure of about 10 MPa, which is consistent with the results of the previous studies.

Energy analysis

Energy supplied to the carriage by the drive screw is partly stored in the structure and partly dissipated in the ice. Energy stored in the structure results in the deformation of the structure, and the energy dissipated in the ice causes deformation and microcracking in the ice. The force generated at the interface is the same as that which deforms the ice, deflects the structure and moves the carriage. Because the displacements of the carriage and the indentor were measured separately with respect to a fixed datum, the energies supplied to the carriage and dissipated in the ice can be computed independently. The energy stored in the structure is computed as the difference between the energy supplied to the carriage and the energy dissipated in the ice.

Figure 30 shows measured ice force and displacements data and computed energy transfers for indentor velocities of 9.4 and 1.3 mm/s respectively. It shows plots of the following: (from the top) the ice force; the displacements of the carriage and the indentor; the energies supplied to the carriage, dissipated in the ice and stored in the structure; and the rates of energy supplied to the carriage, stored in the structure and dissipated in the ice with respect to the time. Energy supplied to the carriage was calculated by integrating the product of the ice force and the incremental carriage displacement. Energy dissipated in the ice sheet was calculated by integrating the product of the ice force and the incremental indentor displacement. Energy stored in the structure was calculated by subtracting the energy dissipated in the ice from the energy supplied to the carriage. We calculated energy rates by multiplying the force with the corresponding velocities, which in turn were obtained by fitting a polynomial through the displacement data by the method of least-squares and then differentiating the fitted polynomial with respect to time.

From the initial contact to a peak force, a portion of the energy from the carriage is stored in the structure as the structure deforms as a result of the interaction force. During a test at high indentor velocity (e.g., 9.4 mm/s,

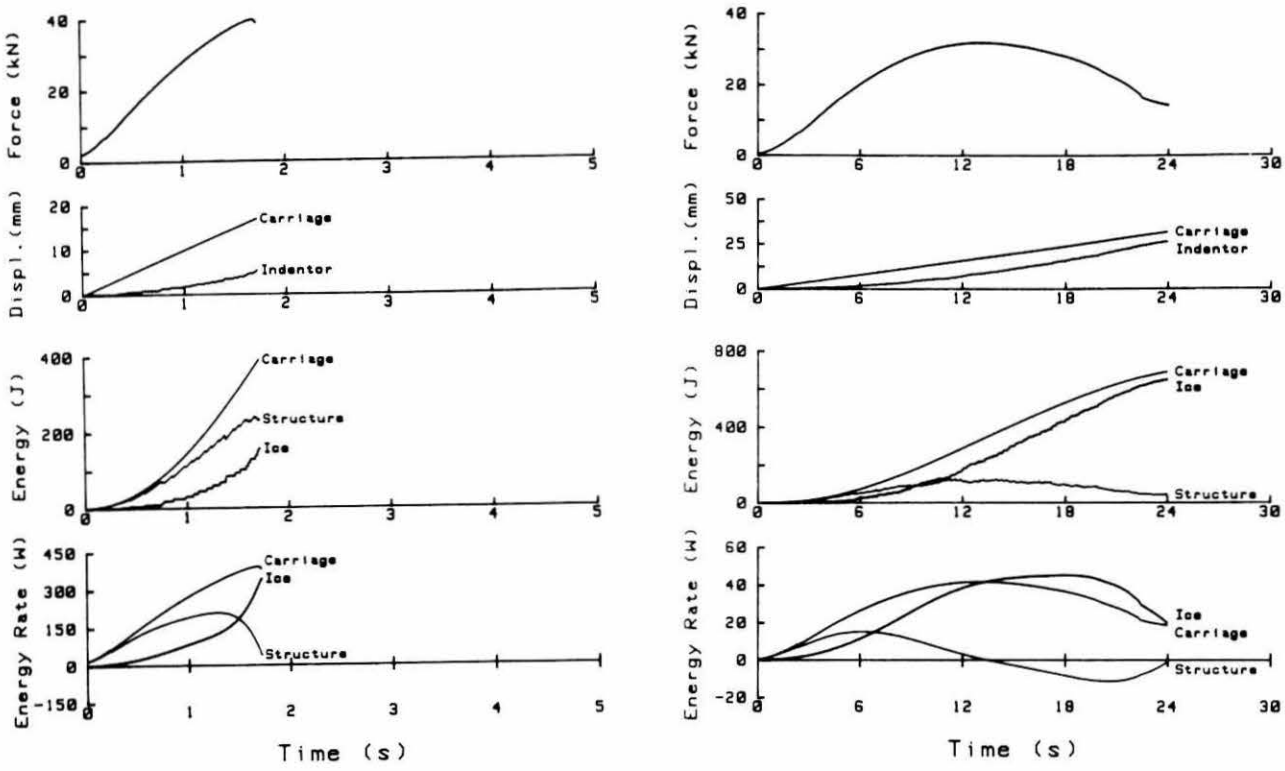

a. Test N N 41, v = 9.4 mm/s.

b. Test N N 49, v = 1.3 mm/s.

Figure 30. Energy and energy-rate plots (d = 50 mm and h = 60 mm).

Fig. 30a), the energies stored in the structure and dissipated in the ice increase with the elapsed time until the force reaches a maximum value. At this time, the energy stored in the structure is greater than that dissipated in the ice. This means that the deformation of the structure is larger than the displacement of the indentor relative to the ice sheet until the ice fails.

During a test at low velocity (e.g., 1.3 mm/s, Fig. 30b), the energy in the structure and in the ice increases with the elapsed time, but the energy dissipated in the ice is greater than that stored in the structure. This means that the displacement of the indentor relative to the ice sheet is greater than the deformation of the structure during the first loading.

The rates of energy supplied to the carriage, stored in the indentor structure and dissipated in the ice are shown at the bottom of Figure 30. For a test with high indentor velocity (v = 9.4 mm/s), the rate of energy dissipated in the ice is low and gradually increases with the elapsed time; the curve becomes steep at the time of the ice failure. For a test with low indentor velocity (v = 1.3 mm/s), the rate of energy dissipated in the ice is much greater than that stored in the structure, and it is even greater than that supplied to the carriage after the force peaks and the structure unloads. The negative values for the rate of energy stored in the structure means that the structure gradually swings back to its original position, thereby losing its stored energy.

Appendix A presents 20 plots showing measured data and computed energy transfers (Fig. A92–A111).

Figure 31 shows plots of time versus dissipation energy in the ice up to the first peak in ice force for different indentor velocities. In each test series, it should be noted, once again, that the energy used to produce the peak force is almost the same, even when the indentor velocity is different. The reason for this result can be seen in the force–displacement records shown in Figure 27. With the lower indentor velocity, the the peak forces are slightly smaller, and these occur slightly to the left, resulting in a constant area under the force–displacement plots. In other words, although the peak force and the displacement of the indentor are different at different indentor velocities, the energy dissipated in the ice up to the first peak in force is almost the same if indentor width, ice thickness and structural stiffness are the same.

Rates of energy dissipated in the ice up to the first peak in force for different indentor velocities are plotted

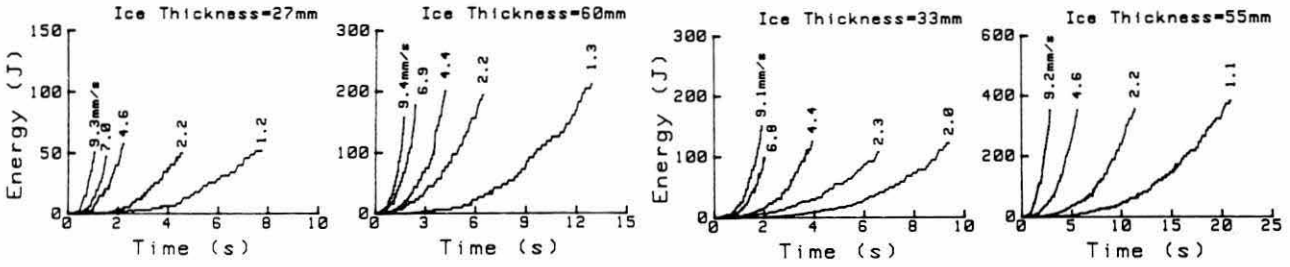

a. d = *50 mm.* *b.* d = *100 mm.*

Figure 31. Energy dissipated in the ice versus time for different indentor velocities (number at the top of each plot).

in Figure 32 for each test series. Each plot shows that the rate of energy dissipated in the ice increases with the elapsed time. For tests at high indentor velocity ($v > 4$ mm/s), the rate increases rapidly with the elapsed time. The rates are much lower for tests at low indentor velocity ($v < 3$ mm/s) and attain a steady-state value as opposed to the steep rise observed for high-velocity tests. This high rate of energy dissipation at high indentor velocity leads to instability, which is commonly called brittle failure of ice. The low rate of energy dissipation in the ice at low indentor velocities leads to gradual unloading of the indentor, which is commonly called the ductile failure of the ice.

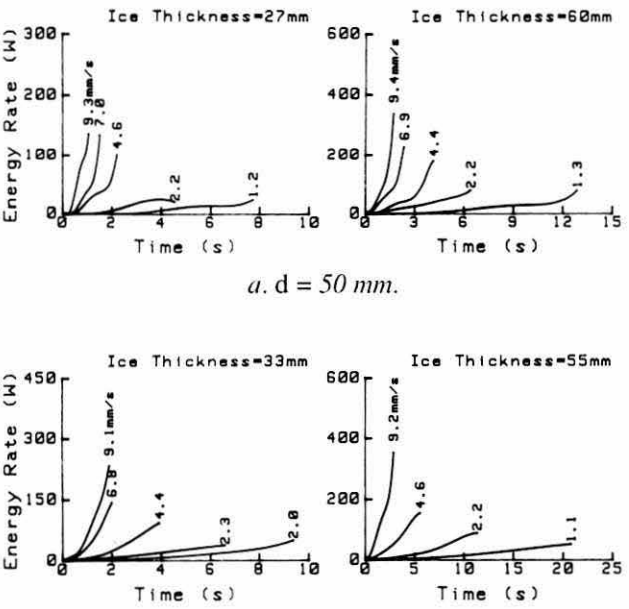

a. d = *50 mm.*

b. d = *100 mm.*

Figure 32. Energy rate dissipated in the ice versus time for different indentor velocities (number at the top of each plot).

Ice pressure and contact area

From a wide range of earlier experiments on the indentation of ice, it is known that the effective pressure decreases with increasing aspect ratio or contact area. Ice in the laboratory fails at 10–20 MPa and yet at large scale in the field it appears to fail at about 1 MPa. It is clear that, for some reason, failure pressure depends on contact area (Sanderson 1986).

First, the effective pressures obtained from this study were examined to see whether they followed any trend. Second, the pressure transducer records were analyzed to see if there was non-simultaneous failure across the contact area.

Contact area effects

Figure 33 shows the plots of the maximum effective pressure p ($= F/dh$, where F = total force, d = indentor width and h = ice thickness) as a function of contact area ($d \times h$) from the present study for indentor widths of d = 50, 100 and 150 mm. The test data do not show any trend of decreasing ice pressure with increasing contact area, probably because of the small variations in contact

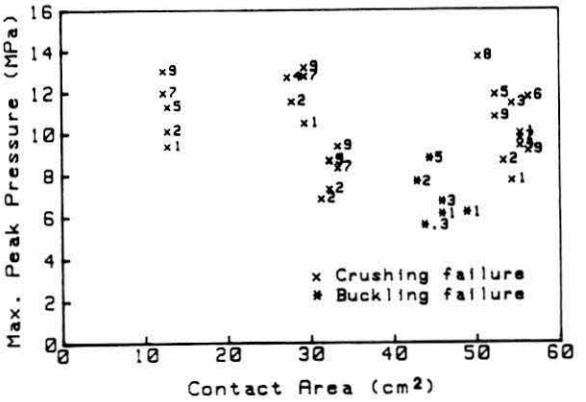

Figure 33. Maximum peak pressure versus contact area in the present study. The numbers beside each point are the indentor velocity in millimeters per second.

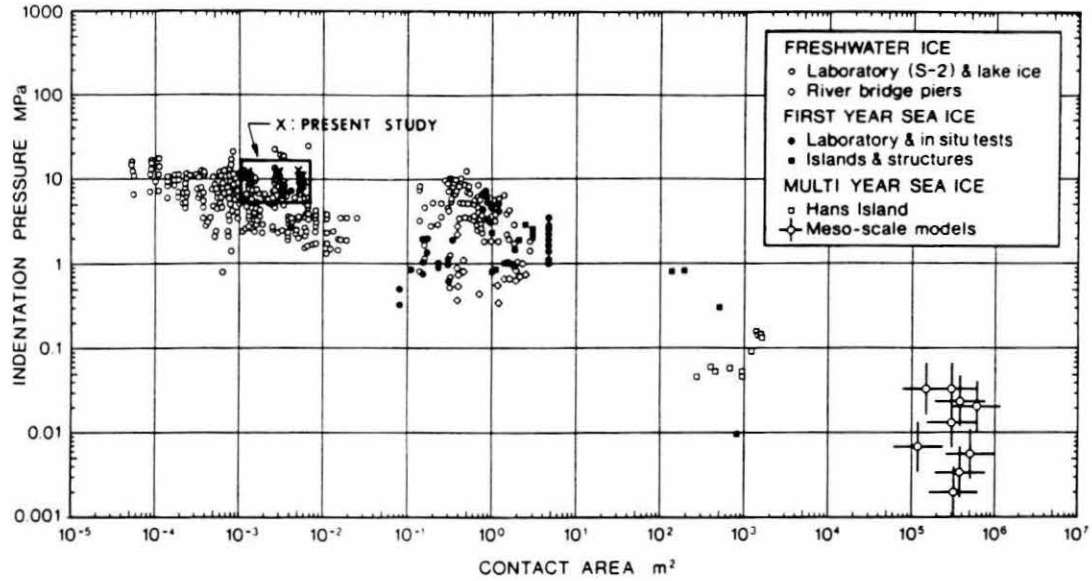

Figure 34. Comparison of our results with those compiled by Sanderson (1988).

area in our tests. However, the data do show that the effective pressure decreases with decreasing velocity for the same contact area.

In Figure 34, the effective pressure is plotted with respect to contact area for a wide range of ice–structure geometries and structure widths (from Sanderson 1988). Similarly, peak effective pressure is plotted with respect to the aspect ratio d/h in Figure 35 for indentation tests conducted on freshwater ice (Timco 1987). The data obtained from this study are also plotted in those figures for comparison, and they compare well with those from other studies.

Simultaneous versus non-simultaneous failure

Some of the pressure transducers failed, because of overloading, during the course of the experiment. Thus, limited data on interfacial pressure between the ice and the indentor were obtained by the pressure transducers.

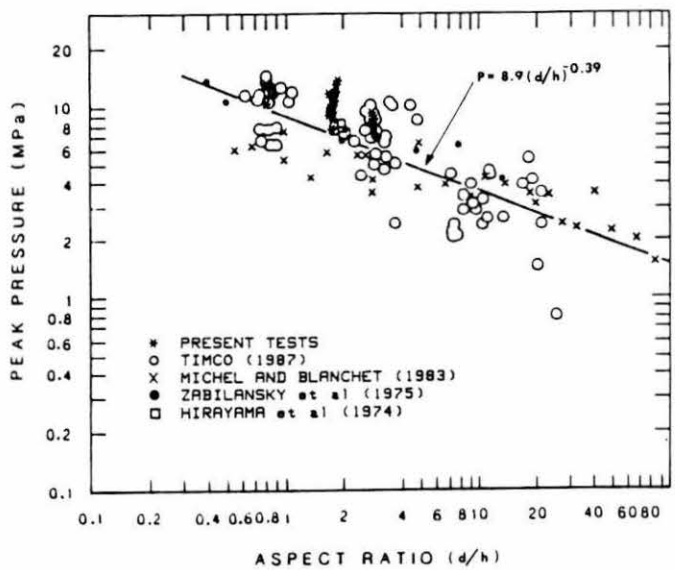

Figure 35. Maximum peak pressure versus aspect ratio for all published tests that used a flat indentor at a high loading rate (after Timco 1987).

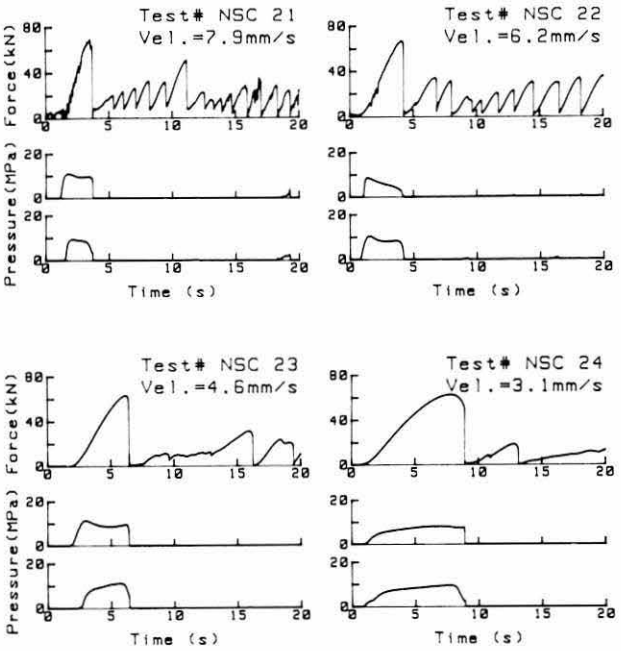

Figure 36. Measured pressure records along with force records, d = *100 mm and* h = *54 mm at different velocities.*

Figure 36 shows the pressure transducer records along with the ice force records for tests in which the indentor width was 100 mm and ice thickness 54 mm. The velocity range in this figure is between 3.1 and 7.9 mm/s. Nearly uniform pressure distribution can be seen during initial contact of the indentor with the edge of an ice sheet. In a few tests, the interfacial pressure increased to a certain value (approximately 10 MPa in Fig. 36) soon after the indentor contacted the ice and remained more or less constant while the ice force increased gradually until the ice failed.

A number of pressure transducer records are included in NSC test sheets in Appendix A. Although some of the records show non-simultaneous crushing behavior, we believe that pressure data from more pressure transducers will be needed to ascertain the non-simultaneous failure of ice from the pressure distribution.

Position of resultant force

As mentioned earlier, the indentor plate was mounted on three load cells after the change in the experimental setup. Mounting the indentor plate directly on the load cells is a better way to measure the interaction force than that by instrumenting the structural support. This setup allowed us to obtain not only the total ice force by summing the three ice forces obtained from the load cells but also the position of the resultant force in the contact area.

The positions of the resultant force were calculated by the following equations

$$x = \frac{F_1 - F_2}{2(F_1+F_2+F_3)} B$$

$$y = \frac{F_3}{F_1+F_2+F_3} H$$

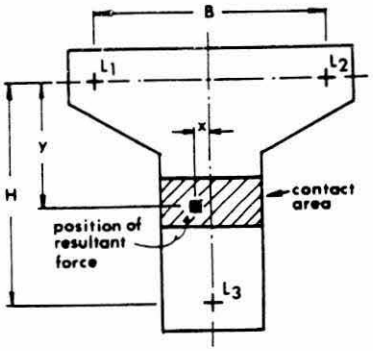

where F_1, F_2 and F_3 = ice force measured by load cells L_1, L_2 and L_3

B = horizontal distance between load cells L_1 and L_2

H = vertical distance between the L_1–L_2 line and L_3.

The calculated positions of the resultant force within the contact area are plotted in Figure 37 for the total force exceeding certain threshold values: 5 kN in Fig. 37a, 15 kN in Fig. 37b, 10 kN in Fig. 37c and 30 kN in Fig. 37d.

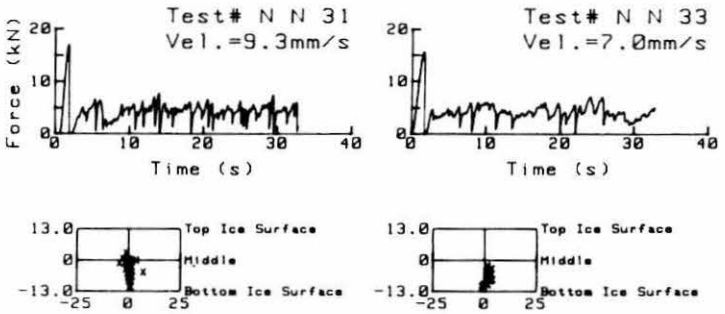

a. d = *50 mm*, h = *27 mm for resultant force* > *5 kN.*

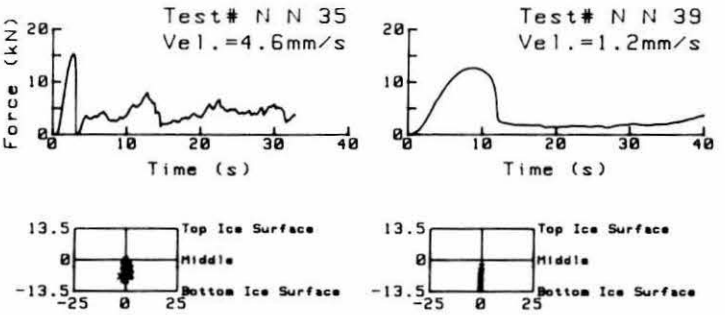

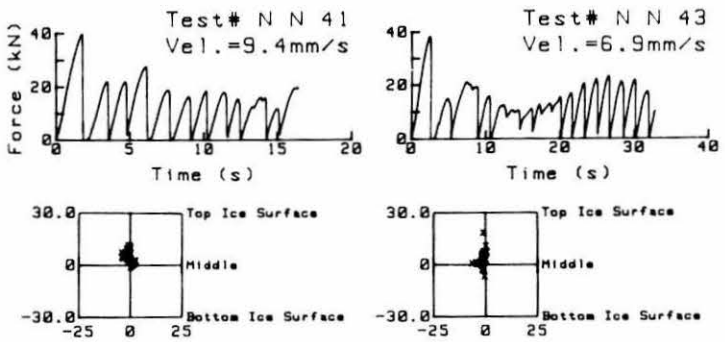

b. d = *50 mm*, h = *60 mm for resultant force* > *15 kN.*

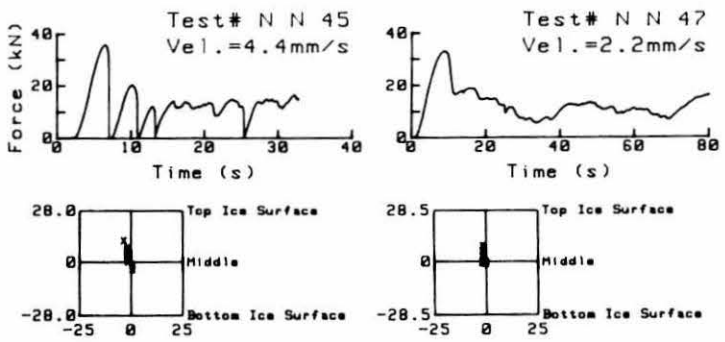

Figure 37. Resultant force position as determined from force measurements by three load cells (resultant forces are shown for each test on the upper graph).

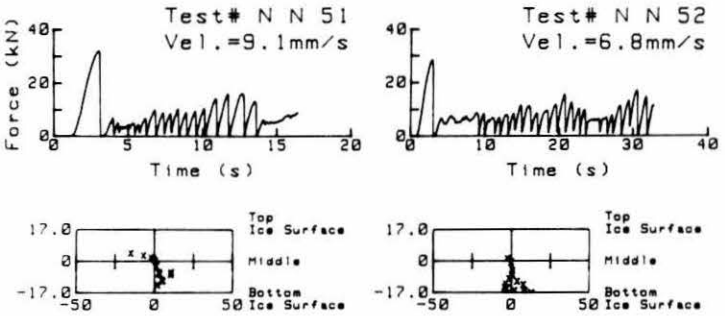

c. d = *100 mm*, h = *33 mm for resultant force > 10 kN.*

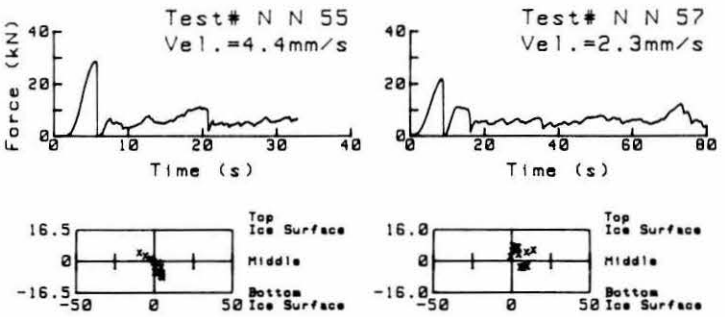

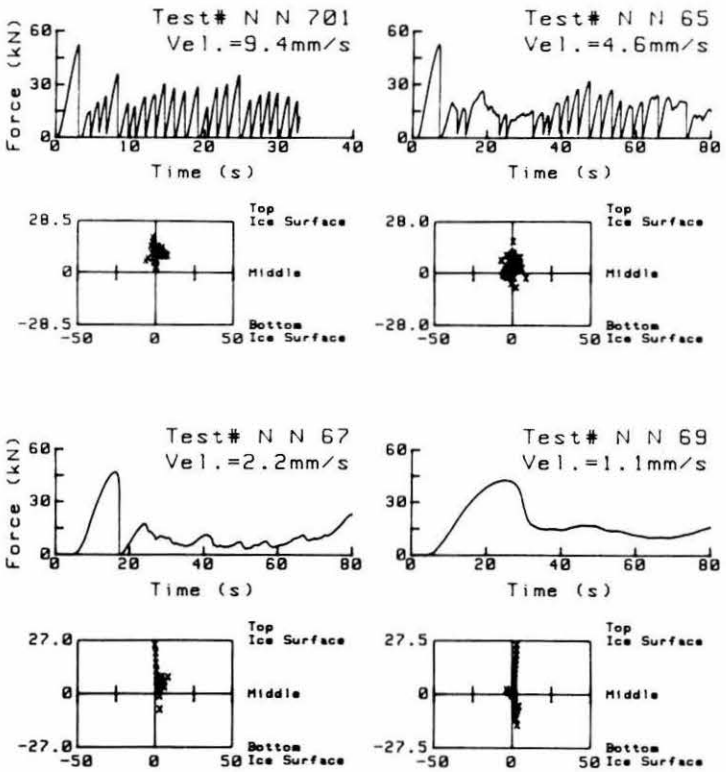

d. d = *100 mm*, h = *55 mm for resultant force > 30 kN.*

Figure 37 (cont'd). Resultant force position as determined from force measurements by three load cells (resultant forces are shown for each test on the upper graph).

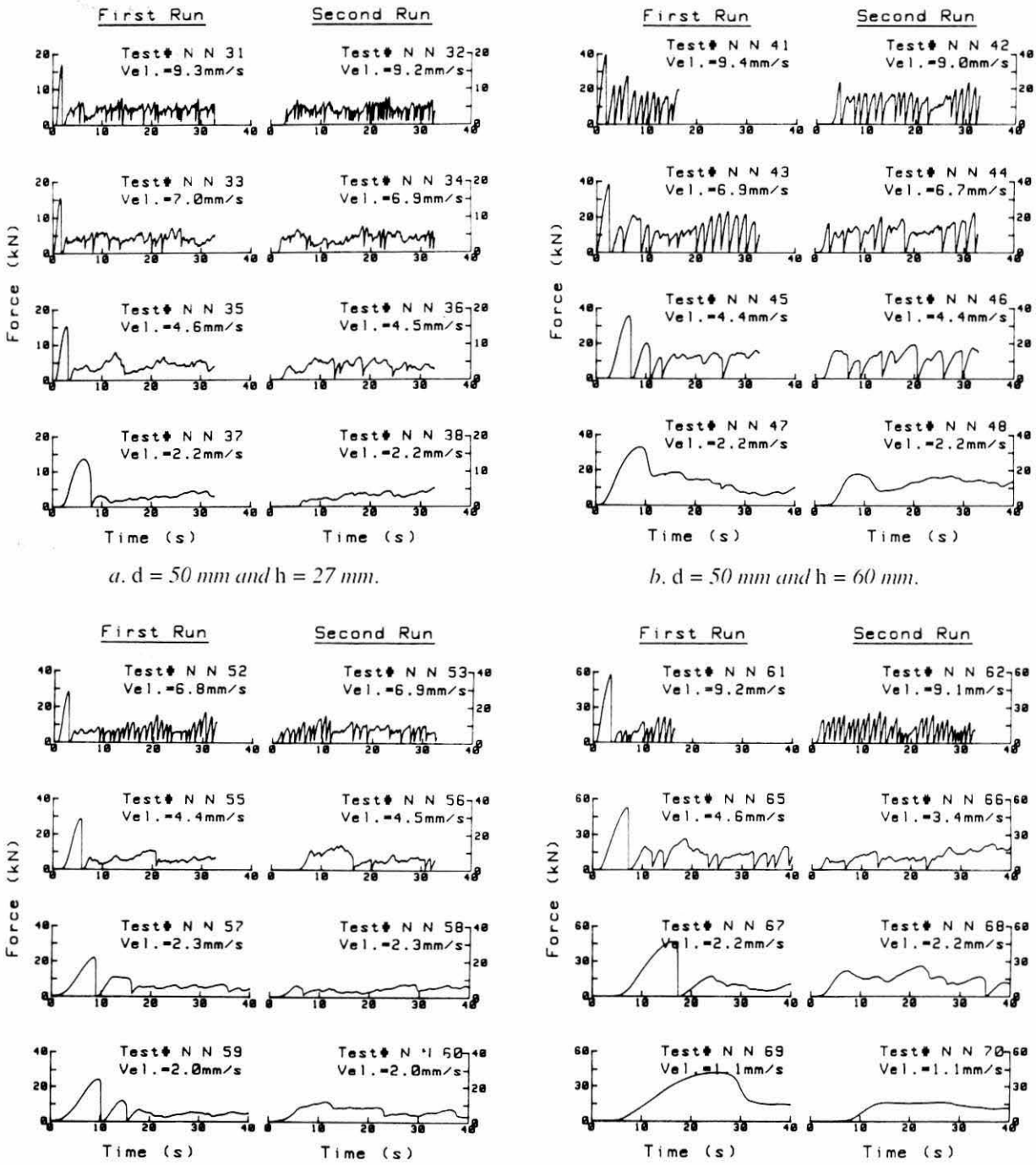

a. d = *50 mm and* h = *27 mm.*

b. d = *50 mm and* h = *60 mm.*

c. d = *100 mm and* h = *33 mm.*

d. d = *100 mm and* h = *55 mm.*

Figure 38. Ice force records at different velocities of first run and second run in the same track.

By monitoring the point of action of the resultant force, a few inferences can be made about the pressure distribution. A symmetrical pressure distribution would be indicated by the point of action of the resultant force being in the center of the contact area; otherwise, we would expect it to be in some other area of the contact zone. In the situation of a non-simultaneous ice failure, the position of the resultant force is expected to move from one part of the contact zone to another during continuous crushing of ice.

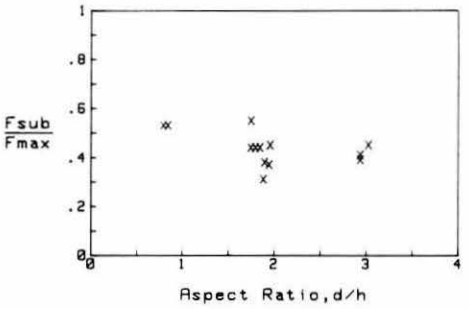

a. Aspect ratio d/h.

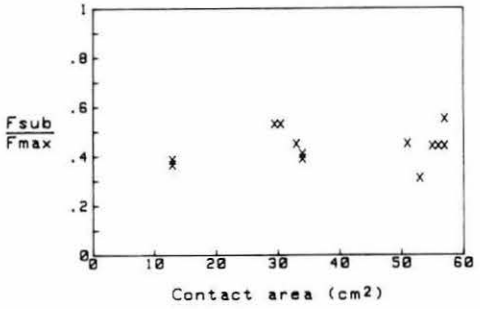

b. Contact area d × h .

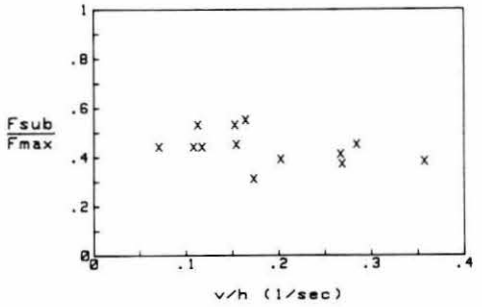

c. Ratio of indentor velocity to ice thickness v/h.

Figure 39. Ratio of the mean subsequent peak force to first peak force plotted versus d/h, d × h *and* v/h.

The plots of resultant force positions in Figure 37 show that the initial contact point between the indentor and the ice edge may not have been in the center of the contact area, but, as the load increased, the position of the resultant force moved to the center of the contact area. From our observations of the computer graphics during data analysis, we consistently saw the position of the resultant force move to the center of the contact zone as the ice force increased. These records indicate that, when the interaction forces are greater than the threshold force level, a symmetrical pressure distribution exists at the ice–indentor interface. It appears that the position of the resultant force at high velocity ($v > 4$ mm/s) is slightly scattered because of the cyclic brittle failure. At low velocities ($v < 3$ mm/s), the position is laterally centered but varies somewhat vertically. This may be attributed to the gradual loading and the ductile behavior of the ice, generating a symmetrical pressure distribution.

It should be noted that the uniformity of the ice pressure may be attributed to the small contact area in this testing program. Further studies employing larger contact areas should be conducted to investigate non-simultaneous failure of ice within the contact area.

First peak force versus subsequent peak force

We stated previously that eight to ten tests were conducted in pairs in four to five tracks in an ice sheet. Two tests were conducted in one test track at the same velocity to observe the magnitude of the ice force resulting from interaction with "undamaged" and "damaged" ice: the "first run" into undamaged ice and the "second run" into damaged ice.

The ice force records are shown in Figure 38. Tests N N 31 and N N 32 (Fig. 38a) were conducted in the same test track, as were N N 33 and N N 34 and so on. The first peak force in the first run was always the maximum force throughout each test. The first peak was generated by the interaction between the indentor and the undamaged (with no microcracks) ice sheet, and subsequent peak forces were generated by indentation into the damaged ice. In the second run, the peak forces were not as large as the first peak force in the first run. These lower peak forces in the second run can be attributed to the previous damage and microcracking present in ice caused during the first run.

The ratio of the average subsequent peak force to the first peak force (F_{sub}/F_{max}) is plotted with respect to the aspect ratio d/h in Figure 39a, the contact area $d \times h$ in Figure 39b and the velocity-to-thickness ratio v/h in Figure 39c. In each of three plots, the ratio F_{sub}/F_{max} is in the range of 0.3 to 0.6, and these plots show no increasing or decreasing trend.

Frequency of ice force failure

Analysis of the structural vibration caused by repeated ice failure is an important part of the design process. Peyton (1968) and Blenkarn (1970) reported on the vibrations of structures caused by ice movement in the Cook Inlet, Alaska. These structures were multi-legged drilling platforms that were instrumented to measure ice forces and structure response. Jefferies and Wright (1988) have reported on the ice-induced vibrations of *Molikpaq*, a large structure (116 × 116 m) that was placed on a 14-m-deep berm at the Amauligak

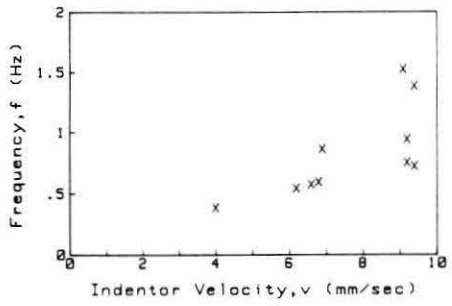

a. Indentor velocity v.

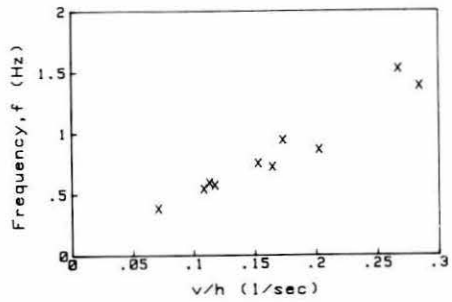

b. Ratio of velocity to ice thickness v/h.

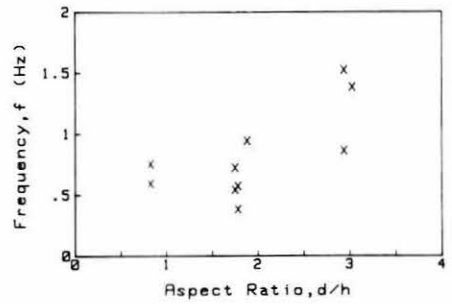

c. Aspect ratio d/h.

Figure 40. Ice failure frequency plotted versus v, v/h *and* d/h.

location. Määttänen (1975) conducted extensive measurement of the ice-induced vibrations of lighthouses in the Gulf of Bothnia.

As can be seen from the data in Figures 24 and 25, the interaction force between the indentor and the ice increases with time (or displacement) until the ice fails and is not able to resist the indentor. As has been demonstrated, depending on the velocity of the indentor, the failure in the ice sheet is either brittle or ductile. For brittle failure of ice at high indentor velocity ($v > 4$ mm/s), there is sudden unloading of the indentor; thus, a brittle failure event in ice is associated with the increase of ice force and a sudden unloading.

After the ice failure, the indentor moves forward, extruding the crushed ice in front of it. The ice force does not rise until the indentor again contacts intact ice. The forward distance moved by the indentor during each failure event can be characterized as a damage zone caused by crushing. The data in Figure 25 indicate that the greater the ice force recorded, the farther the indentor moved forward. In other words, the size of damage zone during successive failure events depends on the magnitude of the ice force. But an average damage zone can be obtained by counting the number of peaks in the force–displacement record and dividing it by the total indentor displacement. An alternate procedure to arrive at the average damage zone is given below.

Frequencies of ice failure (f) in the brittle range, listed in Table 3, were calculated by counting the number of peaks divided by the elapsed time. These frequencies are plotted with respect to the indentor velocity in Figure 40a for all tests with brittle, repeated failures, showing a trend of increasing frequency with increasing velocity. However, the scatter in the plots increases with velocity. When the frequency is plotted with respect to the velocity-to-thickness ratio v/h (Fig. 40b), the variation in the data points reduces and the frequency increases linearly with increasing v/h. These trends are similar to those obtained by Sodhi and Morris (1984).

A plot of frequency versus the aspect ratio d/h is shown in Figure 40c. Although it seems that the frequency increases with increasing the aspect ratio, it is hard to ascertain this trend because of the small variations in the aspect ratio.

The nondimensional variable v/fh is the ratio of the damage zone to ice thickness, where v is the indentor velocity, h the ice thickness and f the frequency of ice failure. This number quantifies the distance that the indentor moves forward in each loading cycle in terms of ice thickness. Figure 41 shows the plots of v/fh versus the aspect ratio d/h and the velocity-to-thickness ratio v/h. The values of v/fh are in the range of 0.18 and 0.24. This means that the average movement of the indentor during each ice failure varies between 18 to 24% of the ice thickness. In both figures, v/fh remains constant as d/h or v/h increase. A nondimensional quantity, fh/v (similar to the Strouhal number for fluids), is calculated and listed in Table 3; it ranges between 4.37 and 5.68 in this test series.

Buckling failure

Tests with an indentor width of 150 mm and an ice thickness 30 mm resulted in buckling failure (tests N N 71 to N N 76 in Table 3).

Six nondimensional data points were plotted in Figure

42, in which theoretical results from a finite element analysis by Sodhi (1979) are also plotted for hinged and frictionless boundary conditions. The ordinate in Figure 42 is a nondimensional buckling pressure F/dKL^2 (F is ice force, d is the structure width, K is the specific weight of water and L is the characteristic length of the ice sheet) and the abscissa is the ratio of the indentor width to the characteristic length of the ice sheet. The hinged boundary condition means that there is no relative displacement between the ice and the structure, and the frictionless boundary condition means that there is no frictional force when ice moves up or down relative to the structure. These two boundary conditions represent the extreme situations possible in the experiments, because the actual boundary condition falls between them.

All data except the test with the velocity of 5 mm/s lie in the zone between the hinged and frictionless conditions. With decreasing velocity, it seems that the nondimensional buckling pressure decreases, and that the boundary condition approaches the frictionless condition from the hinged condition.

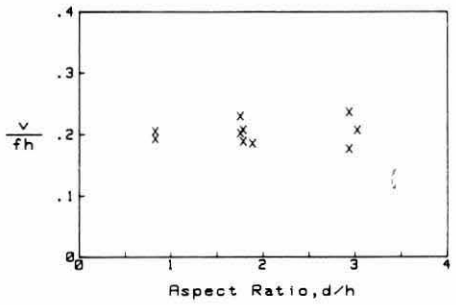

a. Aspect ratio d/h.

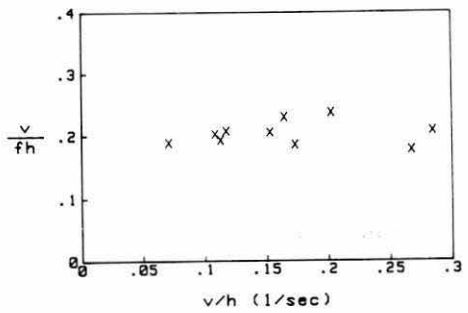

b. Ratio of velocity to thickness v/h.

Figure 41. Average indentor movement per ice failure cycle in terms of ice thickness versus d/h *and* v/h.

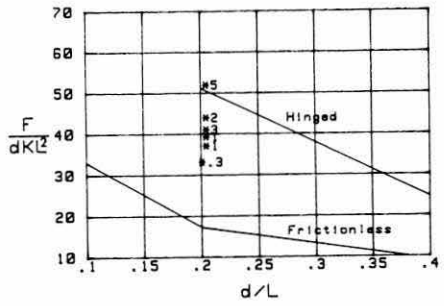

Figure 42. Nondimensional buckling force F/dKL² *as a function of* d/L *(indentor width* d = *150 mm,* F = *ice force,* h = *ice thickness,* K = *9806 N/m and* L = *characteristic length). The number beside each data point is indentor velocity in millimeters per second.*

SUMMARY

We conducted 92 indentation tests by pushing vertical, flat indentors through freshwater, columnar, floating ice sheets. To observe the failure modes and to characterize the magnitude and nature of the ice forces, new methodology was adopted for conducting these tests. For instance, forces were measured by supporting the indentor on three load cells; the displacements of the carriage and the indentor were measured separately to observe the transfer of energies from the carriage to the structure and the ice; AEs were also measured and correlated with measured ice force. The indentor width was varied from 50 to 150 mm, the relative velocity of the indentor from 1 to 9 mm/s, and the ice thickness from 20 to 60 mm.

Instrumentation

Although indentation tests have been conducted earlier by other researchers, there are a few salient features of this study that need to be pointed out.

Ice force measurement

The interaction ice force was measured in two ways: 1) by installing a load cell in the structural support, and 2) by mounting the indentor plate on three load cells. The second method provided the actual ice force that was generated between the ice and the indentor without being influenced by the deformation and vibration of the structure.

Indentor displacement

Displacements of both the carriage and the indentor were measured separately. A displacement transducer

placed on the floating ice sheet measured the relative motion of the indentor with respect to the ice sheet. This allowed us to compute the total energy supplied by the carriage and the energies dissipated in the ice and stored in the structure.

Acoustic emissions

Acoustic emissions were recorded during the tests, and these appear to be correlated to the microcracking activities in the ice and the ice force. The cumulative AE count increases with increasing ice force.

Test results

Microcracks

At the onset of loading, microcracks immediately formed in front of the indentor, and this zone of microcracks expanded until the ice failed. During high velocity tests ($v > 4$ mm/s), we observed spurts of microcracking prior to each ice failure event. Microcracks developed in the ice ahead of the indentor during the time when the indentor was being loaded, and then the indentor moved forward very quickly, crushing or spalling the previously damaged (microcracked) ice.

Macrocracks

Several macrocracks were observed, i.e., radial cracks, circumferential cracks and in-plane cleavage cracks. A number of radial and circumferential cracks nucleated during the first loading and failure of the ice.

Velocity effects

Depending on the relative velocity of the indentor, ice behavior was either ductile or brittle. Brittle behavior resulted in the sudden unloading of the indentor, which moved back to its original undeformed position, relative to the carriage, with crushing or spalling of the damaged, microcracked ice. Ductile deformation resulted in gradual loading and unloading of the indentor. It appears that, even for different indentor velocities, the indentor displacements at the time when the peak ice force occurs are almost the same. In addition, the size of the damaged ice zone during the first loading of the indentor is about the same even when the indentor velocities are different.

Energy analysis

During the ice–structure interaction, energy supplied to the carriage by the drive-screw is partly stored in the structure and partly dissipated in the ice as a result of deformation and microcracking in the ice. During tests at high indentor velocity ($v > 4$ mm/s), the energy stored in the structure is greater than that dissipated in the ice. This means that the deformation of the structure is larger than the displacement of the indentor relative to the ice sheet until the ice fails. During tests at low velocity ($v < 3$ mm/s), the energies stored in the structure and dissipated in the ice increase with the elapsed time, but the energy dissipated in the ice is greater than that stored in the structure. This means that the displacement of the indentor relative to the ice sheet is greater than the deformation of the structure during the first loading.

For tests with high indentor velocity ($v > 4$ mm/s), the rate of energy dissipated in the ice gradually increases with the elapsed time, and the curve becomes steep at the time of the ice failure. For tests with low indentor velocity, the rate of energy dissipated in the ice is much greater than that stored in the structure, and it is even greater than that supplied to the carriage after a peak in the force record occurs and the structure unloads. The negative values for the rate of energy stored in the structure means that the structure gradually swings back to its original position, thereby losing its stored energy.

The energy used to produce the peak force is almost the same even for different indentor velocities. In other words, though the peak force and the displacement of the indentor are different at different indentor velocities, the energy dissipated in the ice up to the first peak in force is almost the same if other conditions are the same.

For tests at high indentor velocities ($v > 4$ mm/s), the rate of energy supplied by the carriage exceeds that dissipated in the ice; the rest is stored in the structure. As the rate of energy dissipated in the ice increases with the elapsed time, ice is weakened by microcracks, and the ability of the ice to absorb more energy decreases with elapsed time. Just before the peak ice force, the rate of energy supplied to the ice from the carriage and the structure increases rapidly with the elapsed time, leading to an instability, which is commonly called the brittle failure of ice. These rates are much lower for tests at low indentor velocity ($v < 3$ mm/s) than for tests at high velocity and attain a steady-state value as opposed to the steep rise observed in high-velocity tests. The low rate of energy dissipation in the ice at low indentor velocity leads to a gradual unloading of the indentor in a stable manner, which is commonly called the ductile failure of the ice.

Simultaneous versus non-simultaneous failure

Because the pressure transducers were damaged during the tests, the pressure distribution could not be determined for all the tests. From the limited data obtained from these transducers, we found that a nearly uniform pressure distribution develops during the initial contact of the indentor with the edge of an ice sheet.

In a few tests, the interfacial pressure increased to a high value soon after the indentor contacted the ice and then remained more or less constant while the ice force increased gradually until the ice failed. More tests with wider structures need to be done to determine whether ice fails at different times in different parts of the contact area.

Position of resultant force

In many of the tests, the interaction forces were measured by supporting the indentor plate on three load cells. This enabled us to compute the position of the resultant force. We were looking for a symmetrical pressure distribution where the resultant force would remain in the center of the contact area. The initial contact point between the indentor and the ice edge may not have been in the center of the contact area, but as the load increased, the position of the resultant force moved to the center of the contact area, indicating a uniform or symmetrical pressure distribution at the interface.

First peak force and subsequent peak force

First peak forces were always greater than the subsequent peak forces, which were between 30 to 60% of the first peak force. We attribute this to the fact that ice offers less resistance to indentation as a result of previous deformation and microcracking. The undamaged ice offers maximum resistance, thereby resulting in a higher interaction force.

Frequency of ice force failure

The frequency of ice failure increased with the increase in the ratio of velocity to ice thickness. Using the velocity and frequency data, we calculated the distance of indentor movement for each ice failure; it was between 0.18 and 0.24 times the ice thickness.

Buckling failure

The ice sheets buckled during the tests when the indentor width was 150 mm. The nondimensional buckling load was found to be between those predicted by theoretical results for frictionless and hinged boundary conditions. Experimental results were closer to those for the hinged boundary condition, and these decreased with decreasing indentor velocity.

Scope of future work

The data obtained in this study provided us with many interesting results that were only possible because of the new methodology used to measure ice forces and the measurements of carriage and indentor displacement, separately, with respect to a fixed datum. Therefore, we recommend that all future experimental studies of this nature also measure forces and displacements in a similar manner. The following is a list of studies that we believe should be conducted for a better understanding of ice–structure interactions.

1. Through the course of study, our observations of the deformation of the structure during the ice loading showed us that the stiffness of the structure is an important parameter during ice crushing. The frequency of the ice failure may depend on the structural stiffness. Thus, it is recommended that the influence of the structural stiffness to the ice–structure interaction be investigated.

2. Observations of the structural response at the time of ice crushing are needed to understand the force–displacement relationship.

3. Microcracking and energy/energy-rate dissipation relationships in the ice should be studied for a better understanding of the ductile and brittle behavior of the ice.

4. Further studies of non-simultaneous failure in the ice–structure contact area should be conducted to determine the influence of the contact area on the magnitude of the ice force.

LITERATURE CITED

Blanchet, D. (1987) Variations of the local failure pressure with depth through first-year and multi-year ice. *ASME Journal of Offshore Mechanics and Arctic Engineering*, **110**(2): 159–168.

Blenkarn, K.A. (1970) Measurement and analysis of ice forces on Cook Inlet structures. In *Proceedings of 2nd Offshore Technology Conference, Houston, Texas* (OTC 1261), vol. 2, p. 365–378.

Croasdale, K.R., N.R. Morgenstern and J.B. Nuttall (1977) Indentation tests to investigate ice pressures on vertical piers. *Journal of Glaciology*, **19**(81): 301–312.

Forland, K.A. and J-C. Tatinclaux (1984) Laboratory investigation of the kinetic friction coefficient of ice. In *IAHR Ice Symposium, Proceedings. Hamburg, West Germany, August*, vol. 1, p. 19–28.

Frederking, R. and L.W. Gold (1975) Experimental study of edge loading of ice plates. *Canadian Geotechnical Journal*, **12**(4):456–463.

Hirayama, K., J. Schwarz and H.C. Wu (1974) An investigation of ice forces on vertical structures. IIHR Report No.158. Iowa City: University of Iowa.

Jefferies, M.G. and W.H. Wright (1988) Dynamic response of "MOLIKPAQ" to ice–structure interaction. In *Proceedings of International Conference on Offshore Mechanics and Arctic Engineering, Houston, Texas*, p. 201–220.

Kato, K. and D.S. Sodhi (1984) Ice action on two cylindrical structures. *Journal of Energy Resources Technology ASME*, **106**: 107–112.

Kendall, K. (1978) Complexities of compression failure.

Proceedings of the Royal Society (London), **Ser. A361**: 245–263.

Kry, P.R. (1979) Stress distribution during continuous crushing of ice. Calgary: Arctic Petroleum Operators' Association, APOA Project No.148.

Kry, P.R. (1978) A statistical prediction of effective ice crushing stresses on wide structures. In *Proceedings, IAHR Symposium on Ice Problems, Luleä, Sweden*. Part I, p. 33–47.

Määttänen, M. (1975) Experiences of ice forces against a steel lighthouse mounted on the seabed, and proposed constructional refinements. In *Proceedings, 3rd International Conference on Port and Ocean Engineering under Arctic Conditions (POAC'75), Fairbanks, Alaska*, vol. 2, p. 857–869.

Michel, B. and N. Toussaint (1977) Mechanisms and theory of indentation of ice plates. *Journal of Glaciology*, **19**(81): 285–300.

Michel, B. and D. Blanchet (1983) Indentation of an S2 floating ice sheet in the brittle range. *Annals of Glaciology*, **4**: 180–187.

Neill, C. (1976) Dynamic ice forces on piers and piles: an assessment of design guide lines in the light of recent research. *Canadian Journal of Civil Engineering*, **3**(2): 305–341.

Oksanen, P. (1980) Coefficient of friction between ice and some construction materials, plastics and coatings. Espoo: Technical Research Institute of Finland, Laboratory of Structural Engineering, Report 7.F.

Peyton, H.R. (1968) Sea ice forces. In *Ice Pressures Against Structures*. National Research Council of Canada, Technical Memorandum 92, p.117–123.

Saeki, H., K. Hamanaka and A. Ozaki (1977) Experimental study on ice force on a pile. In *Proceedings, 4th International Conference on Port and Ocean Engineering under Arctic Conditions (POAC '77), St. John's, Newfoundland, Canada*, p. 695–706.

Saeki, H. , K. Hamanaka and A. Ozaki (1986) The coefficient of friction between sea ice and various materials used in offshore structures. *ASME Journal of Energy Resources Technology*, **6**: 65–71.

Saeki, H. , K. Hamanaka and A. Ozaki (1988) Ice forces due to changes in water level and adfreeze bond strength between sea ice and various materials. *ASME Journal of Offshore Mechanics and Arctic Engineering*, **110**: 74-80.

Sanderson, T.J.O. (1986) A pressure–area curve for ice. In *Proceedings, IAHR Ice Symposium 1986, Iowa City, Iowa*, vol. 2, p. 361–384.

Sanderson, T.J.O. (1988) *Ice Mechanics—Risk to Offshore Structures*. London: Graham & Trotman.

Schwarz, J. (1970) The pressure of floating ice-fields on pile. In *Proceedings, IAHR Symposium on Ice, Reykjavik, Iceland*, section 6.3, p. 1–12.

Sinha, N.K. (1983) Creep model of ice for monotonically increasing stress. *Cold Regions Science and Technology*, **8**: 25–33.

Sinha, N.K. (1984) Delayed-elastic model for initiation and accumulation of creep cavitation at high temperature. In *Proceedings of 6th International Conference on Fracture (ICF6), New Delhi, India*, p. 2295–2302.

Sodhi, D.S. (1979) Buckling analysis of wedge-shaped floating ice sheets. In *Proceedings, 5th International Conference on Port and Ocean Engineering under Arctic Conditions (POAC '79), Trondheim, Norway*, p. 797–810.

Sodhi, D.S., K. Kato, F.D. Haynes and K. Hirayama (1982) Determining the characteristic length of model ice sheets. *Cold Regions Science and Technology*, **6**: 99–104.

Sodhi, D.S. and C.E. Morris (1984) Ice forces on rigid, vertical, cylindrical structures. USA Cold Regions Research and Engineering Laboratory, CRREL Report 84-33.

Tusima, K. and T. Tabata (1979) Friction measurements of sea ice on flat plates metals, plastics and coatings. In *Proceedings, 5th International Conference on Port and Ocean Engineering Under Arctic Conditions (POAC'79), Trondheim, Norway*, vol. 1, p. 741–755.

Tanaka, S., H. Saeki and T. Ono (1987) The distribution of ice pressure acting on offshore pile structure and the failure mechanics of ice sheet. *ASME Journal of Offshore Mechanics and Arctic Engineering*, **109**(1): 85–92.

Timco, G.W. (1987) Indentation and penetration of edge-loaded freshwater ice sheets in the brittle range. *ASME Journal of Offshore Mechanics and Arctic Engineering*, **109**(3): 287–294.

Tunik, A. (1987) Impact ice loads on offshore structures. In *Proceedings, 9th International Conference on Port and Ocean Engineering Under Arctic Conditions (POAC'87), Fairbanks, Alaska*, p. 485–493.

Wyman, M. (1950) Deflection of an infinite plate. *Canadian Journal of Research*, **A28**: 293–302.

Weeks, W.F. and S.F. Ackley (1982) The growth, structure and properties of sea ice. USA Cold Regions Research and Engineering Laboratory, Monograph 82-1.

Weeks, W.F. and G.F.N. Cox (1984) The mechanical properties of sea ice: A status report. *Ocean Science and Engineering*, **9**(2): 135–198.

Wierzbicki, T. (1985) Spalling and buckling of ice sheets. In *Proceedings, Civil Engineering in the Arctic Offshore, ASCE Conference Arctic '85*, p. 953–961.

Zabilansky, L., D.E. Nevel and F.D. Haynes (1975) Ice forces on model structures. *Canadian Journal of Civil Engineering*, **2**(4): 400–417.

APPENDIX A: DATA

NSC test sheets

Each data sheet contains the following plots: tests 89 to 36—ice force versus time, indentor displacement versus time and ice pressure versus time; tests 29 to 16—ice force versus time, AE signal versus time, carriage and indentor displacement versus time, ice pressure versus time and ice force versus indentor displacement.

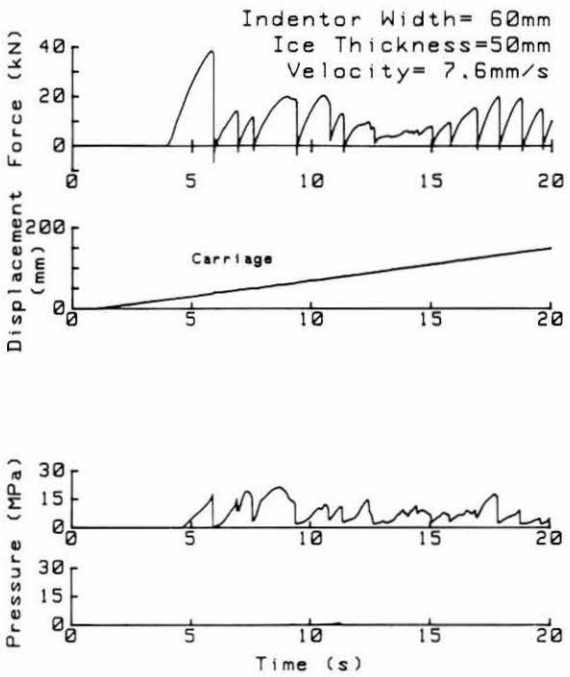

Figure A1. Test NSC 89.

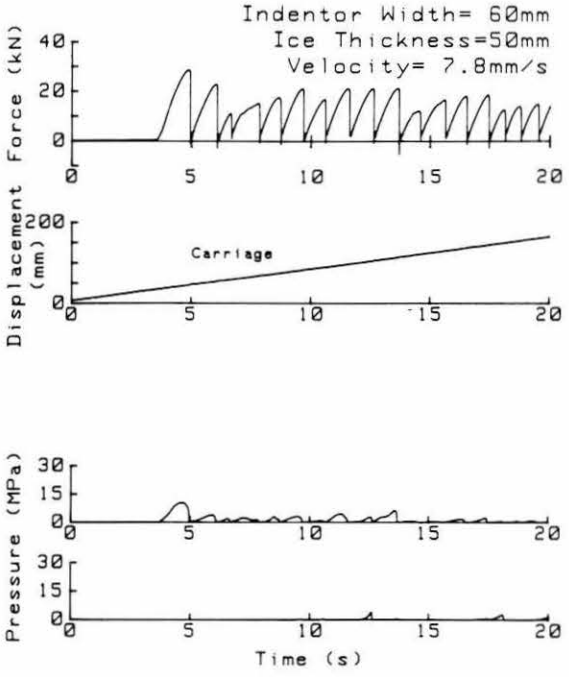

Figure A2. Test NSC 88.

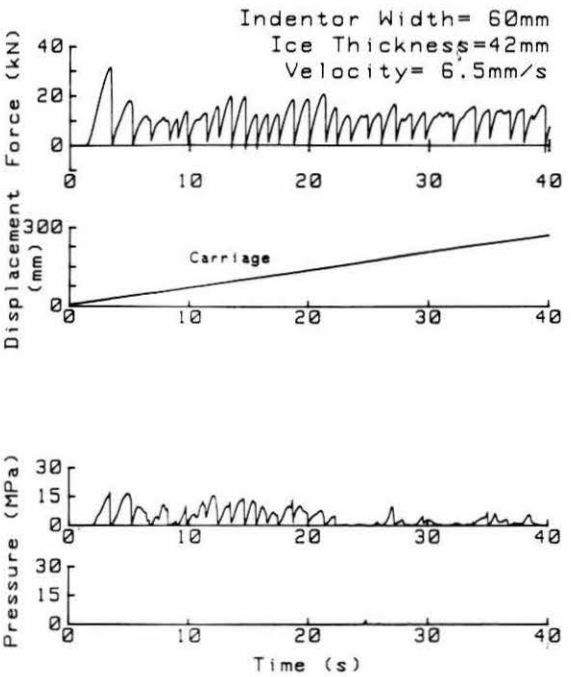

Figure A3. Test NSC 87.

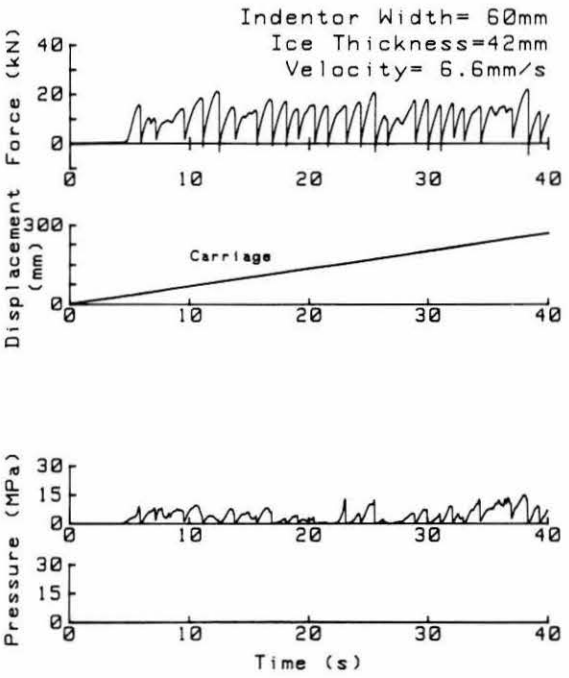

Figure A4. Test NSC 86.

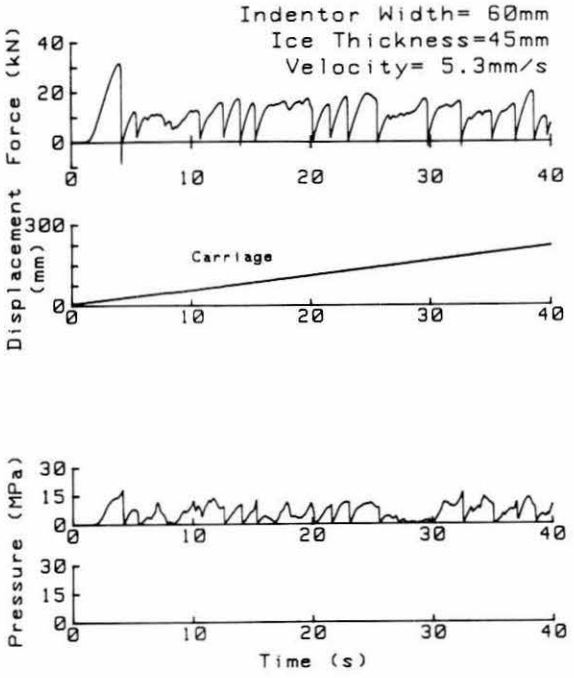

Figure A5. Test NSC 85.

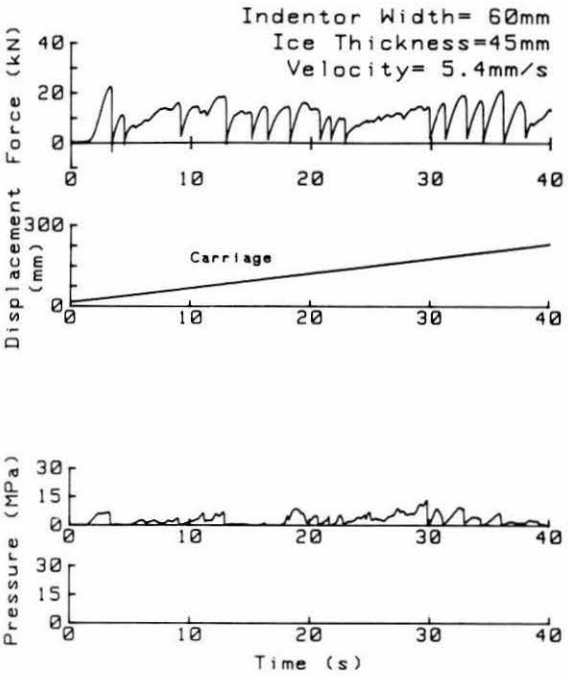

Figure A6. Test NSC 84.

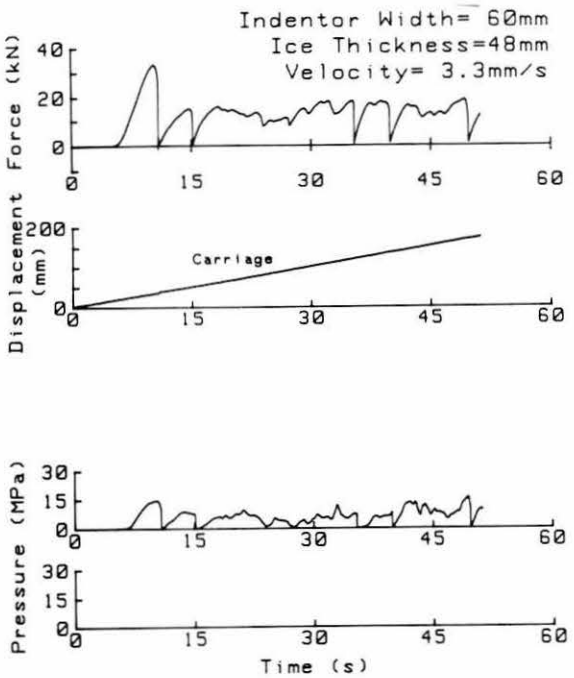

Figure A7. Test NSC 83.

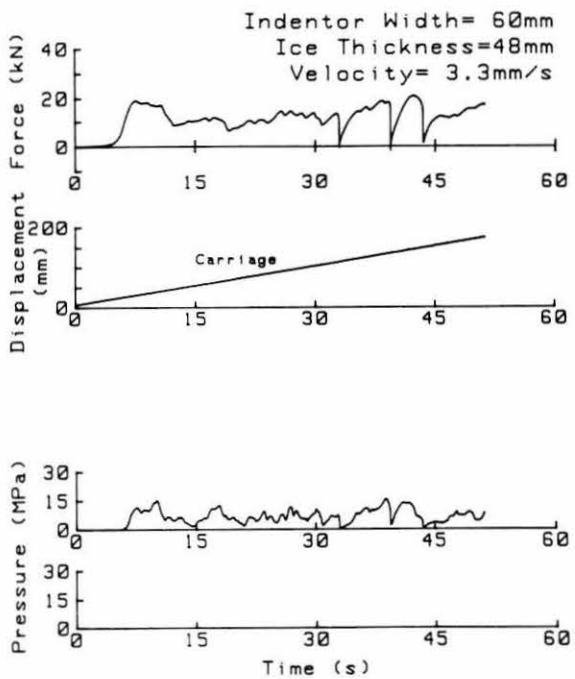

Figure A8. Test NSC 82.

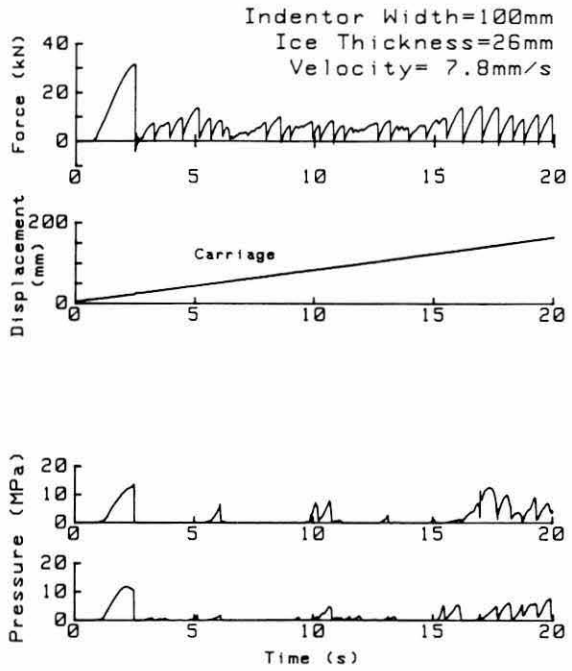

Figure A9. Test NSC 79.

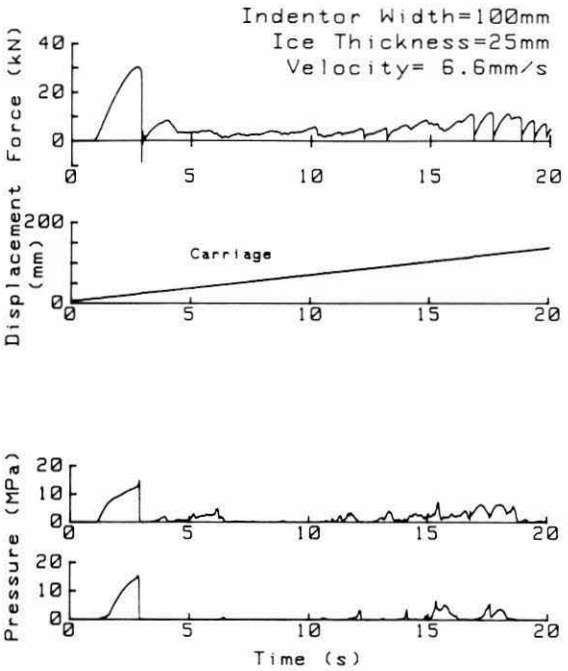

Figure A10. Test NSC 78.

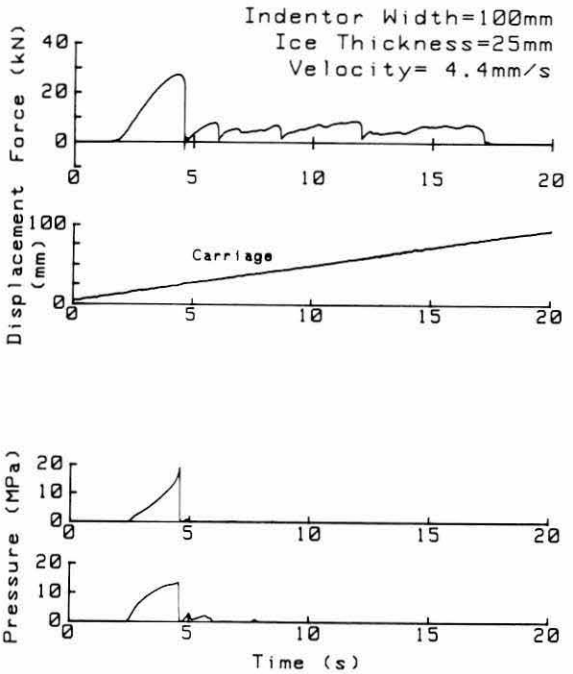

Figure A11. Test NSC 77.

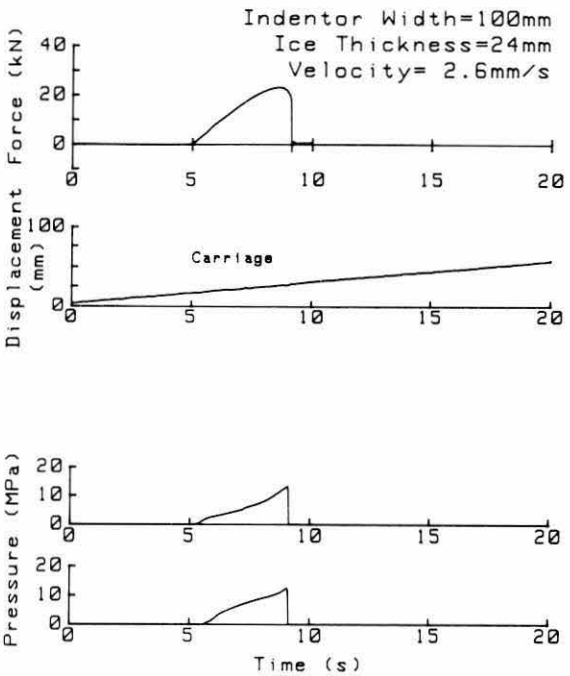

Figure A12. Test NSC 76.

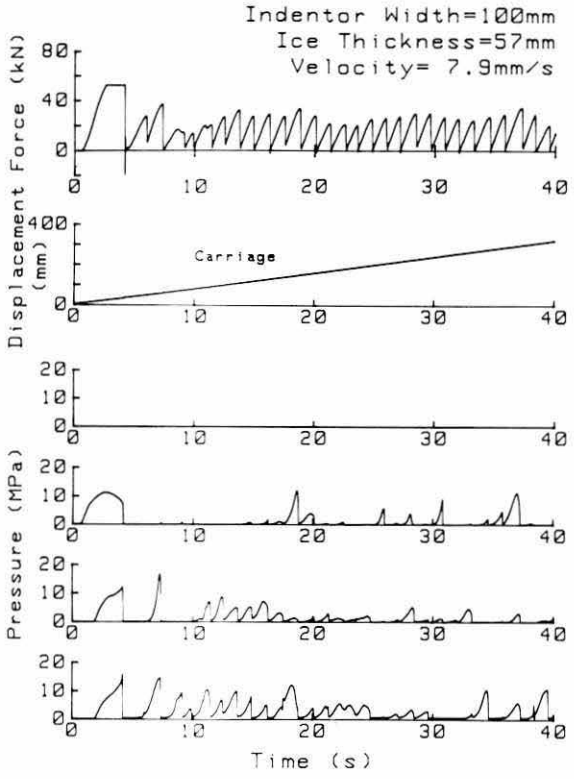

Figure A13. Test NSC 69.

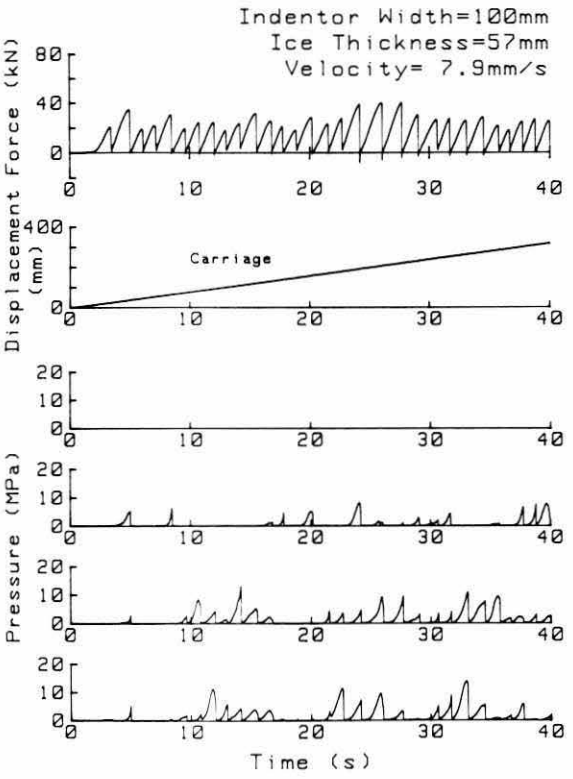

Figure A14. Test NSC 68.

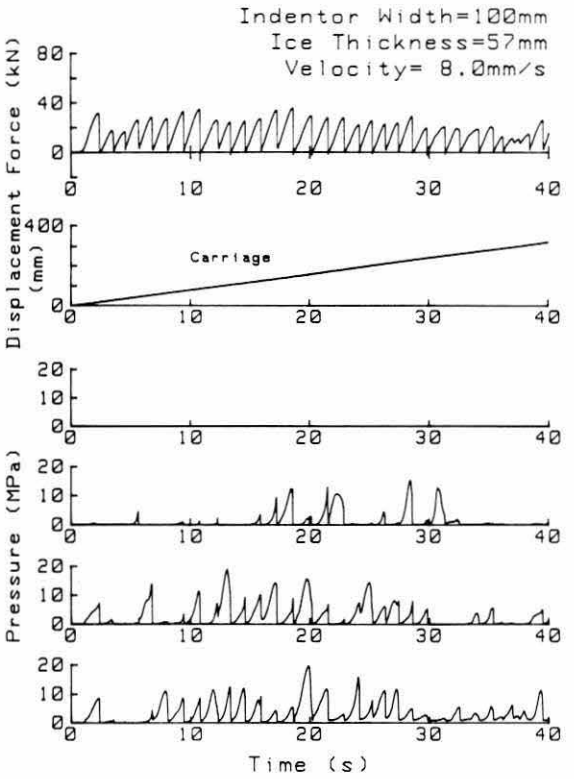

Figure A15. Test NSC 67.

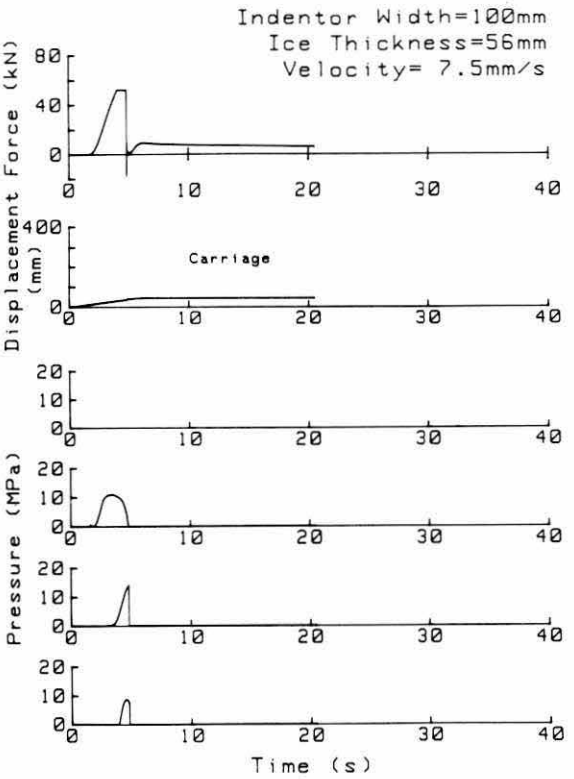

Figure A16. Test NSC 66.

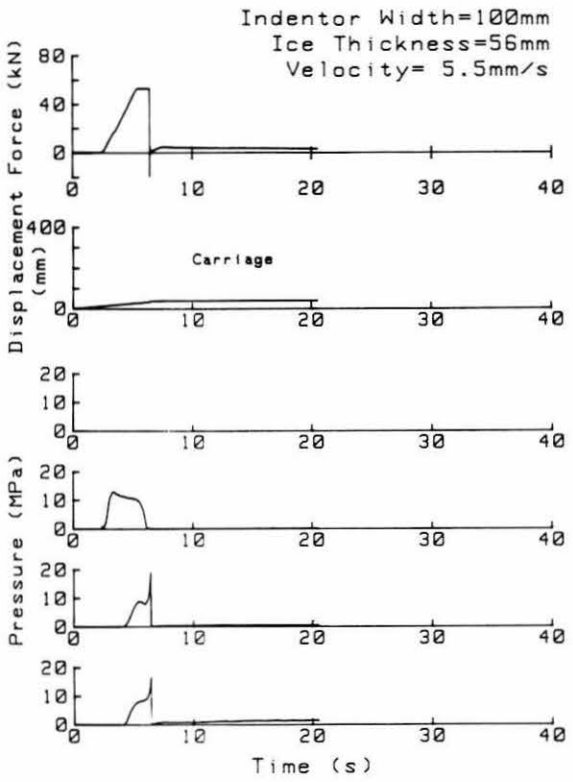

Figure A17. Test NSC 65.

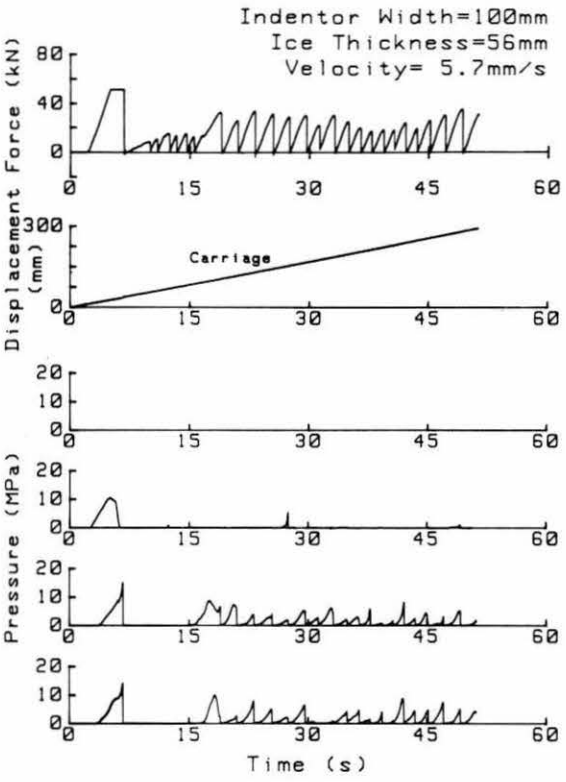

Figure A18. Test NSC 64.

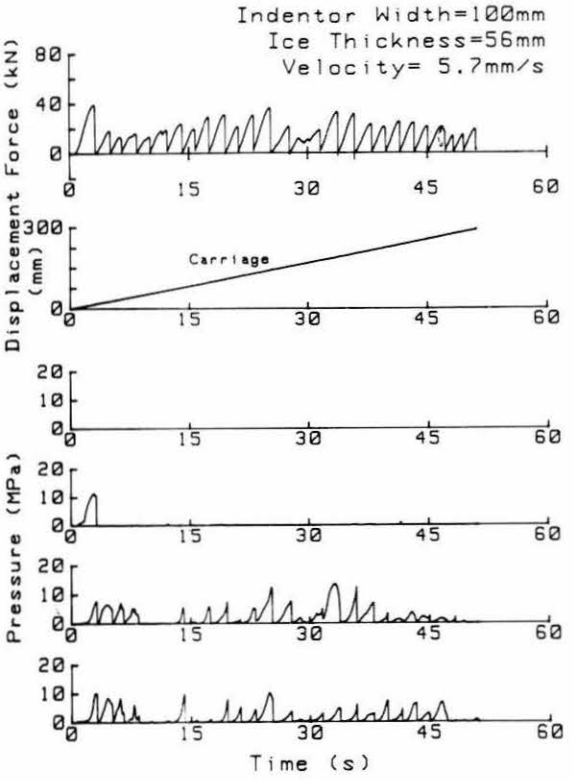

Figure A19. Test NSC 63.

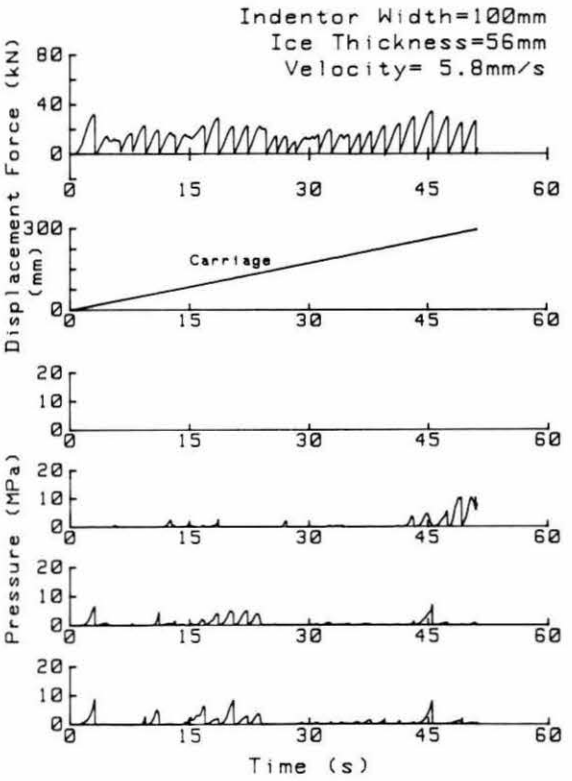

Figure A20. Test NSC 62.

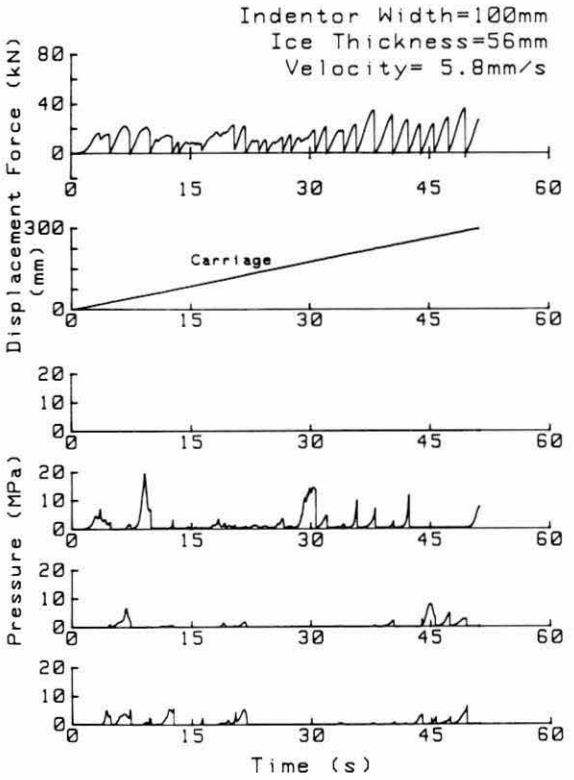

Figure A21. Test NSC 61.

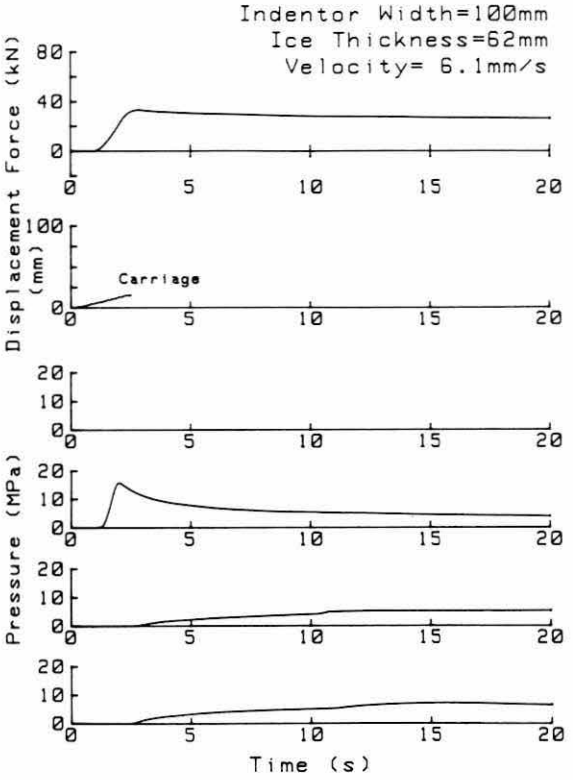

Figure A22. Test NSC 60.

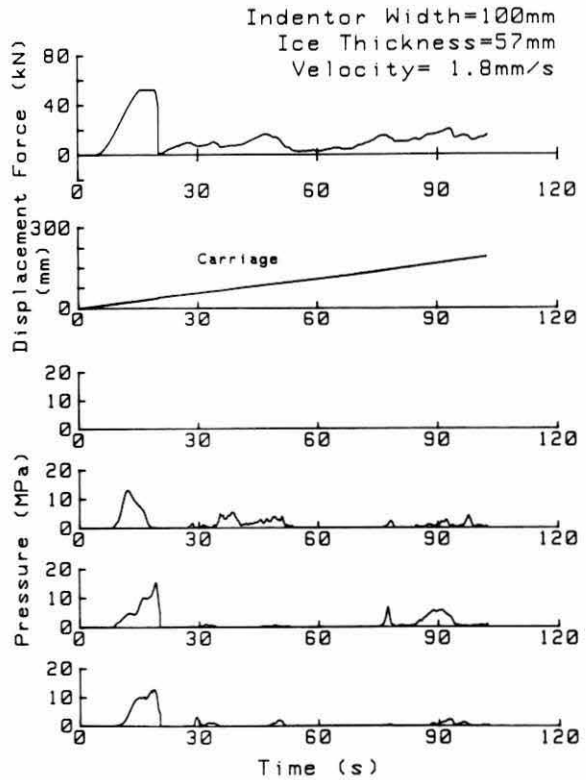

Figure A23. Test NSC 59.

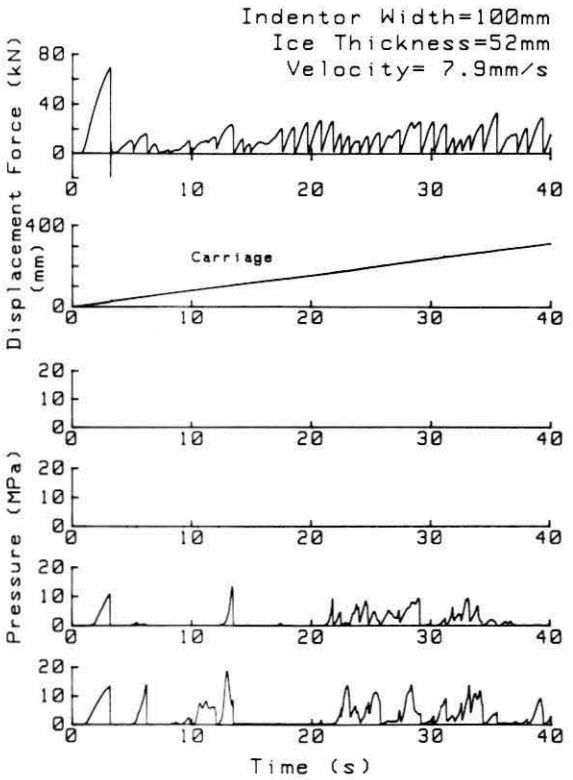

Figure A24. Test NSC 49.

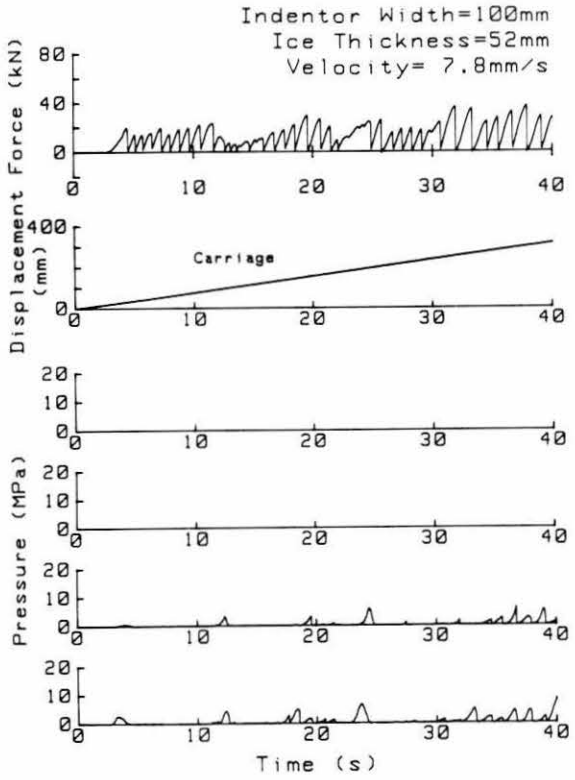

Figure A25. Test NSC 48.

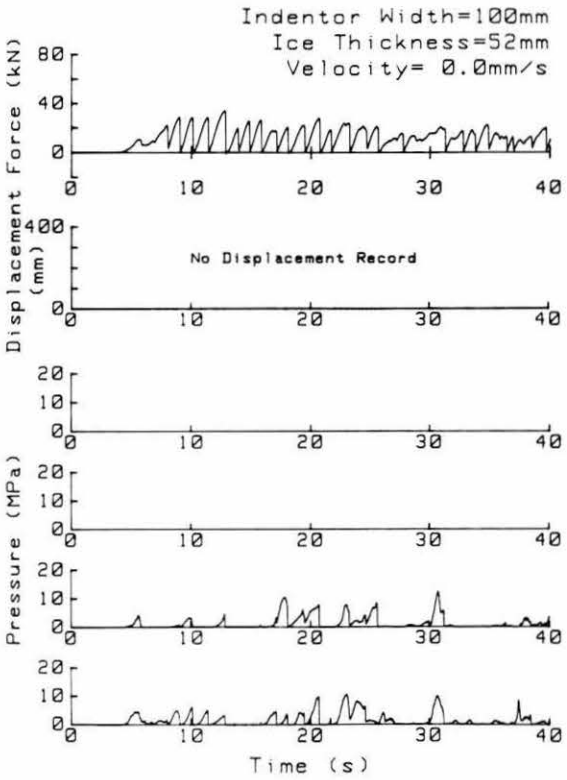

Figure A26. Test NSC 47.

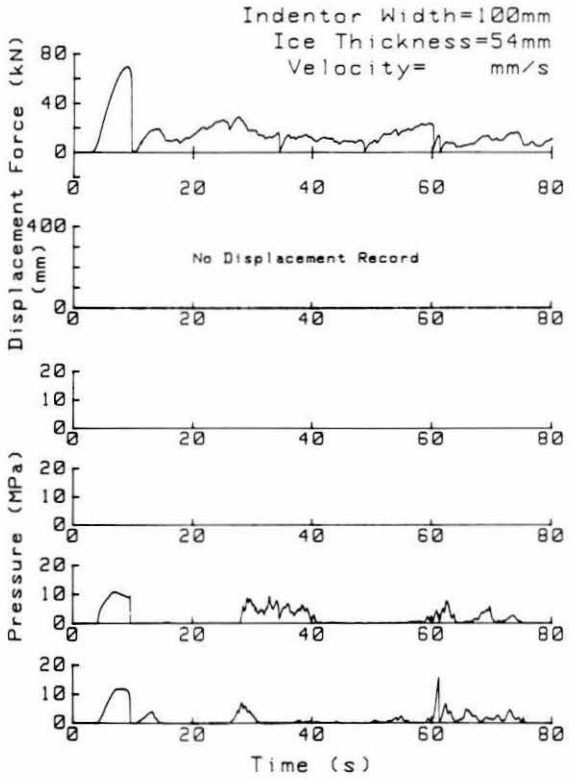

Figure A27. Test NSC 46.

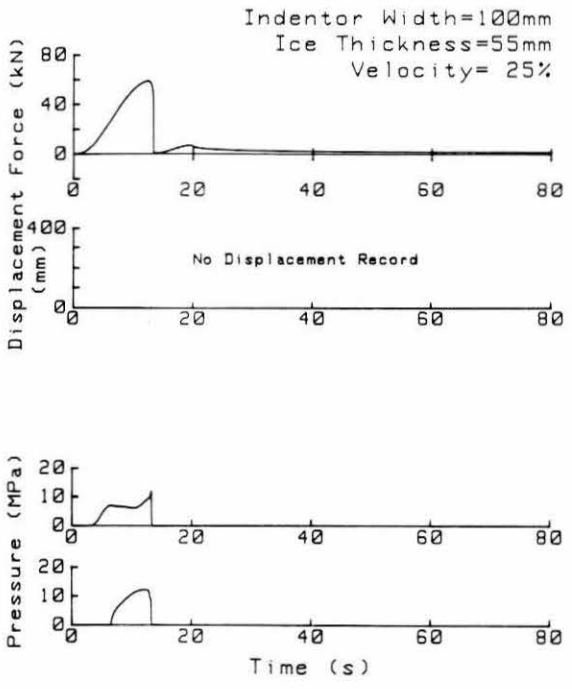

Figure A28. Test NSC 45.

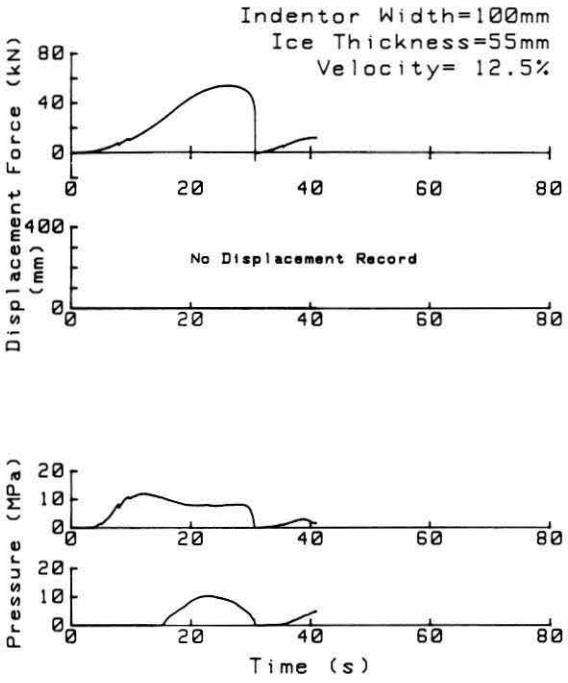

Figure A29. Test NSC 44.

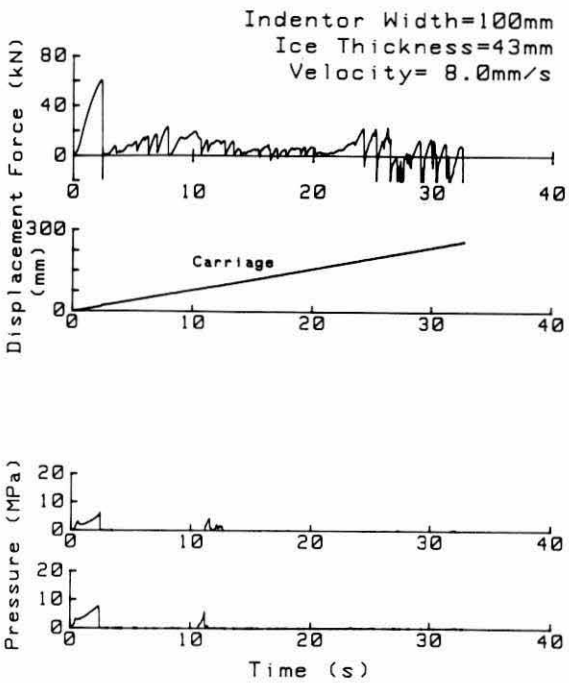

Figure A30. Test NSC 39.

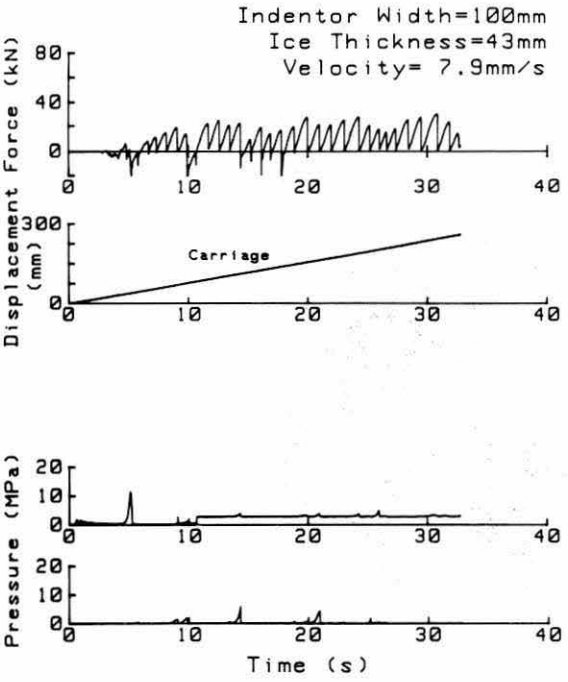

Figure A31. Test NSC 38.

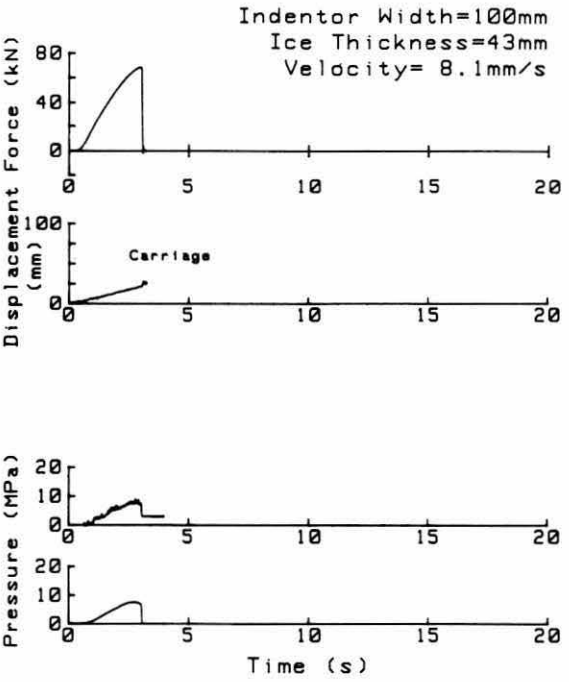

Figure A32. Test NSC 37.

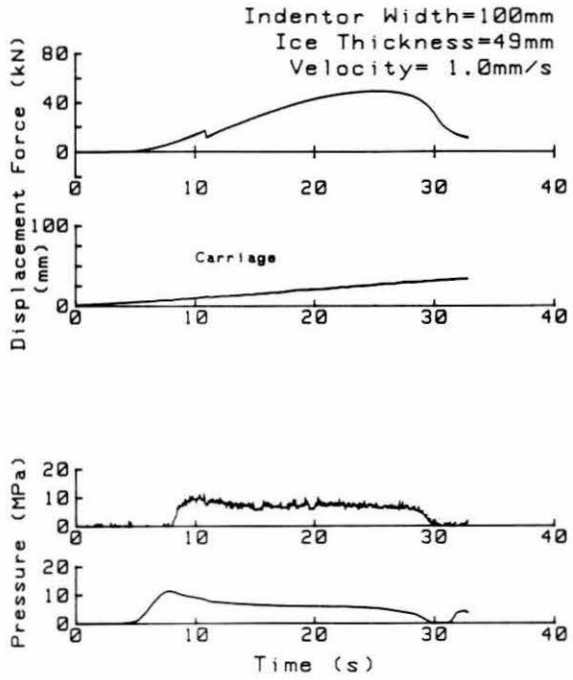

Figure A33. Test NSC 36.

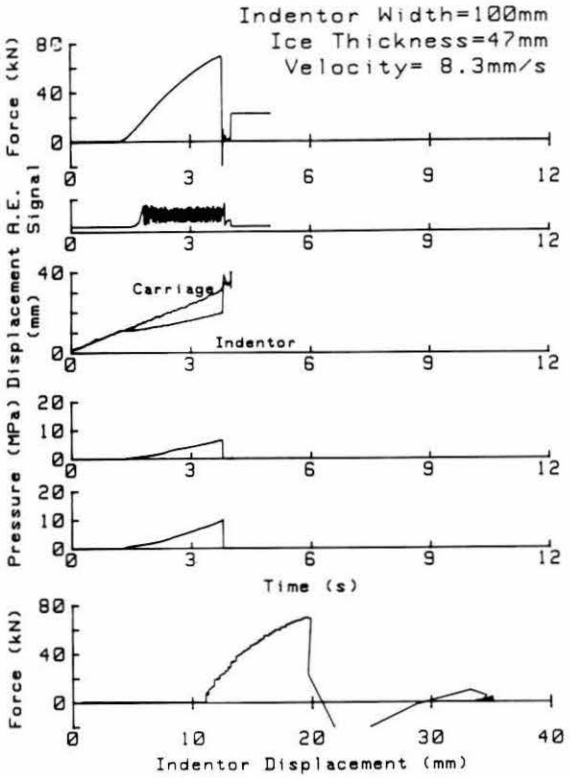

Figure A34. Test NSC 29.

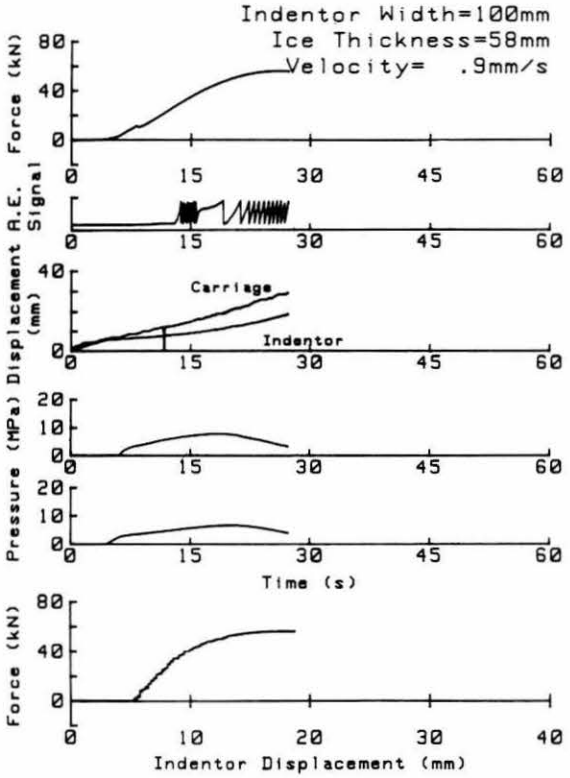

Figure A35. Test NSC 28.

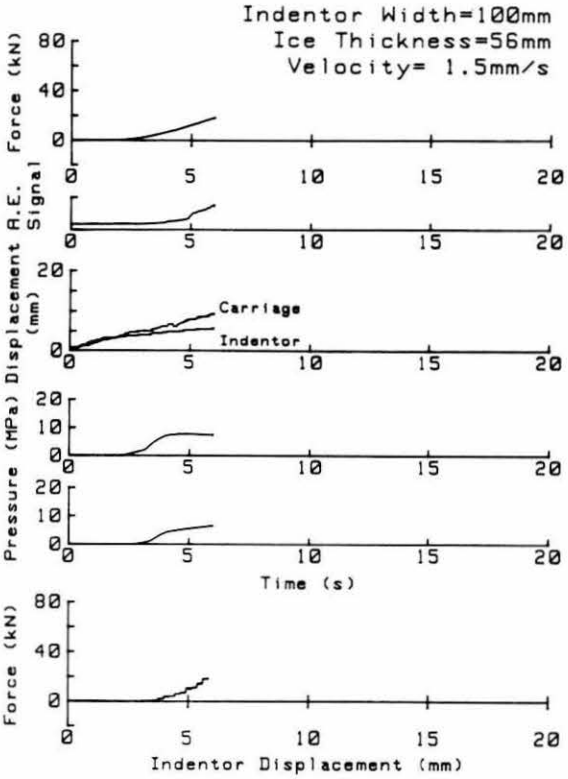

Figure A36. Test NSC 27.

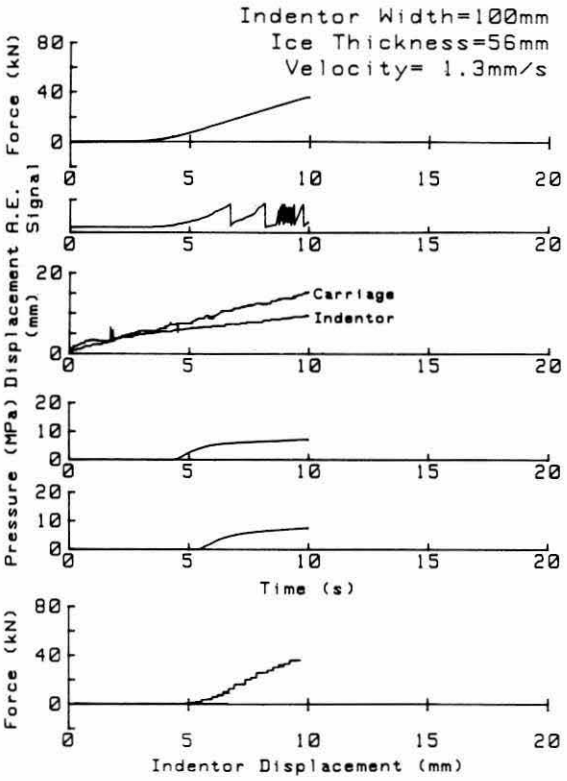

Figure A37. Test NSC 26.

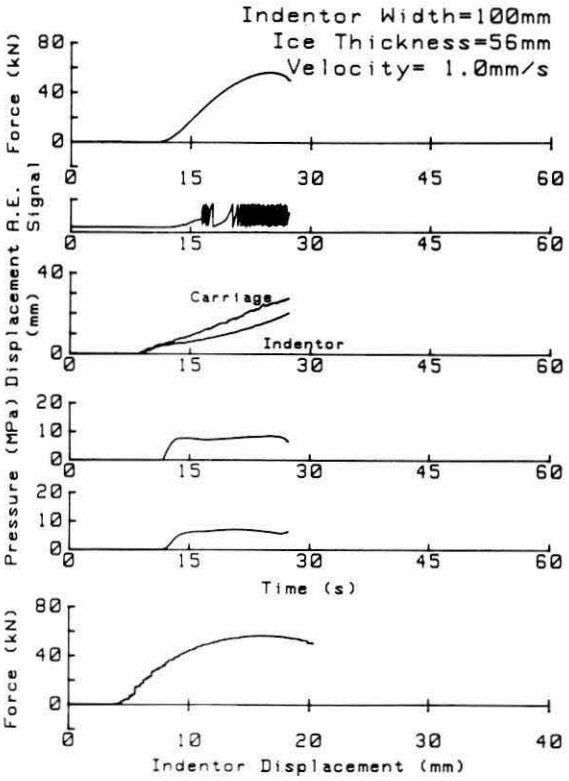

Figure A38. Test NSC 25.

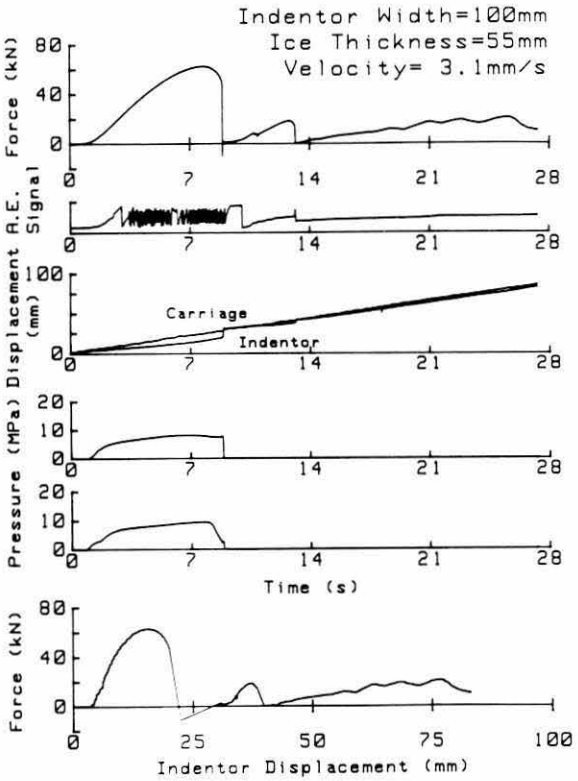

Figure A39. Test NSC 24.

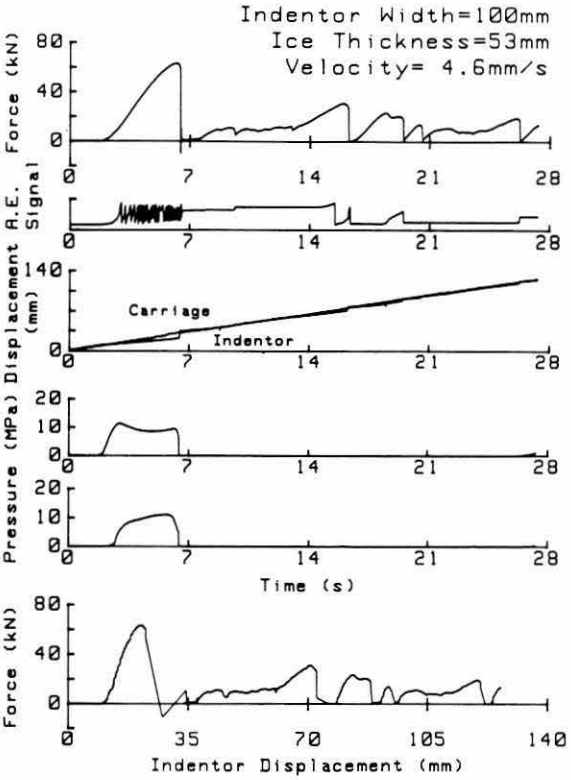

Figure A40. Test NSC 23.

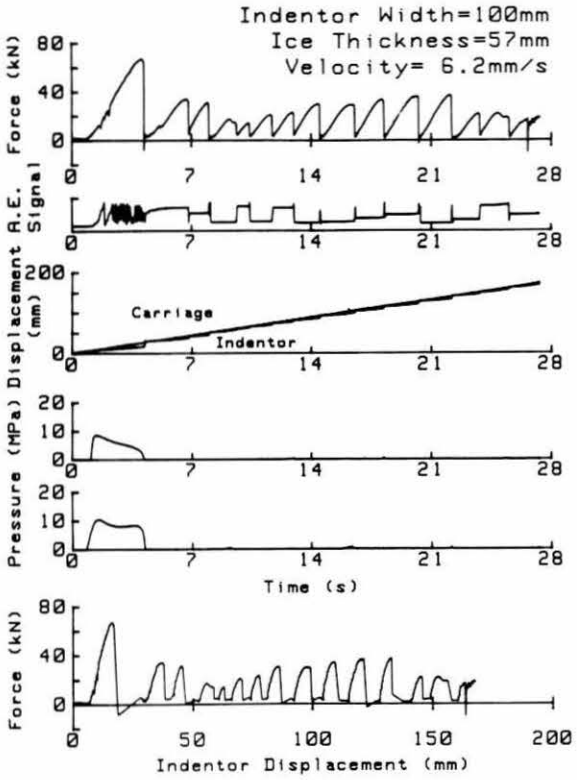

Figure A41. Test NSC 22.

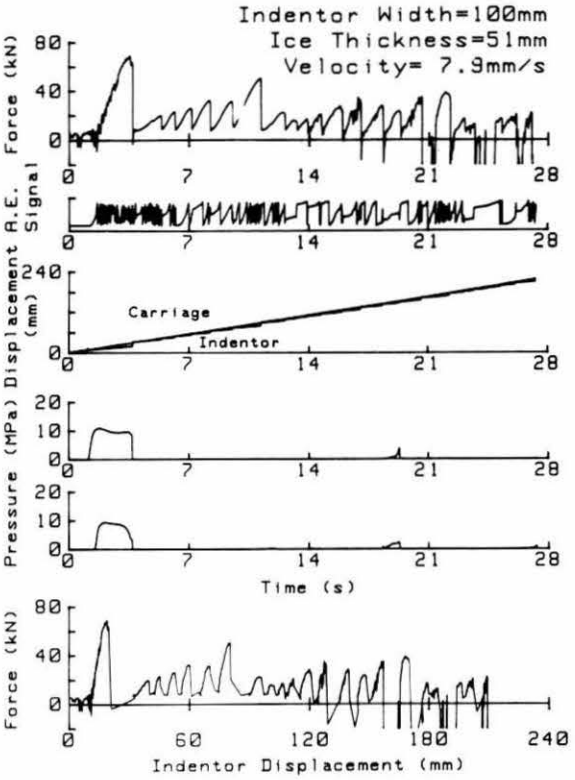

Figure A42. Test NSC 21.

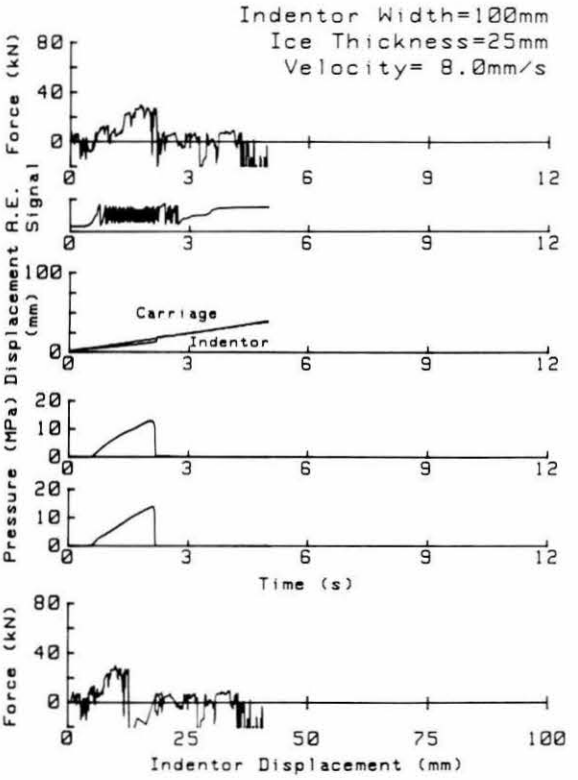

Figure A43. Test NSC 19.

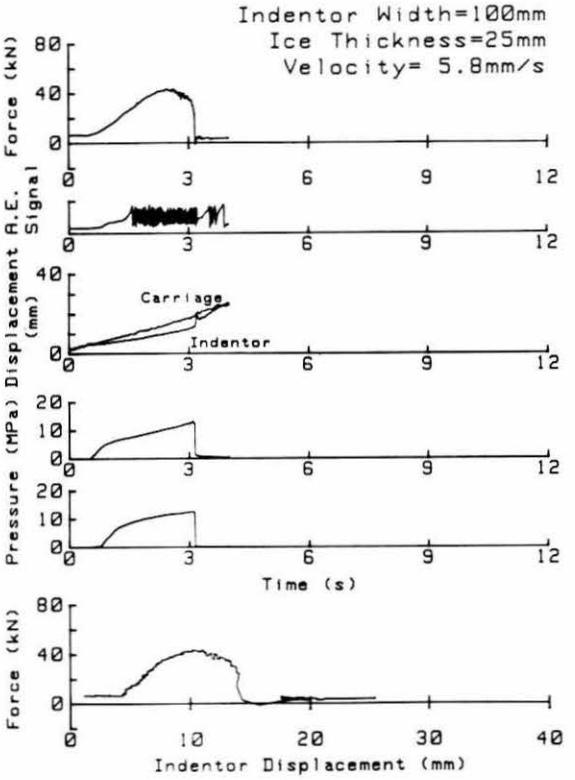

Figure A44. Test NSC 18.

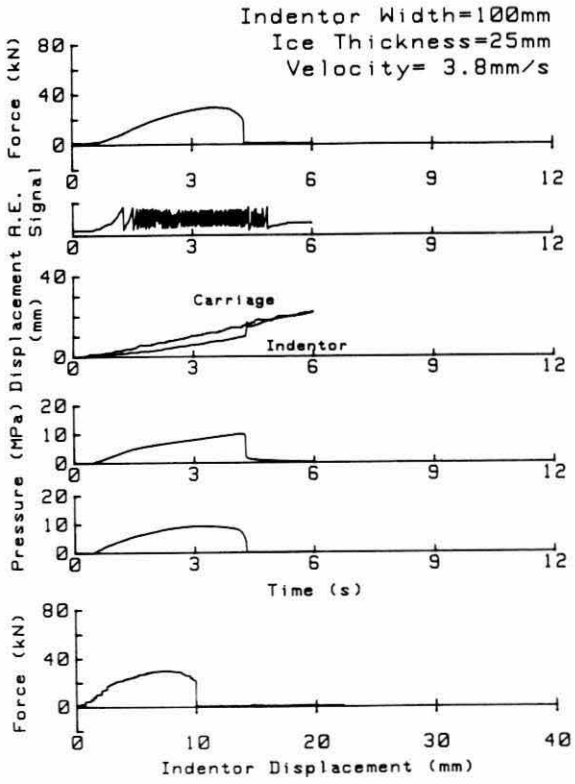

Figure A45. Test NSC 17.

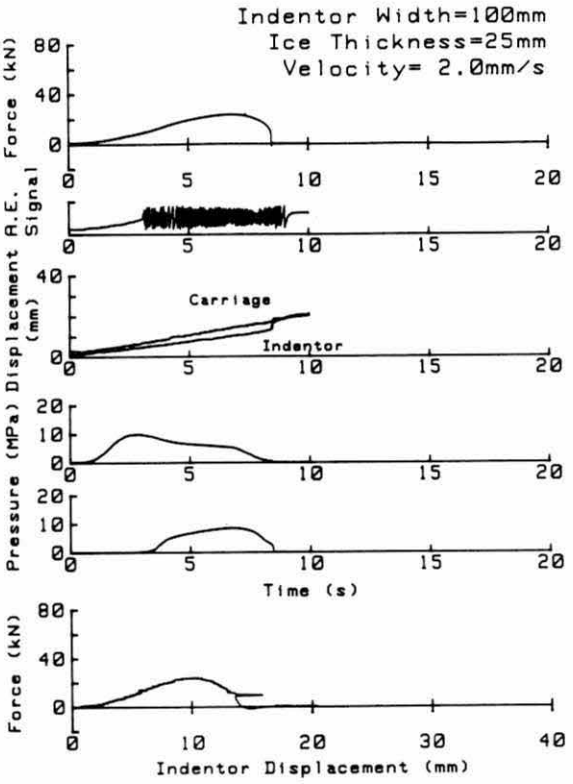

Figure A46. Test NSC 16.

N N test sheets

Each data sheet contains the following four plots: ice force versus time, AE signal versus time, ice force versus indentor displacement and calculated positions of the resultant force within the contact area. These are plotted with a label *x* for the total force exceeding the following threshold values: 5 kN in tests 31 to 39, 15 kN in tests 41 to 49, 61 to 70 and 701, 10 kN in tests 51 to 60, 20 kN in tests 71 to 76, and 40 kN in test 81.

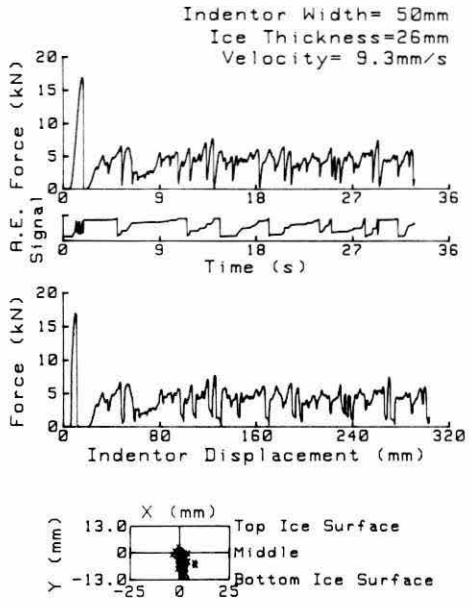

Figure A47. Test N N 31.

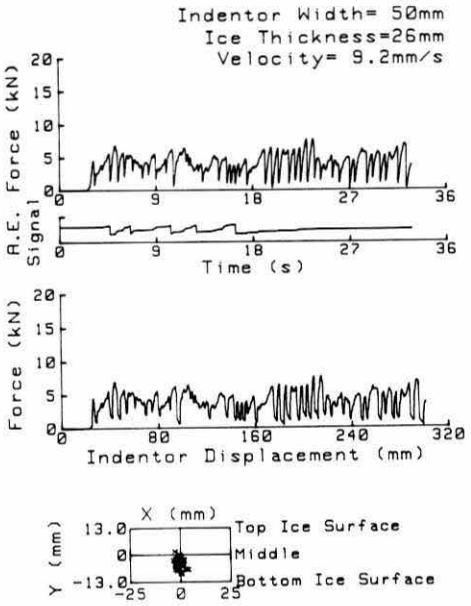

Figure A48. Test N N 32.

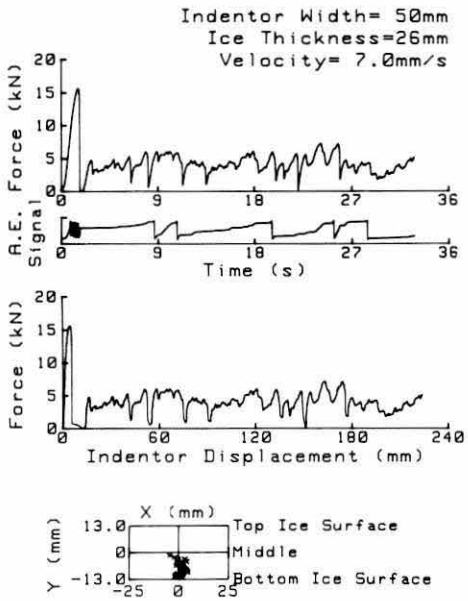

Figure A49. Test N N 33.

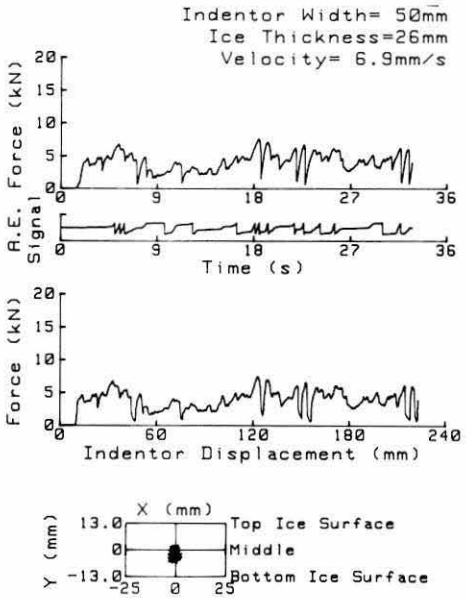

Figure A50. Test N N 34.

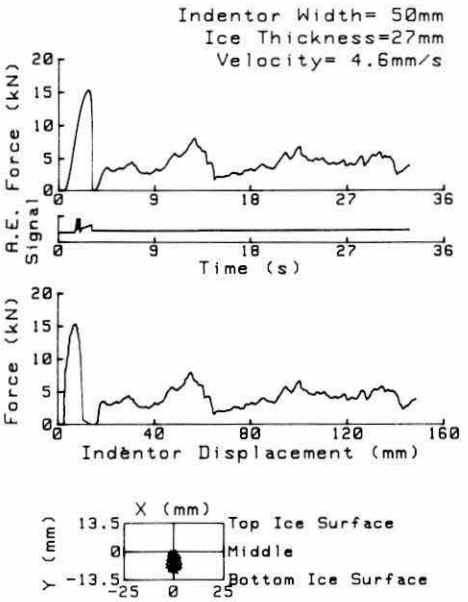

Figure A51. Test N N 35.

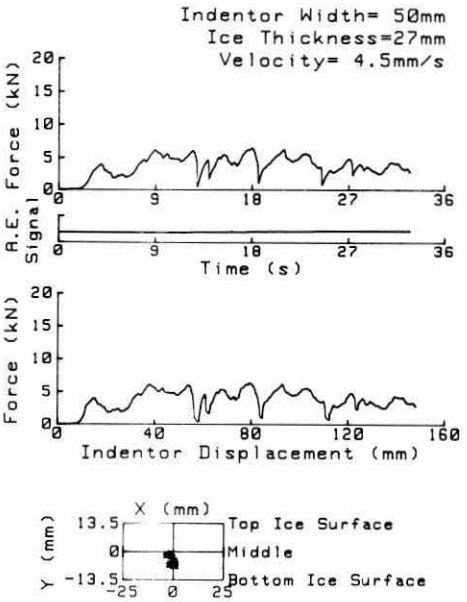

Figure A52. Test N N 36.

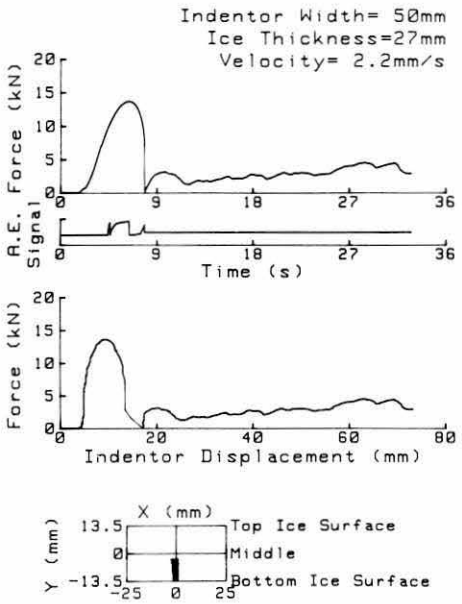

Figure A53. Test N N 37.

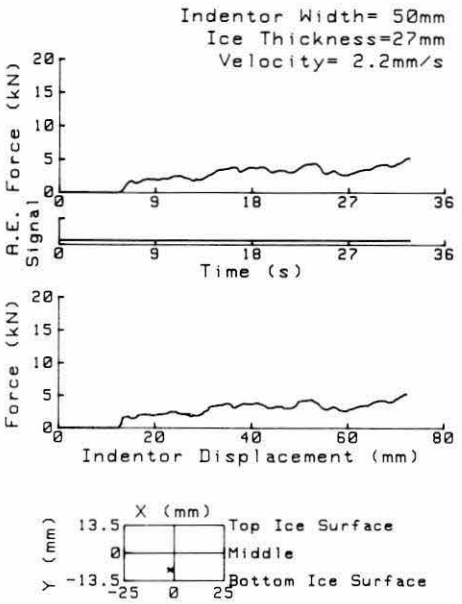

Figure A54. Test N N 38.

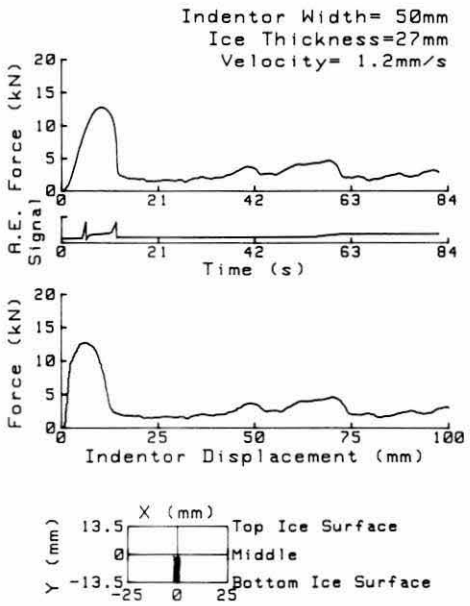

Figure A55. Test N N 39.

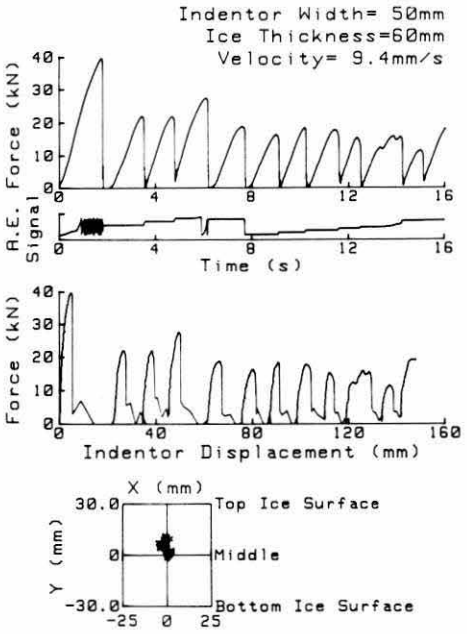

Figure A56. Test N N 41.

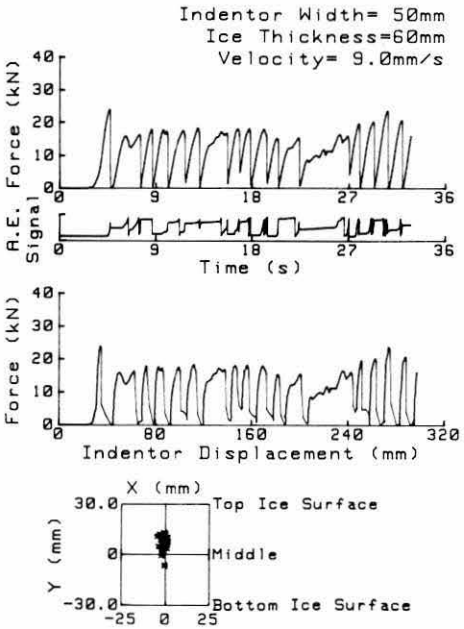

Figure A57. Test N N 42.

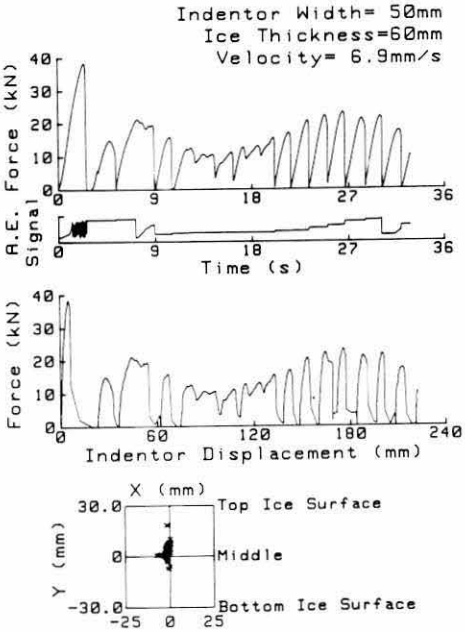

Figure A58. Test N N 43.

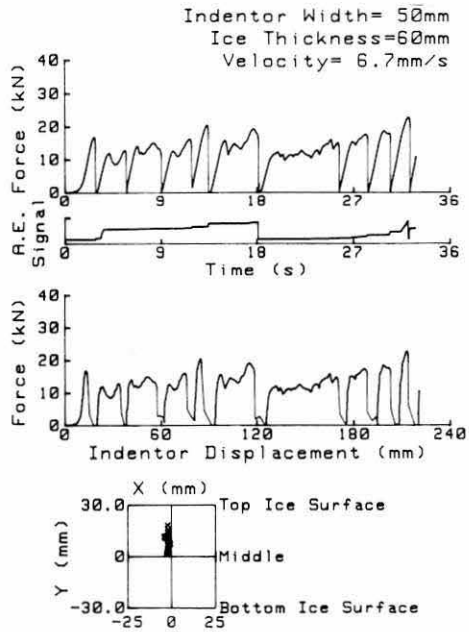

Figure A59. Test N N 44.

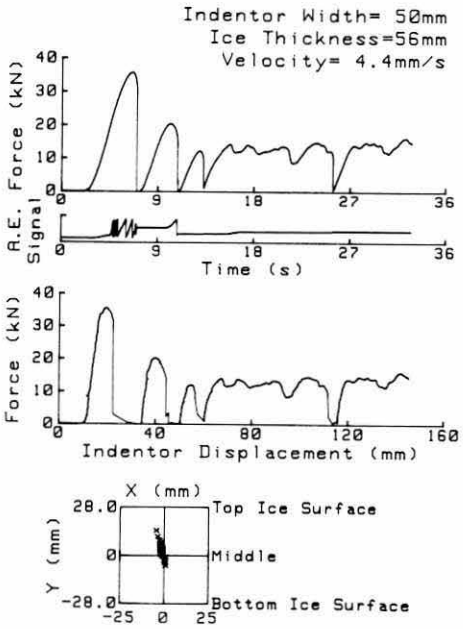

Figure A60. Test N N 45.

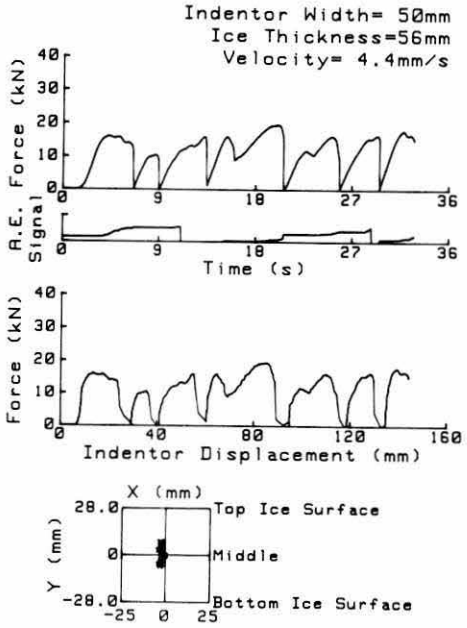

Figure A61. Test N N 46.

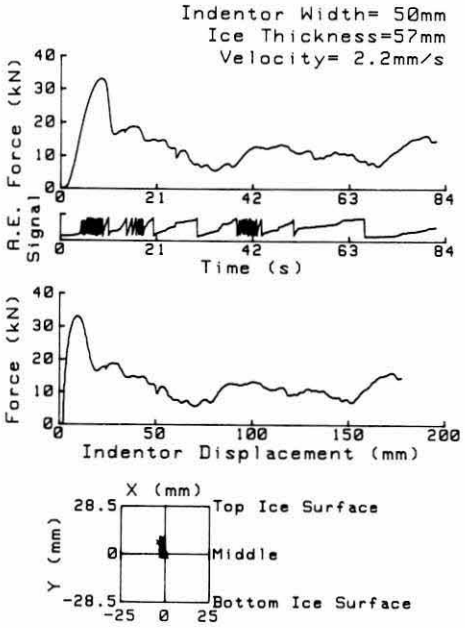

Figure A62. Test N N 47.

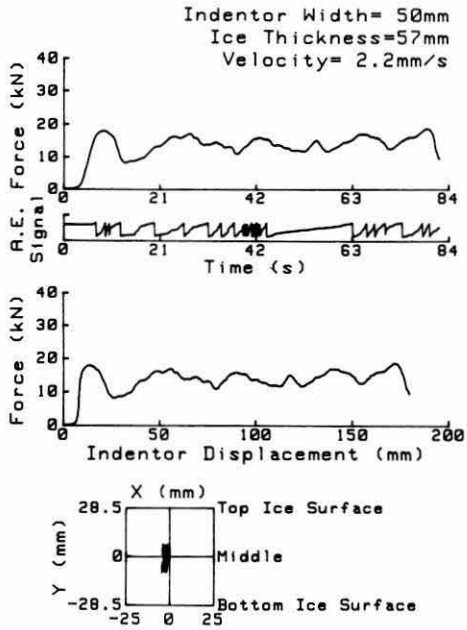

Figure A63. Test N N 48.

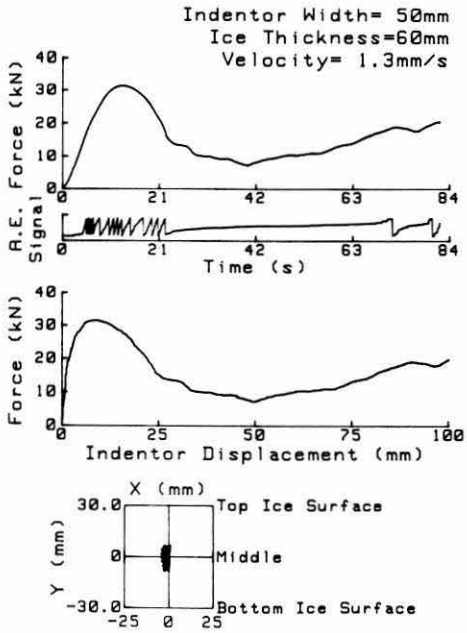

Figure A64. Test N N 49.

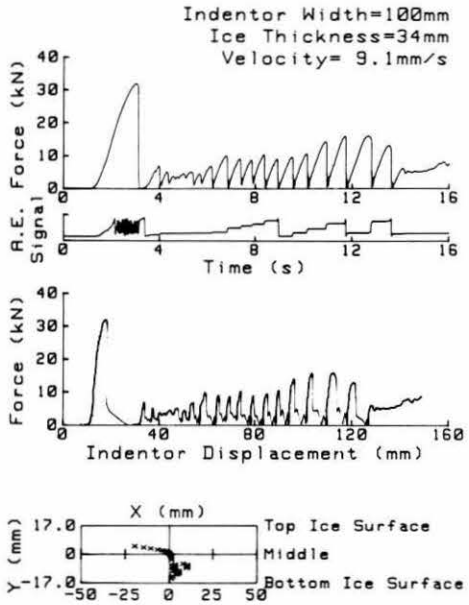

Figure A65. Test N N 51.

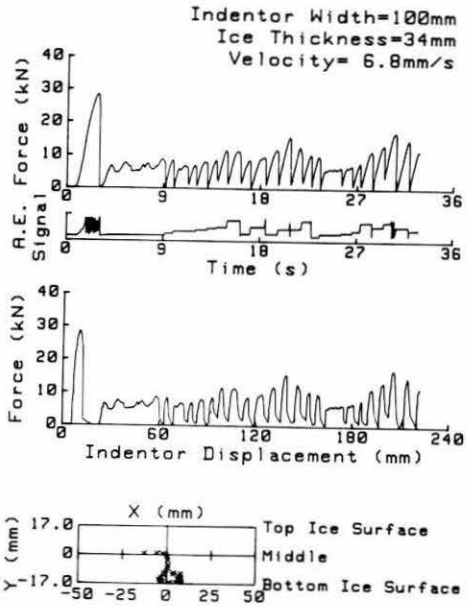

Figure A66. Test N N 52.

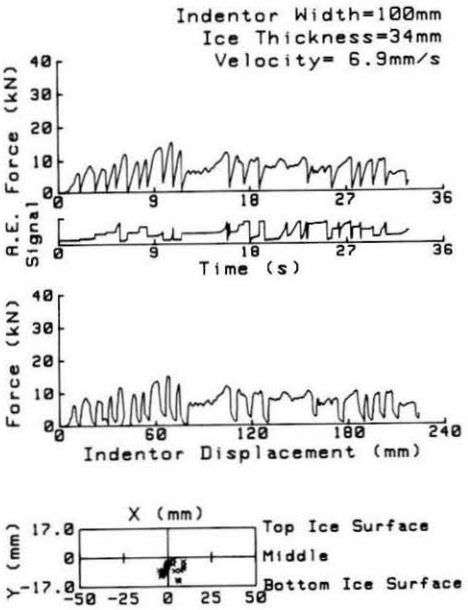

Figure A67. Test N N 53.

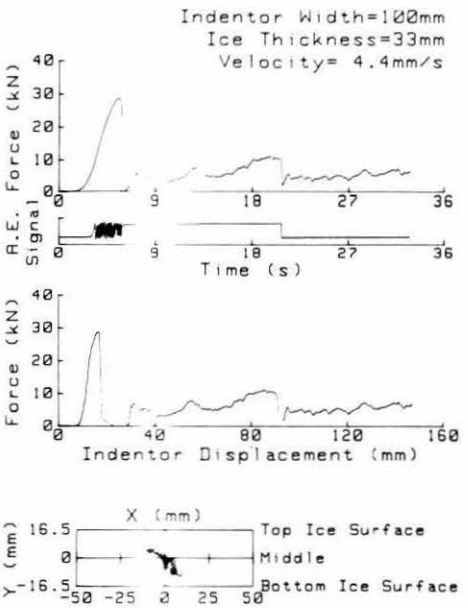

Figure A68. Test N N 55.

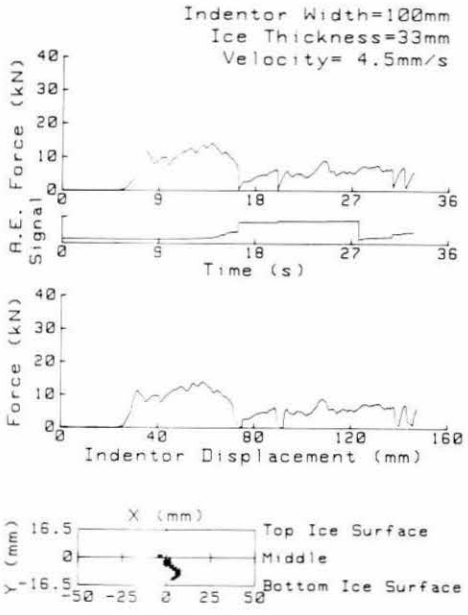

Figure A69. Test N N 56.

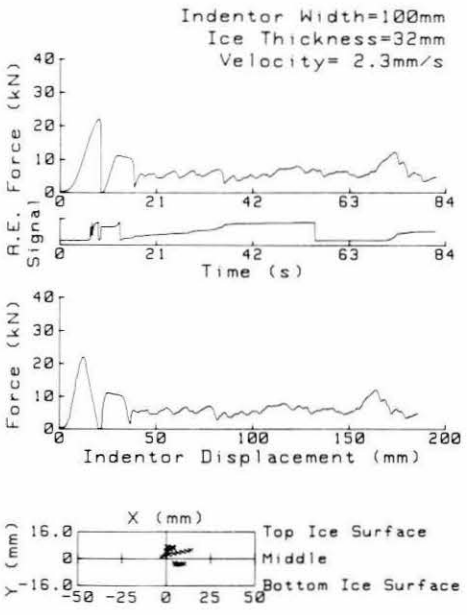

Figure A70. Test N N 57.

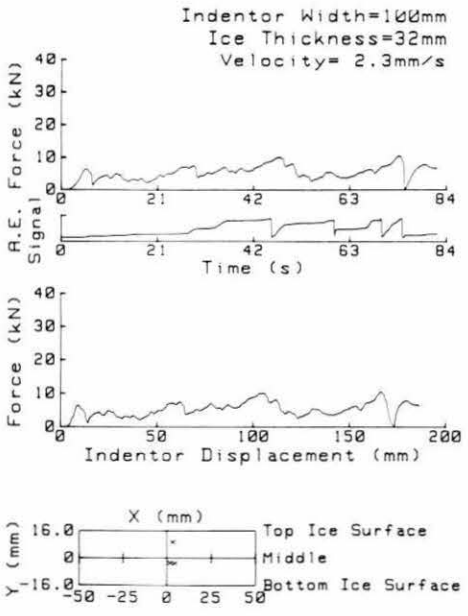

Figure A71. Test N N 58.

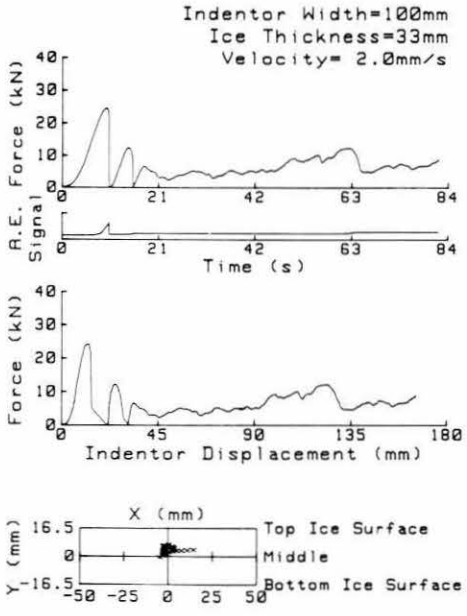

Figure A72. Test N N 59.

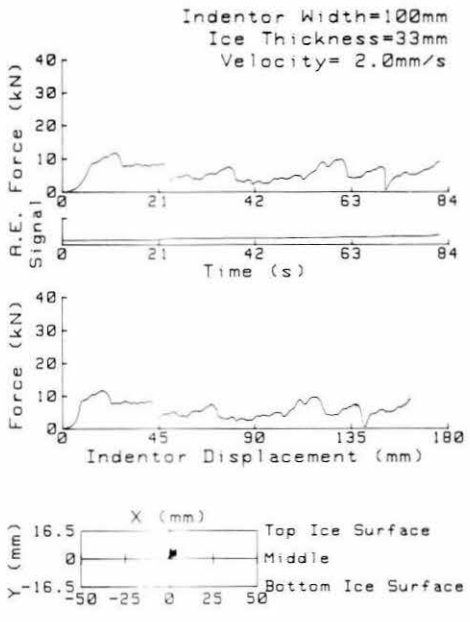

Figure A73. Test N N 60.

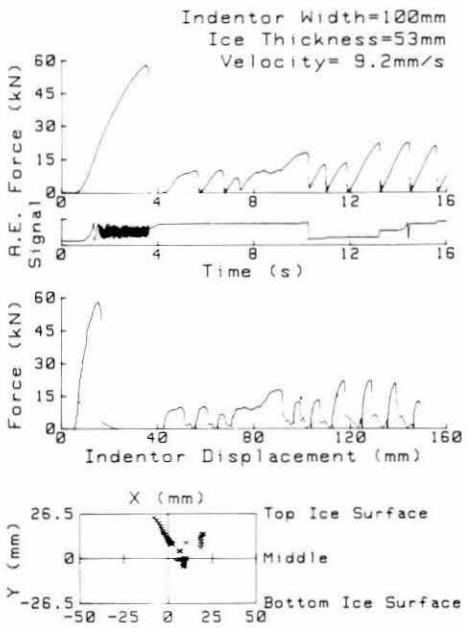

Figure A74. Test N N 61.

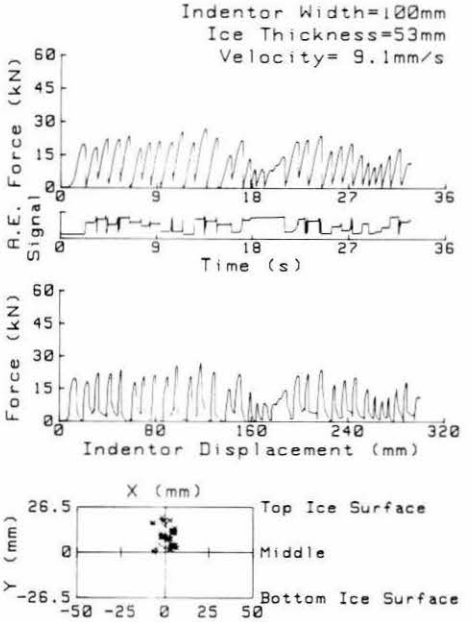

Figure A75. Test N N 62.

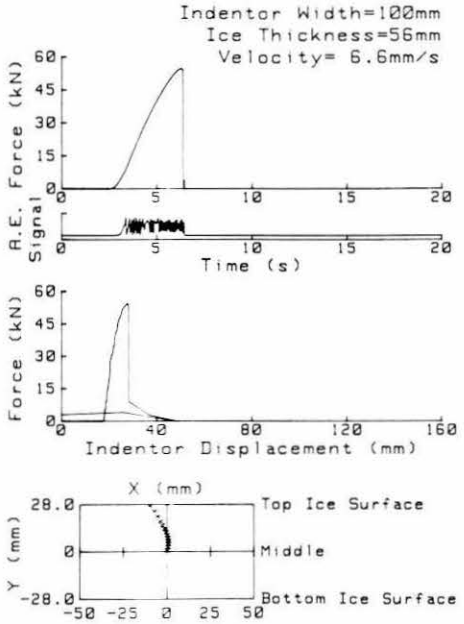

Figure A76. Test N N 63.

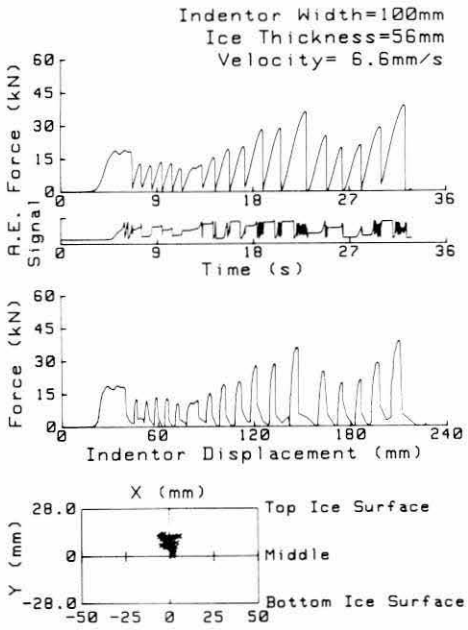

Figure A77. Test N N 64.

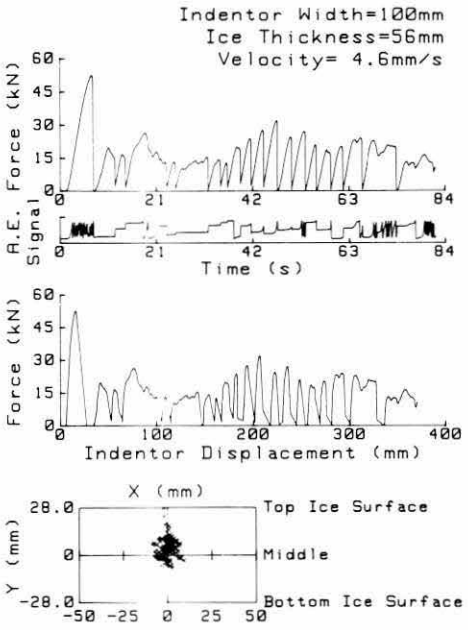

Figure A78. Test N N 65.

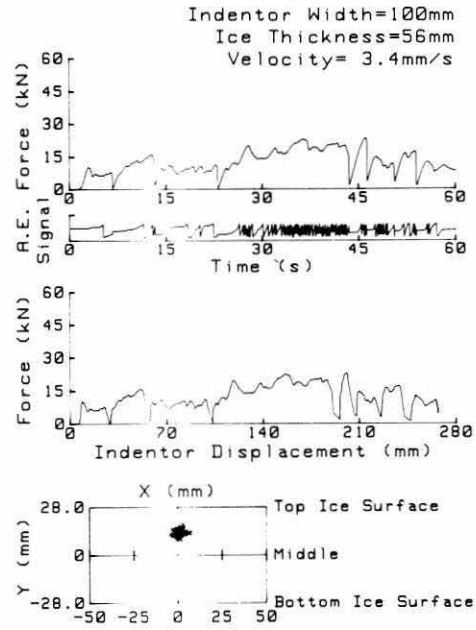

Figure A79. Test N N 66.

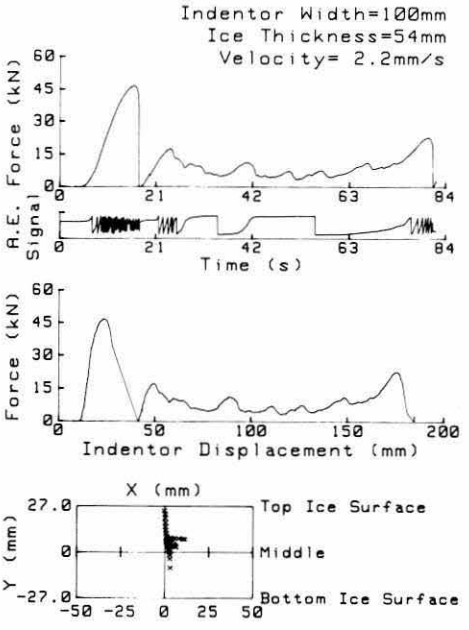

Figure A80. Test N N 67.

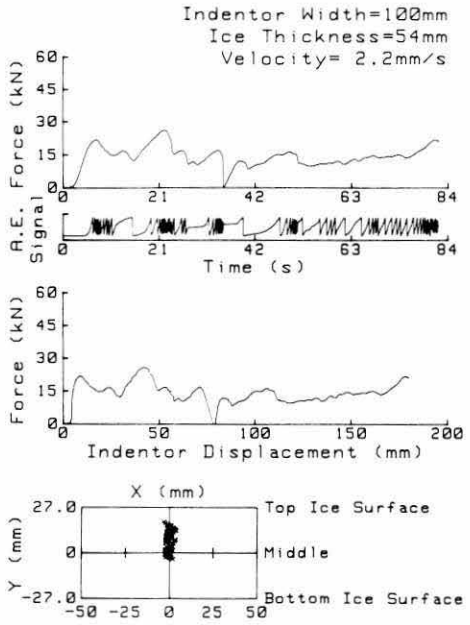

Figure A81. Test N N 68.

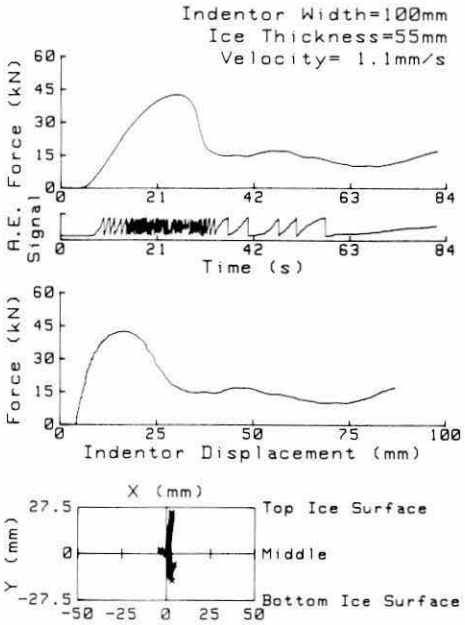

Figure A82. Test N N 69.

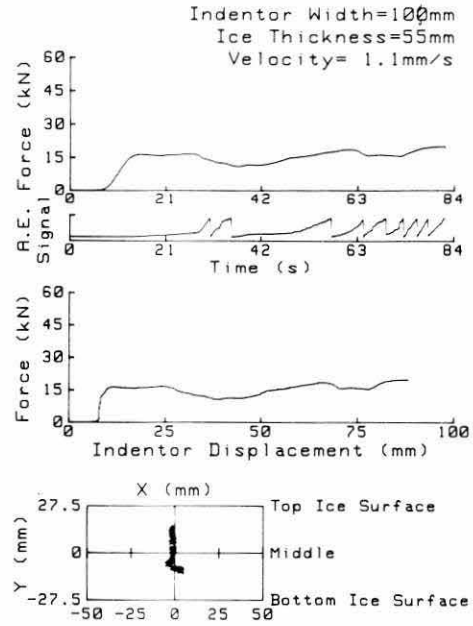

Figure A83. Test N N 70.

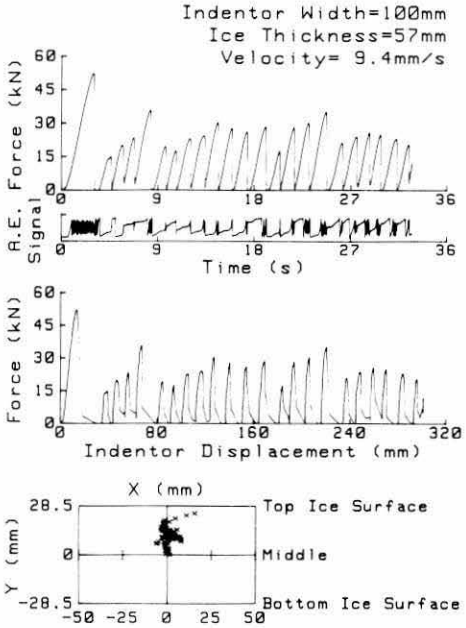

Figure A84. Test N N 701.

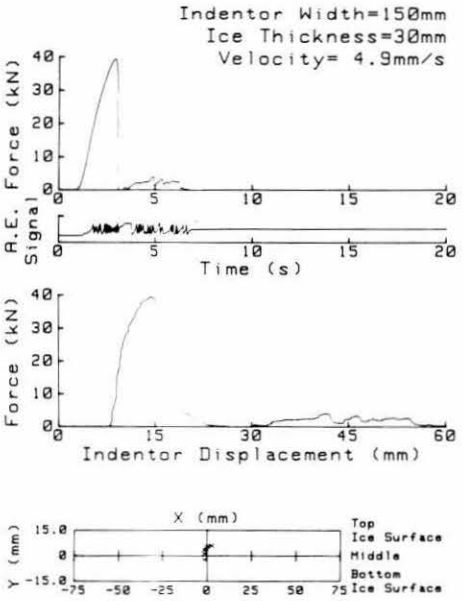

Figure A85. Test N N 71.

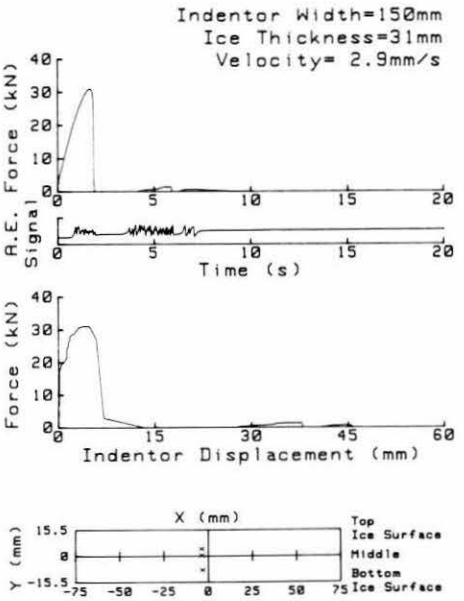

Figure A86. Test N N 72.

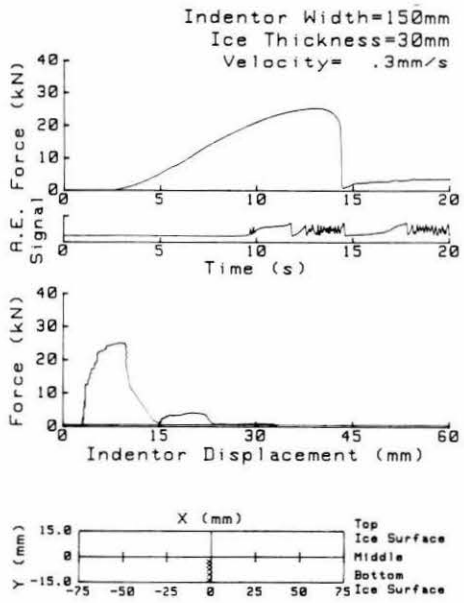

Figure A87. Test N N 73.

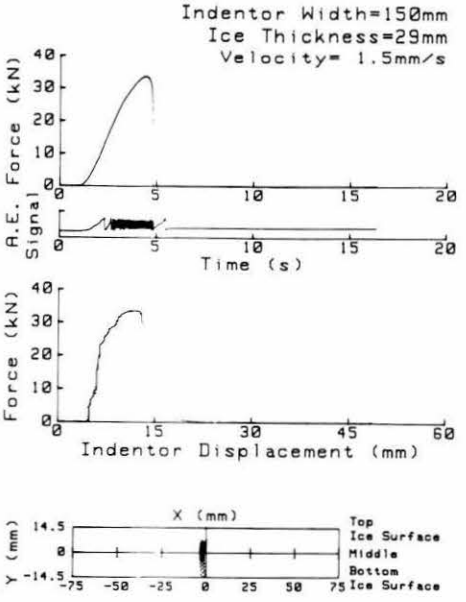

Figure A88. Test N N 74.

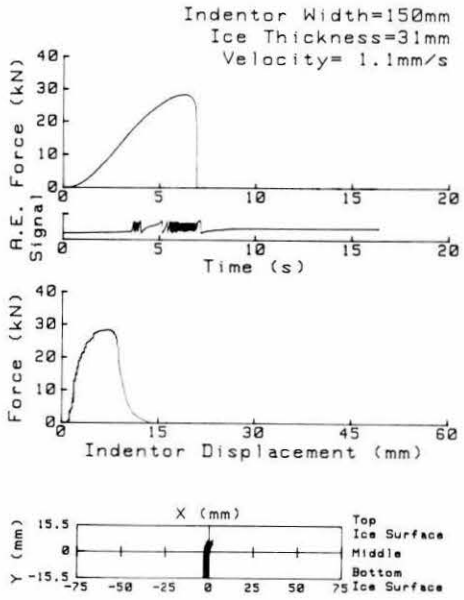

Figure A89. Test N N 75.

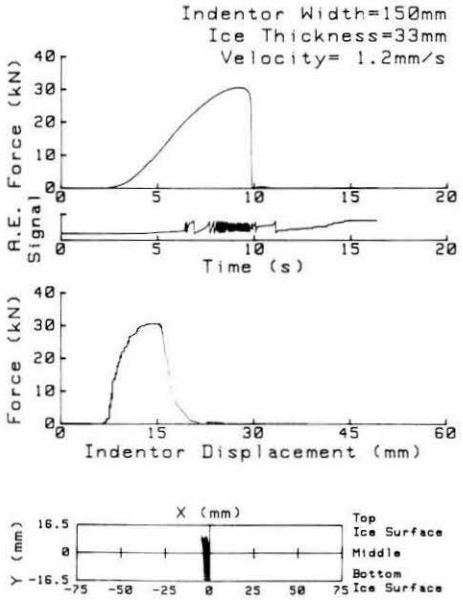

Figure A90. Test N N 76.

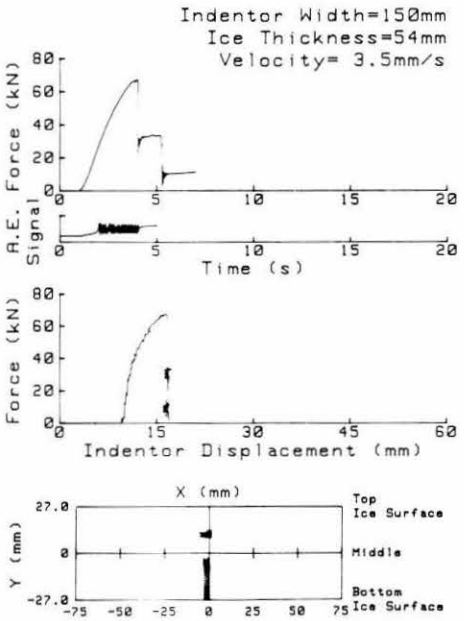

Figure A91. Test N N 81.

Energy plots of N N tests

Each data sheet contains the following plots: ice force versus time, carriage and indentor displacement versus time, energies supplied to the carriage, dissipated in the ice and stored in the structure versus time and rates of energy supplied to the carriage, dissipated in the ice and stored in the structure versus time.

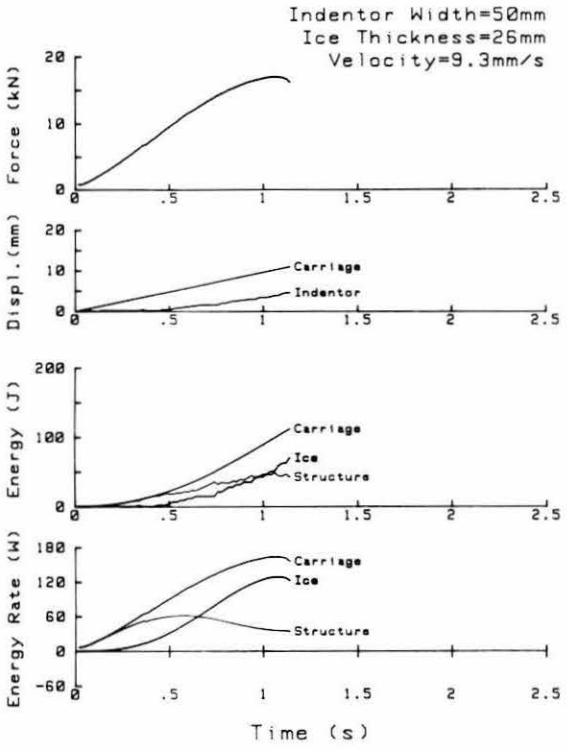

Figure A92. Test N N 31.

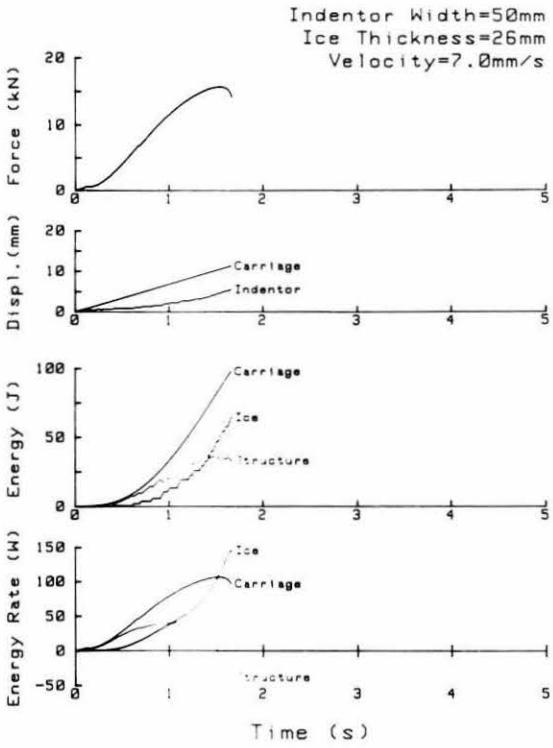

Figure A93. Test N N 33.

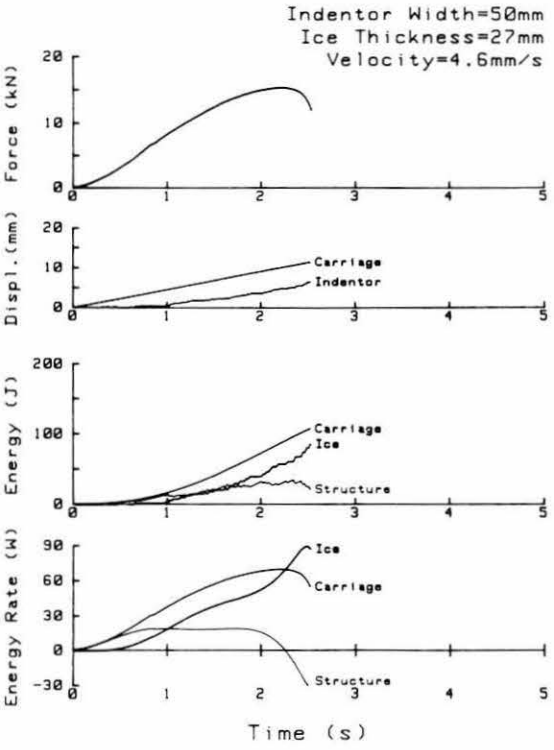

Figure A94. Test N N 35.

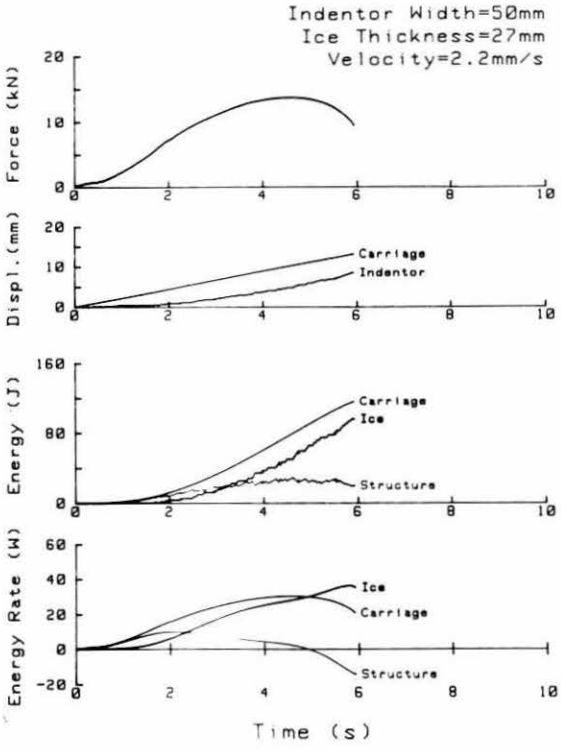

Figure A95. Test N N 37.

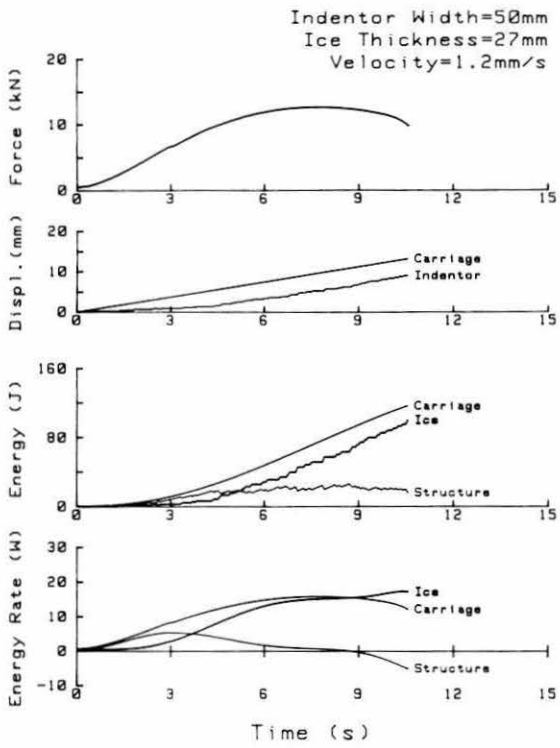

Figure A96. Test N N 39.

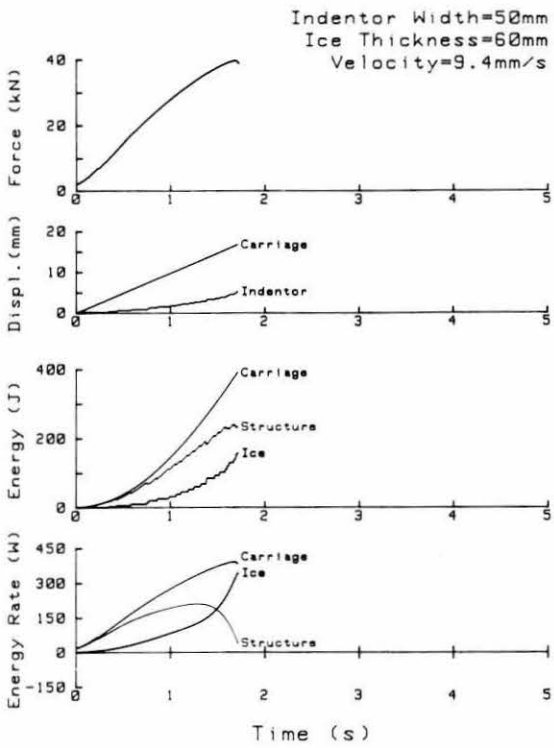

Figure A97. Test N N 41.

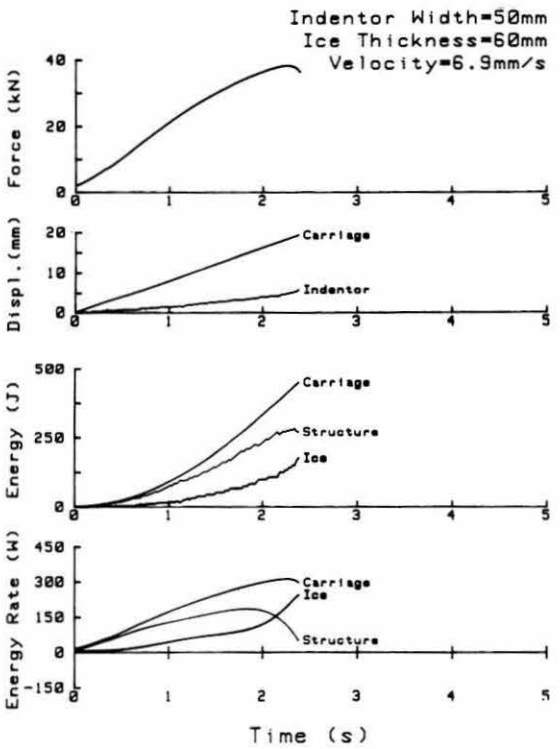

Figure A98. Test N N 43.

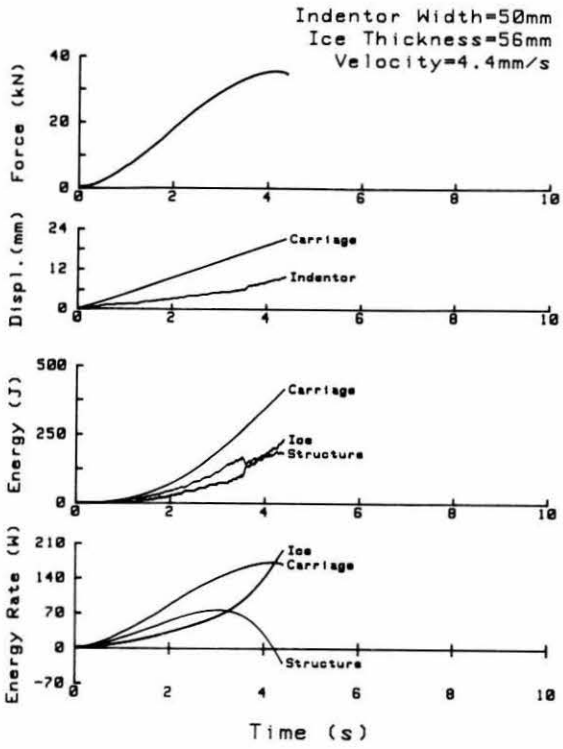

Figure A99. Test N N 45.

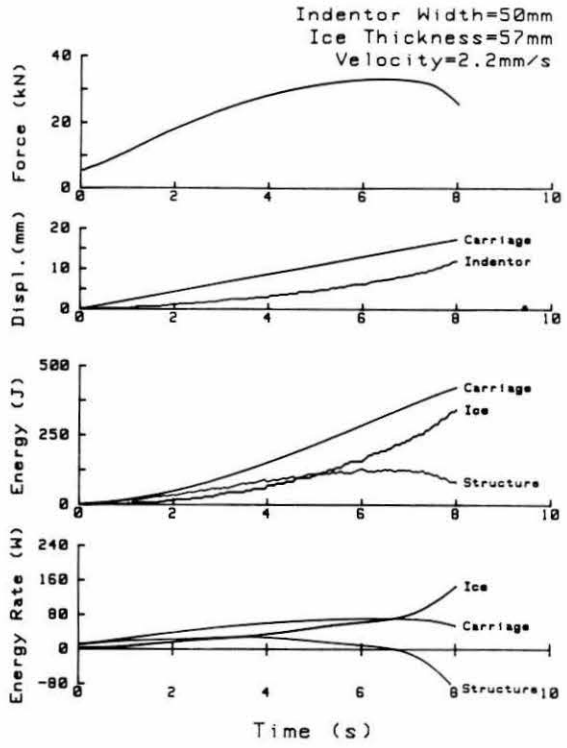

Figure A100. Test N N 47.

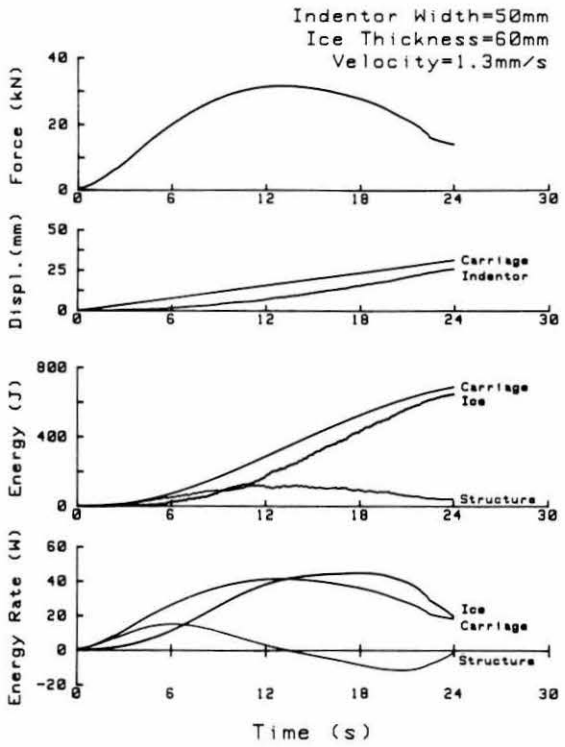

Figure A101. Test N N 49.

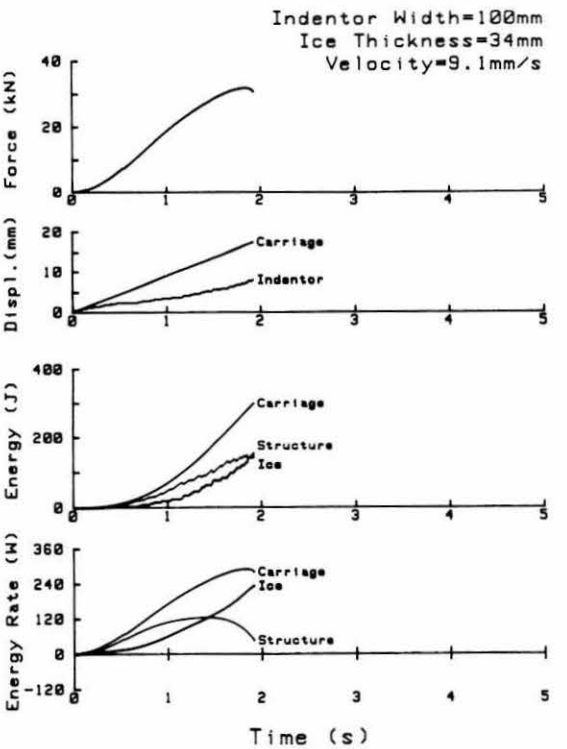

Figure A102. Test N N 51.

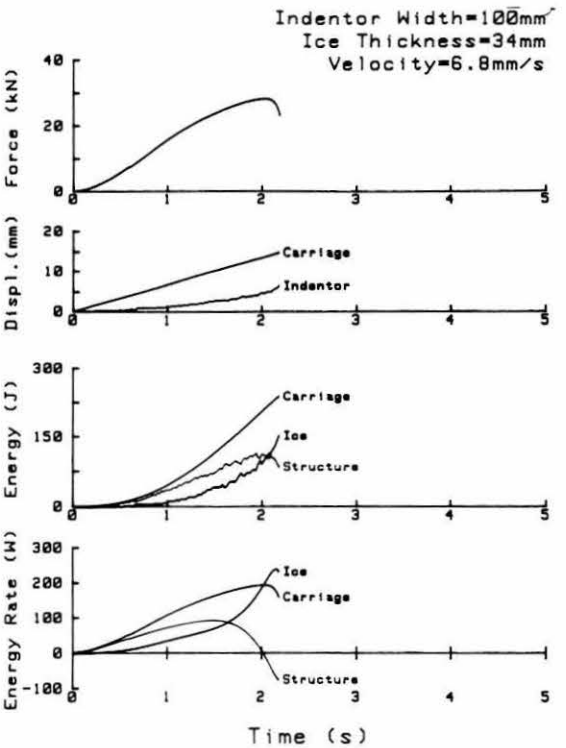

Figure A103. Test N N 52.

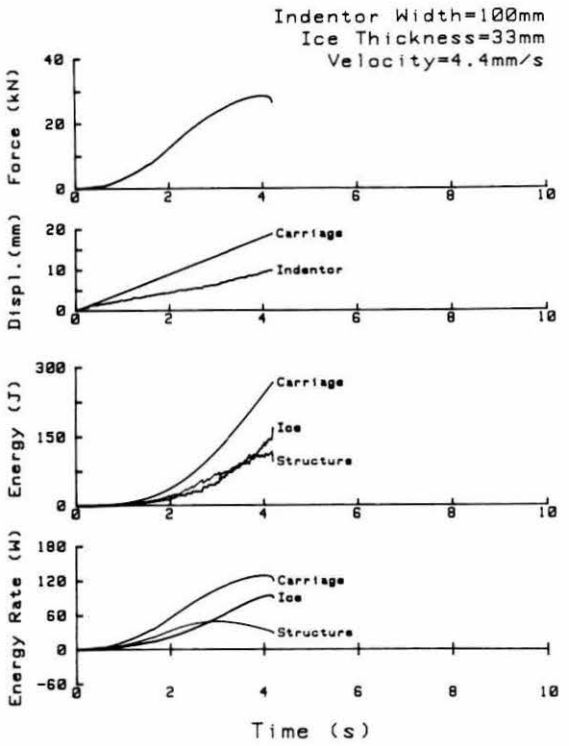

Figure A104. Test N N 55.

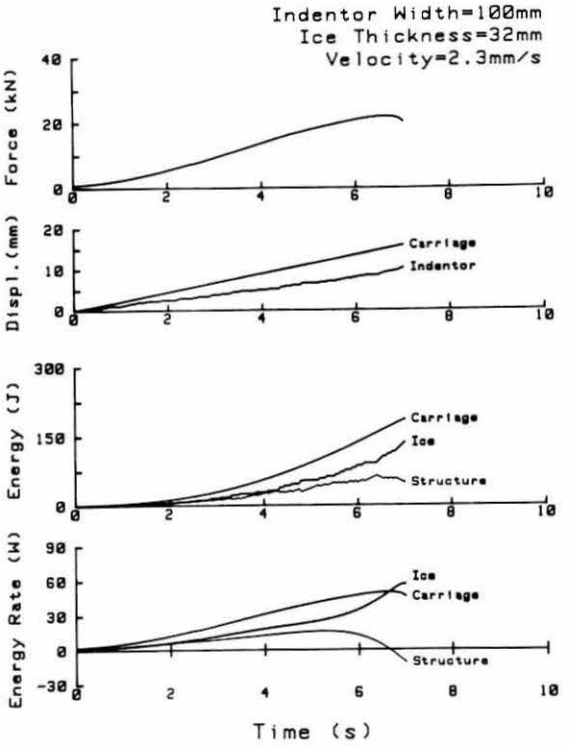

Figure A105. Test N N 57.

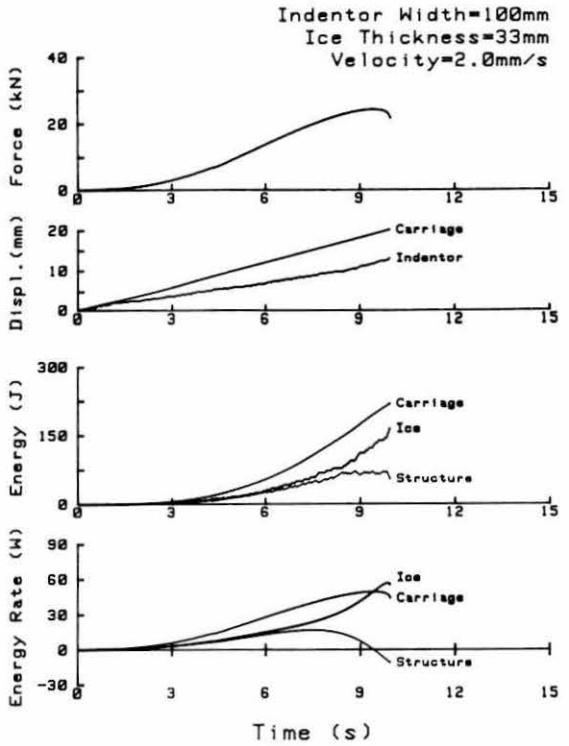

Figure A106. Test N N 59.

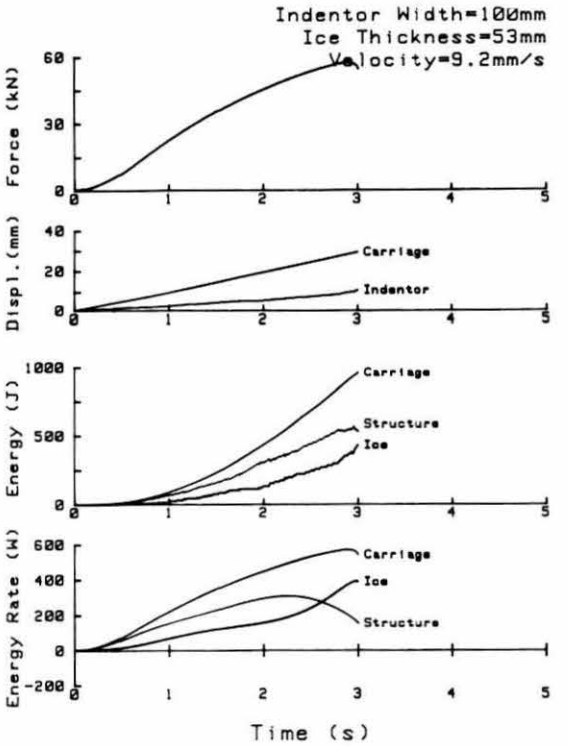

Figure A107. Test N N 61.

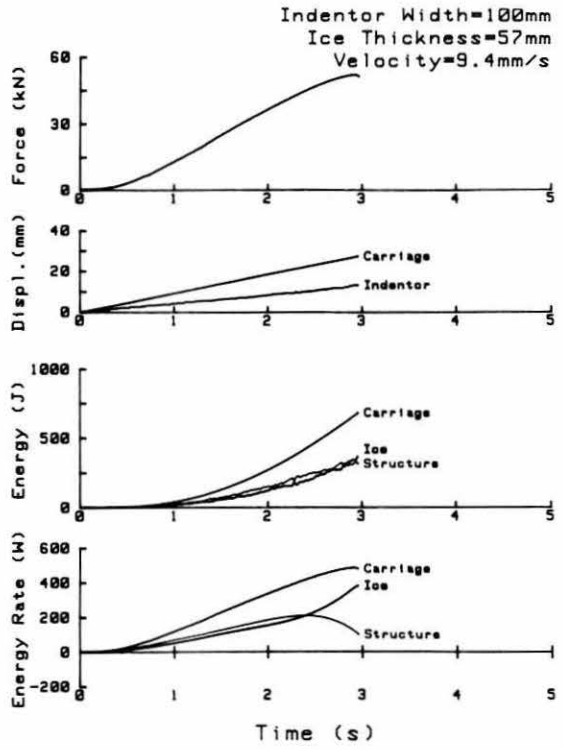

Figure A108. Test N N 701.

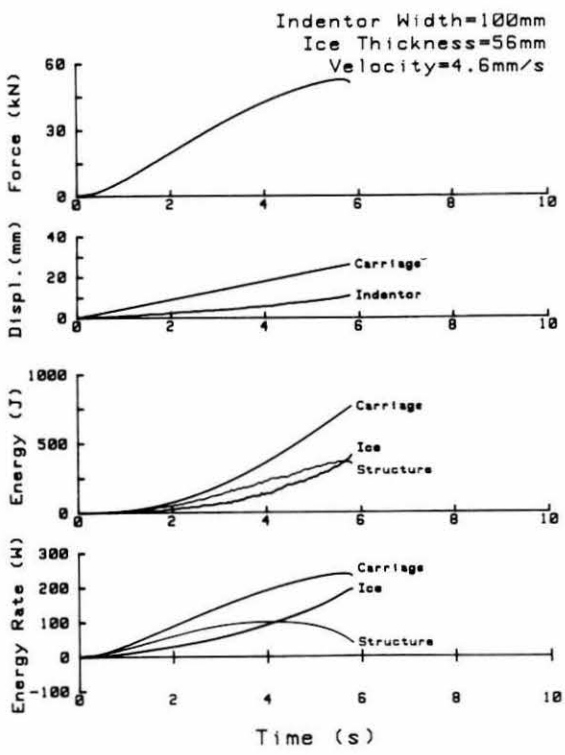

Figure A109. Test N N 65.

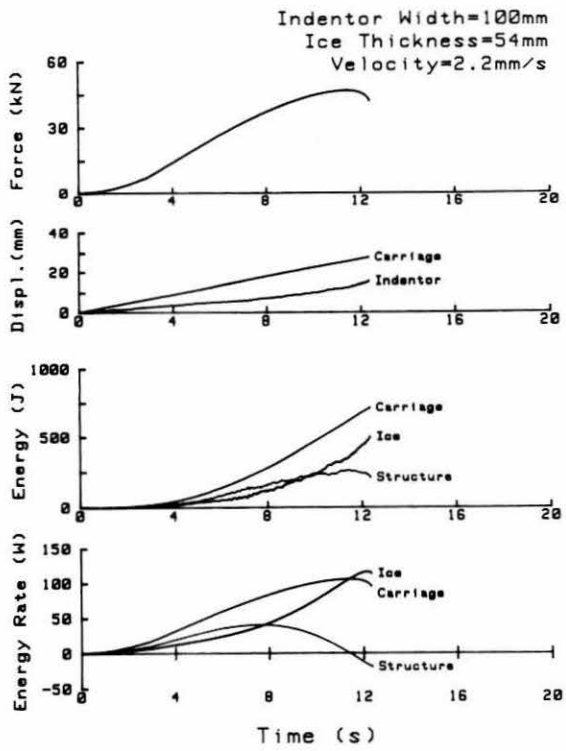

Figure A110. Test N N 67.

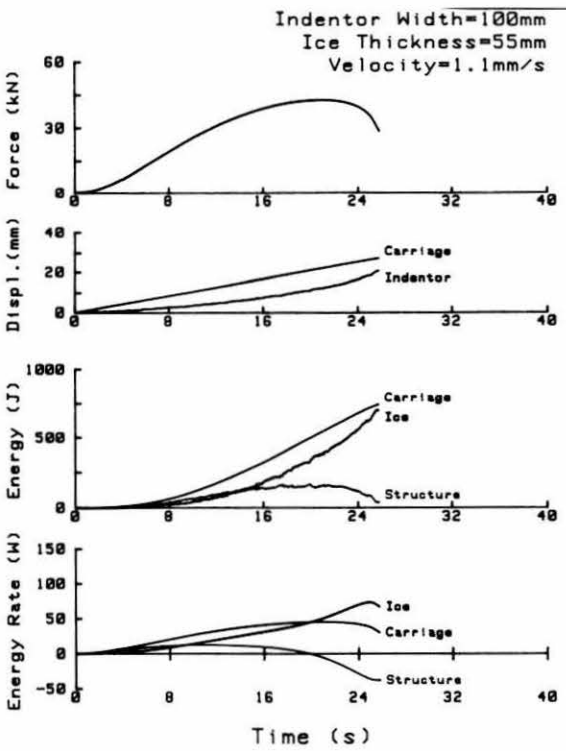

Figure A111. Test N N 69.

REPORT DOCUMENTATION PAGE

Form Approved
OMB No. 0704-0188

1. AGENCY USE ONLY (Leave blank)	2. REPORT DATE	3. REPORT TYPE AND DATES COVERED
	May, 1990	

4. TITLE AND SUBTITLE

Ice Forces on Flat, Vertical Indentors Pushed Through Floating Ice Sheets

5. FUNDING NUMBERS

CWIS 31723

6. AUTHORS

Naoki Nakazawa and Devinder S. Sodhi

7. PERFORMING ORGANIZATION NAME(S) AND ADDRESS(ES)

U.S. Army Cold Regions Research and Engineering Laboratory
72 Lyme Road
Hanover, New Hampshire 03755-1290

8. PERFORMING ORGANIZATION REPORT NUMBER

Special Report 90-14

9. SPONSORING/MONITORING AGENCY NAME(S) AND ADDRESS(ES)

Office of the Chief of Engineers
Washington, D.C. 20314

10. SPONSORING/MONITORING AGENCY REPORT NUMBER

11. SUPPLEMENTARY NOTES

12a. DISTRIBUTION/AVAILABILITY STATEMENT

Approved for public release; distribution is unlimited.

Available from NTIS, Springfield, Virginia 22161.

12b. DISTRIBUTION CODE

13. ABSTRACT (*Maximum 200 words*)

Structures placed in an ice environment should be able to withstand the ice forces that are produced by the motion of a floating ice sheet. To observe the crushing failure of ice and to characterize the magnitude and nature of ice forces, an experimental study was conducted by pushing vertical, flat indentors through floating ice sheets made up of freshwater, columnar ice. Depending on the velocity of the indentor, ductile or brittle behavior of ice was observed. Microcracks and macrocracks were observed during the tests. The energy used to produce the maximum ice force was found to be approximately the same for different indentor velocities. The positions of the resultant forces were found to be in the center of the contact area. The area of the ice damaged by the first peak loading of the identor was about the same, even when the indentor velocities were different. Acoustic emission signals were measured during indentation experiments, and these were found to correlate with the ice force that produces strain and microcracking in the ice.

14. SUBJECT TERMS

Acoustic emissions, Crushing, Effective pressure, Freshwater ice, Ice forces, Indentation, Laboratory tests, Macrocracking, Microcracking

15. NUMBER OF PAGES
70

16. PRICE CODE

17. SECURITY CLASSIFICATION OF REPORT	18. SECURITY CLASSIFICATION OF THIS PAGE	19. SECURITY CLASSIFICATION OF ABSTRACT	20. LIMITATION OF ABSTRACT
UNCLASSIFIED	UNCLASSIFIED	UNCLASSIFIED	UL

NSN 7540-01-280-5500

☆ U. S. GOVERNMENT PRINTING OFFICE: 1990--700-057--22005

Standard Form 298 (Rev. 2-89)
Prescribed by ANSI Std. Z39-18
298-102